6-2022

Methods for Focal Plane Array Resolution Estimation Using Random Laser Speckle in Non-paraxial Geometries

Phillip J. Plummer

Recommended Citation

Plummer, Phillip J., "Methods for Focal Plane Array Resolution Estimation Using Random Laser Speckle in Non-paraxial Geometries" (2022). *Theses and Dissertations*. 5484.
https://scholar.afit.edu/etd/5484

METHODS FOR FOCAL PLANE ARRAY RESOLUTION ESTIMATION USING RANDOM LASER SPECKLE IN NONPARAXIAL GEOMETRIES

DISSERTATION

Philip James Plummer, CIV, USAF

AFIT-ENP-DS-22-J-027

DEPARTMENT OF THE AIR FORCE
AIR UNIVERSITY

AIR FORCE INSTITUTE OF TECHNOLOGY

Wright-Patterson Air Force Base, Ohio

AFIT-ENP-DS-22-J-027

METHODS FOR FOCAL PLANE ARRAY RESOLUTION ESTIMATION USING RANDOM LASER SPECKLE IN NONPARAXIAL GEOMETRIES

DISSERTATION

Presented to the Faculty
Graduate School of Engineering and Management
Air Force Institute of Technology
Air University
Air Education and Training Command
in Partial Fulfillment of the Requirements for the
Degree of Doctor of Philosophy in Optical Science and Engineering

Philip James Plummer, BS, MS
CIV, USAF

May 10, 2022

DISTRIBUTION STATEMENT A
APPROVED FOR PUBLIC RELEASE; DISTRIBUTION UNLIMITED.

AFIT-ENP-DS-22-J-027

METHODS FOR FOCAL PLANE ARRAY RESOLUTION ESTIMATION USING RANDOM LASER SPECKLE IN NONPARAXIAL GEOMETRIES

DISSERTATION

Philip James Plummer, BS, MS
CIV, USAF

Committee Membership:

Michael A. Marciniak, Ph.D
Chair

Kenneth W. Burgi, PhD, Lt Col
Member

Tony Liu, PhD, Capt
Member

Michael T Eismann, PhD
Member

Kenneth J Barnard, PhD
Member

AFIT-ENP-DS-22-J-027

Abstract

The infrared (IR) imaging community has a need for direct IR focal plane array (FPA) evaluation due to the continued demand for small pixel pitch detectors, the emergence of strained-layer-superlattice devices, and the associated lateral carrier diffusion issues. Conventional laser speckle-based modulation transfer function (MTF) estimation is dependent on Fresnel propagation and a wide-sense-stationary input random process, limiting the utilization of this approach on lambda-scale IR devices.

This dissertation develops two alternative methodologies for speckle-based resolution evaluation of IR FPAs. Both techniques are formulated using Rayleigh-Sommerfield electric field propagation, making them valid in the nonparaxial geometries dictated by the resolution estimation of lambda-scale devices. The generalized FPA MTF estimation approach numerically evaluates Rayleigh-Sommerfeld speckle irradiance autocorrelation functions (ACFs) to indirectly compute the power spectral density (PSD) of a non-wide-sense-stationary (WSS) speckle irradiance random process. The experimental error incurred by making WSS assumptions regarding the associated laser speckle random process are quantified utilizing the Wigner distribution function. This method is experimentally demonstrated on a lambda-scale longwave infared FPA, showing at 27% spatial frequency range improvement over established estimation methodology. Additionally, a resolution estimation approach, which utilizes an iterative maximum likelihood estimation approach and speckle irradiance ACFs to solve for a system impulse response, is developed and demonstrated with simulated speckle imagery.

Acknowledgements

I would like to express my sincere gratitude to my advisor, Michael Marciniak, for his enduring guidance and support throughout this research effort. I would also like to thank Kenneth Barnard for the countless technical discussions and thorough reviews of my work. I would, also, like to thank my committee members Michael Eismann, Capt. Tony Liu and Lt. Col. Kenneth Burgi for their suggestions and involvement in this work. I appreciate the great deal of effort my AFRL colleagues committed to whiteboard sessions, general problem solving, FPA testing expertise and advice. My AFRL leadership is acknowledged for providing the opportunity to pursue this research. Finally, I would like to thank my wife for her constant encouragement throughout this effort.

Philip James Plummer

Table of Contents

List of Figures

List of Tables

METHODS FOR FOCAL PLANE ARRAY RESOLUTION ESTIMATION USING RANDOM LASER SPECKLE IN NONPARAXIAL GEOMETRIES

I. Introduction

1.1 Motivation for Research

Recent trends in commercial and military sensor markets include minimizing cost, size, weight and power (SWaP) of imaging systems, increasing pixel count of focal plane array (FPA) detectors, expanding fields of view and improving resolution. In an effort to meet these requirements, infrared (IR) detector pixels have been pushed to unprecedented small pixel sizes and FPAs developed at unprecedented large formats.

In an effort to address these high performance demands in a cost-effective manner, the Department of Defense (DoD) community has invested significant time, money and manpower into the development of III-V nBn strained-layer-superlattice (SLS) IR detectors. This promising technology offers many potential advantages over historic IR detector materials and designs, including higher operability, better yield, theoretically lower dark current, lower manufacturing costs and higher operating temperatures.

However, this technology remains relatively immature; its performance suffers as a result. SLS architectures have inherently lower absorption coefficients than conventional detector structures, leading to lower device quantum efficiency (QE). Dark current densities are on the order of two times higher than Tennant's "Rule 07" [2] due to material growth impurities. Increased dark current due to surface leakage prevents full reticulation of individual detector elements, increasing the potential for electrical crosstalk due to lateral carrier diffusion. The push to higher resolution images, thus smaller detector elements, further exacerbates this problem. Investigating the severity of this resolution degradation is vital to understanding the capability of this relatively new detector technology.

Modulation transfer function (MTF) is a well understood industry standard metric for analyzing and describing image system or subsystem resolution [3]. Many system modelers assume detector MTFs follow theoretical sinc functions based on wavelength and detector size parameters. This oversimplification typically leads to overestimation of a detector's actual resolution capabilities.

Many techniques have been developed to estimate detector MTF using a full imaging system for testing [3–9]. All of these methods incorporate front-end optics into the measurement, necessitating the need to divide out the optics MTF to obtain the desired result. This procedure may lead to errors and complications increasing the difficulty of getting an accurate detector MTF estimation, such as inaccurate lens characterization or the need for high quality, low F-number optics to cover the measurement's spatial frequency range.

Driven by the need to avoid this complication, a number of methods have been established [10–12] to directly estimate the MTF of FPAs using random laser speckle. These techniques are based on a linear systems approach to the problem, where a random process, laser speckle, is the input to a linear system, which includes the FPA and its associated read-out electronics. These speckle-based, direct FPA MTF techniques require wide-sense-stationary (WSS) random process inputs and Fresnel approximations for electric field propagation. To estimate the resolution of lambda-scale detectors, meaning the detector pixel pitch is approximately equal to the desired detection wavelength, nonparaxial testbed geometries must be utilized, forcing modifications to established speckle-based MTF estimation techniques.

1.2 Problem Statement

In an effort to evaluate lambda-scale state-of-the-art SLS IR detectors, this research aims to improve upon these random laser speckle MTF estimation techniques via the following avenues:

- Investigation of laser speckle second-order statistics in nonparaxial test geometries dictated by lambda-scale detectors, understanding random process characteristics and their impact on the established estimation techniques.
- Formulating numerical methods for computing laser speckle second-order statistics in nonparaxial geometeries.
- Development of valid FPA resolution techniques considering the characteristics of the laser speckle random process in proposed test geometries, producing MTF estimations at higher spatial frequencies than previously attainable via established speckle-based methodologies.
- Specific to applicable spatial-frequency-based resolution estimation techniques, optimization of the output PSD estimation process via robust investigation of relevant parameters influencing output PSD outcomes, ensuring accurate estimation given the test environment.

1.3 Organization

Chapter II introduces and elaborates on vital background information in support of this study, beginning with a brief tutorial on linear system analysis, focusing on MTF. The focus then shifts to detector MTF theory, discussing ideal detector performance and the impact of crosstalk on detector resolution. Various detector MTF estimation methods are investigated; the advantages and disadvantages of each technique are discussed. A review of speckle-based MTF estimation method variations are examined with detailed attention applied to the efforts by Barnard [11] which supplied foundational building blocks for this research. Finally, an introduction to the Wigner Distribution Function (WDF), a function critical to analyzing non-WSS random processes such as laser speckle, is presented.

A rigorous investigation of the speckle imagery output PSD estimation process is conducted in Chapter III. Parameters examined include number of independent speckle image realizations, window type, window size and aperture shape. Additionally, the PSD estimation variance versus resolution trade-off is analyzed and the impact of signal-independent noise on output PSD estimations was investigated. Finally, the analysis is extrapolated from output PSD to FPA MTF estimation accuracy.

Chapter IV develops the generalized MTF estimation technique, addressing the challenge of FPA MTF estimation in scenarios where lambda-scale detectors require nonparaxial test geometries. Speckle irradiance autocorrelation functions (ACFs) developed via Rayleigh-Sommerfeld electric field propagation are numerically evaluated on the Air Force Research Laboratory's High Performance Computing Systems, then utilized to indirectly determine the PSD of a non-WSS laser speckle random process. The error associated with making stationary assumptions and employing linear systems analysis is quantified via use of the WDF. Finally, the generalized estimation technique is applied experimentally to estimate the MTF of a lambda-scale LWIR detector.

An iterative maximum likelihood approach for FPA impulse response estimation valid beyond conventional paraxial constraints of Fresnel propagation and applicable to non-WSS random processes is introduced in Chapter V. Development of the technique theory and demonstration of capability with simulated speckle images is presented. Practical method implementation challenges, including independent speckle image realization generation and speckle image microscanning super-resolution application are explained.

Finally, Chapter VI summarizes key results, highlights major contributions and discusses future work.

II. Background and Literature Review

This chapter provides important technical and theoretical context in support of the conducted research. First, the concept of modulation transfer function (MTF) in described, focusing on ideal FPA performance and factors impacting FPA resolution, such as crosstalk. Then, various FPA MTF estimation techniques are introduced; the advantages and disadvantages of the methods are discussed. Next, the analytical development of a laser speckle electric field autocorrelation function (ACF) utilizing Rayleigh-Sommerfeld (RS) diffraction integrals is described. After that, the Wigner Distribution Function (WDF) is introduced and demonstrated in the context of stochastic processes. Finally, novel infrared (IR) FPA devices are presented, with a focus on design architecture and FPA resolution impact.

2.1 Modulation Transfer Function Theory

MTF is the industry standard metric for quantifying the resolution capability of a composite imaging system. The metric is directly applicable for resolution analysis of individual imaging system sub-components, such as focal plane arrays (FPA). Accurate estimation of this FPA resolution parameter is the primary goal of the research efforts undertaken in the subsequent chapters. MTF is based on linear systems theory; a system or phenomenon must be considered linear and spatially invariant to be described with a transfer function [13]. Utilization of this powerful tool can allow one to characterize system or sub-system components needed to evaluate design trades and improve performance.

2.1.1 Impulse Response

In linear systems terminology, an impulse response is an optical linear system's reaction to a point source input. This concept is represented mathematically as,

$$g(x, y) = f(x, y) * *h(x, y), \tag{1}$$

where ** is a 2-D convolution between the input, $f(x, y)$, and system impulse response, $h(x, y)$ where (x, y) are spatial coordinates. This operation results in a system output, $g(x, y)$.

Using linear system theory, each imaging system component's effect on a point source input can be accounted for using convolution,

$$\begin{aligned} g(x, y) = f(x, y) * *h_{turb}(x, y) * *h_{optics}(x, y) * *h_{FPA}(x, y) * * \\ h_{ele}(x, y) * *h_{drift}(x, y) * *h_{jitter}(x, y) * *h_{blur}(x, y), \end{aligned} \tag{2}$$

where h_{optics}, h_{FPA}, h_{turb}, h_{ele}, h_{drift}, h_{jitter} and h_{blur} are the impulse responses of the imaging system's optics, FPA, atmospheric turbulence experienced by the system, linear line-of-sight drift, random jitter during frame integration time and optical blur due to aberrations, respectively. These sub-component impulse responses have been combined to form an entire system impulse response, $h_{sys}(x, y)$,

$$\begin{aligned} h_{sys}(x, y) = h_{turb}(x, y) * *h_{optics}(x, y) * *h_{FPA}(x, y) * * \\ h_{ele}(x, y) * *h_{drift}(x, y) * *h_{jitter}(x, y) * *h_{blur}(x, y). \end{aligned} \tag{3}$$

The convolution of a full system impulse response with a point-source input, generating a system output, $g(x, y)$,

$$g(x, y) = f(x, y) * *h_{sys}(x, y). \tag{4}$$

2.1.2 Transfer Function

Using the convolution theorem, this analysis can be converted to the spatial frequency domain,

$$G(\xi, \eta) = F(\xi, \eta)H_{sys}(\xi, \eta), \tag{5}$$

where $G(\xi, \eta)= \mathcal{F}[g(x, y)]$, $F(\xi, \eta)=\mathcal{F}[f(x, y)]$, $H_{sys}(\xi, \eta)=\mathcal{F}[h_{sys}(x, y)]$ and $\mathcal{F}$ represents the 2D Fourier transform. Analyzing systems in the frequency domain rather than the spatial domain is preferred; multiplications are easier to perform and visualize than convolutions. The normalized version of H_{sys}, is referred to as the optical transfer function (OTF),

$$H_{sys}(\xi, \eta) = |H_{sys}(\xi, \eta)|exp[-j\Theta(\xi, \eta)], \tag{6}$$

where $\Theta(\xi, \eta)$ is the phase transfer function and $|H_{sys}(\xi, \eta)|$ is the MTF.

2.1.3 Modulation Transfer Function

The MTF is the normalized magnitude response of the optical system or component to sinusoids of different spatial frequencies. When optical systems are analyzed in the frequency domain, sine wave objects are considered rather than point sources [3]. Modulation depth is a measure of contrast,

$$M = \frac{A_{max} - A_{min}}{A_{max} + A_{min}}, \tag{7}$$

and defined as the amplitude of the irradiance variation divided by the bias level, where A_{min}, is the maximum value of the output image and A_{max}, is the minimum value of the output image. When a sinosoid is the object of interest, modulation depth can be considered the AC value of the waveform divided by the DC bias. The limited spatial resolution of the optical system results in a decreased modulation depth of the image relative to that of the object distribution. An incoherent imaging system experiences reduced modulation when observing sinusoids of increasing spatial frequency. Decreasing modulation depth is directly tied to a lower MTF over the spatial frequency range of interest, as shown in Fig. 1.

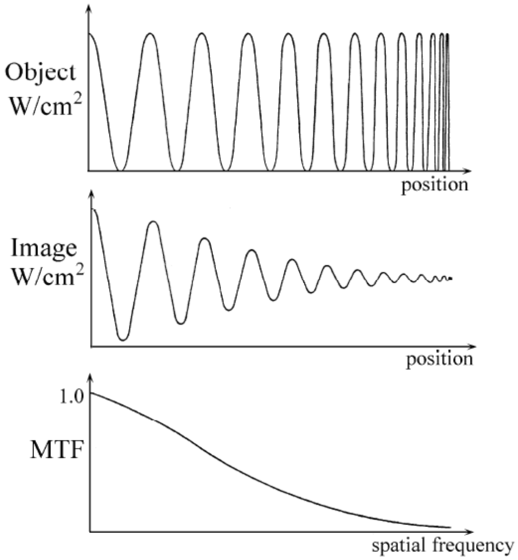

Figure 1: Visual representation of the relationships between spatial frequency, modulation depth and MTF. Image taken from source with permission [3].

The MTF is useful as a resolution specification, demonstrating system performance over a wide range of spatial frequencies. MTF units are typically in cycles/mm, but can be represented in angular space for comparison of overall system performance. The MTF allows the opportunity to aggregate independent sub-system or phenomenology via multiplication to describe a full scenario's impact on image resolution, as demonstrated in Figs. 2 and 3. Dividing out known sub-system MTFs from a composite system MTF is also a technique for isolating unknown sub-system

MTF contribution.

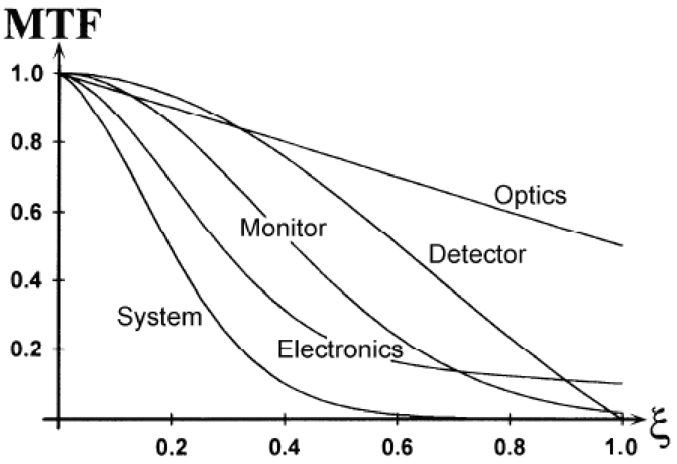

Figure 2: An example of cascading sub-system MTFs forming a full system MTF. Image taken from source with permission [3].

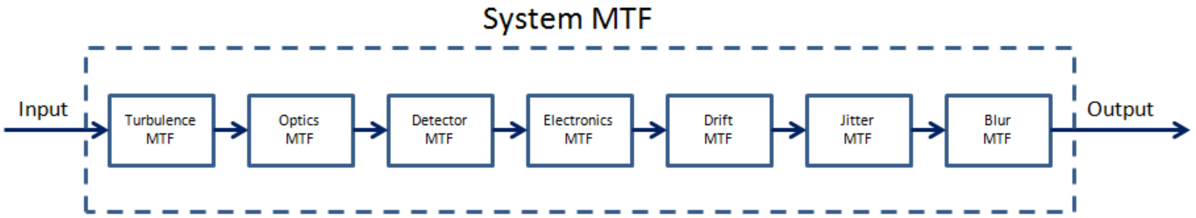

Figure 3: Block diagram of cascading sub-system MTFs to form a full system MTF.

2.1.4 Theoretical FPA MTF

A theoretical FPA MTF equation by treating the FPA as an integral sampler [14]. An integral sampler produces a sampled version of the scene input irradiance by spatially averaging the input irradiance over the FPA, then performing delta-function sampling at the center of each detector element. This integral sampling process for an FPA with square detector pixels is shown as,

$$r(x,y) = k[i(x,y) ** rect(\frac{x}{w},\frac{y}{w})] \times comb(\frac{x}{w},\frac{y}{w})) \times rect(\frac{x}{W},\frac{y}{W}), \tag{8}$$

where $rect(x, y)$ and $comb(x, y)$ are the rectangle and comb functions as defined in Ref. 15, $i(x, y)$, is input irradiance function, $r(x, y)$ is the sampled version of the scene input radiance, w is the detector element width and W is the lateral dimension of the FPA. A square FPA and 100% fill factor detector elements are assumed in this analysis. A Fourier transform of Eq. (8) provides the sampled input radiance spectrum.

$$R(\xi, \eta) = k[I(\xi, \eta)sinc(w\xi, w\eta)] * *comb(w\xi, w\eta) * *sinc(W\xi, W\eta), \tag{9}$$

where $sinc(\xi, \eta)$ is the sinc function as defined in Ref. 15 and ξ and η are spatial frequencies. Since W≫w, $sinc(W\xi, W\eta)$ can be approximated as a delta function, $\delta(\xi, \eta)$. If the input irradiance function is bandlimited and properly sampled by the FPA, meaning $\xi_s > 2\xi_i$, where ξ_i is the cutoff frequency of the input radiance spectrum and ξ_s is the sampling frequency of the FPA, no aliasing occurs and only comb's center delta function is considered. Note, if $I(\xi, \eta)$ is not properly sampled by the FPA, aliasing will occur and $I(\xi, \eta)$ cannot be accurately represented by $R(\xi, \eta)$. Aliasing is experienced in Section 5.3.3 when spatially narrow (spectrally broad) speckle ACFs are undersampled by an FPA, resulting in inaccurate ACF estimations. Making the aforementioned simplifications allows the Eq. (9) sampling input radiance spectrum to reduce to,

$$R(\xi, \eta) = kI(\xi, \eta)sinc(w\xi, w\eta), \tag{10}$$

Utilizing Eq. (5) and normalizing the ratio between the output spectrum, $R(\xi, \eta)$, and input spectrum, $I(\xi, \eta)$, results in the following FPA OTF, H_{det} and MTF, $|H_{det}|$,

$$\begin{aligned} H_{FPA}(\xi) &= sinc(w\xi, w\eta), \\ |H_{FPA}(\xi)| = |sinc(w\xi, w\eta)| &= \left| \frac{sin(\pi\xi w)}{\pi\xi w} \frac{sin(\pi\eta w)}{\pi\eta w} \right|, \end{aligned} \tag{11}$$

Note that the w term refers to the width of the detector's active area and not the FPA pixel pitch. For a square detector, fill factor refers to the percentage of light-sensitive, or active, area of a detector versus the squared pixel pitch of a device. A device with a low fill factor and a smaller active area will theoretically produce a higher MTF and thus a higher resolution image. However, a lower fill factor design will capture less overall target irradiance, lowering the device's overall signal-to-noise ratio (SNR).

Most detector elements are square in shape, therefore Eq. (11) is the standard representation of a FPA's spatial frequency response in imaging system models. If the detector elements' active areas are a different shape, the MTF is directly related that particular shape's Fourier transform. The MTF of a focal plane consisting of hexagonal detector elements was investigated by Boreman and Barnard [14]. Though simple and effective for many situations, the assumption of ideal detector element performance is not always accurate and can potentially mislead a system designer regarding the resolution performance of a particular detector array. Crosstalk issues can result in an FPA not achieving ideal resolution performance [16].

2.1.5 Crosstalk

One of the main phenomena causing deviation between theoretical and actual IR FPA resolution performance is crosstalk. Crosstalk is any situation where illumination impinging on or carriers generated in one detector element create signal in an adjacent element. Electrical crosstalk is attributed to carriers generating within one detector, diffusing and being collected by an adjacent detector element [17]. Electric crosstalk within the actual ROIC is another source of resolution degradation that may be experienced during this research effort.

Requirements for increased image resolution have continued to push IR pixels to smaller sizes, which in turn increases the potential for crosstalk between adjacent pixels [16]. Crosstalk's effect on FPA resolution has been effectively and accurately represented using a one dimensional exponential decay model [18],

$$|H_{cd}(L_{eq}, \xi)| = \frac{1}{1 + (2\pi L_{eq}\xi)^2}, \tag{12}$$

where L_{eq} is the lateral diffusion length of the carriers in the given detector material and ξ is the spatial frequency under consideration. Combining this carrier diffusion model in series with an ideal 1-D FPA MTF allows the resolution impact of reticulated, meaning the detector material is etched to physically and electrically isolate each individual pixel, and unreticulated detectors to be theoretically analyzed. Figure 4 compares the MTFs of FPAs with two theoretical InSb detectors, one with a $30\mu m$ pixel pitch and 100% fill factor ($30\mu m$ active detector length), and another with a $30\mu m$ pixel pitch, but reticulated to a 25% fill factor ($15\mu m$ active detector length). A nominal InSb diffusion length value of $7.1\mu m$ is used in this comparison. Figure 4 demonstrates the FPA with the $15\mu m$ detector having an increased MTF over FPA with the unreticulated detector. A number of factors influence the degree to which reticulation is possible or effective, such as increased dark current due to surface leakage currents and reduced fill factor leading to reduced signal levels.

Additionally, as discussed in Sec. 2.1.4, another critical factor in system performance is the FPA's ability to accurately sample the scene input irradiance. Included in Fig. 4 is the Nyquist sampling frequency of the FPAs utilized in this analysis. The FPA's Nyquist sampling frequency,

$$\xi_{Ny} = \frac{\xi_s}{2} = \frac{1}{2d_p}, \tag{13}$$

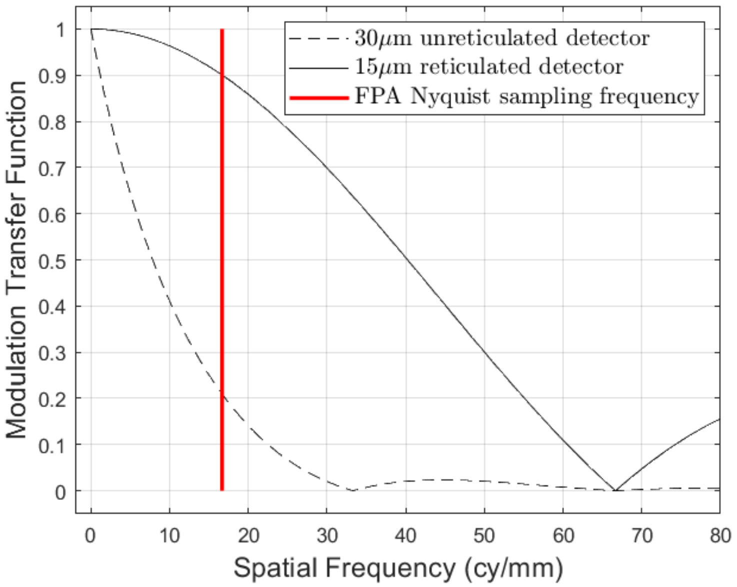

Figure 4: Comparison of theoretical MTFs of FPAs with $30\mu m$ pixel width unreticulated and $15\mu m$ pixel width reticulated InSb detectors.

where d_p is the FPA pixel pitch. If the scene spectrum input into the FPA is greater than ξ_{Ny}, higher scene spatial frequency content will alias, inducing undesirable image artifacts. Unless the imaging system's lens is designed to cut off the input spectum near ξ_{Ny} or microscanning super-resolution techniques are incorporated into the system design, significant aliasing will occur when using the FPA with the reticulated detector. Additionally, the reduced fill factor detector elements will result in a lower sensitivity device, as demonstrated in Sec. 2.2.3. When analyzing FPA performance, not only MTF, but also device sampling and sensitivity characteristics must be taken under consideration.

2.2 Modulation Transfer Function Estimation Techniques

This section serves as an overview of FPA MTF estimation techniques applied in industry and academia. Various direct and indirect estimation methods are reviewed, highlighting the advantages and disadvantages of each technique. Additionally, random laser speckle-based FPA MTF estimation techniques are introduced and discussed here; these methods are foundational to the alternative speckle-based FPA resolution methods developed in Chapters IV and V.

2.2.1 Indirect FPA MTF Estimation Techniques

Indirect FPA MTF estimation techniques refer to measurement methods where the entire imaging system, including the optics, is utilized to image a scene or target and generate a full system MTF. Estimated MTFs of subsystem components are then removed from the full system result, leaving an estimation for the FPA's MTF. This section introduces and describes a number of prominent indirect FPA MTF estimation methods.

2.2.1.1 Bar Pattern Techniques

For imaging systems, one technique for MTF estimation is viewing bar target patterns, such as the Air Force 1951 Bar Target, shown in Fig. 5, through a collimator and determining the signal amplitude reduction. The patterns follow a $2^{\frac{1}{6}}$ size increase progression and are split into sets of six vertical or horizontal bars (three white and three black). In the thermal IR, sets of eight bars are typically used. For each horizontal set of bars, there is a corresponding vertical set of bars with identical width, providing the ability to estimate both the vertical and horizontal MTF of an imaging system. Each set of bars is associated with a fundamental spatial target frequency and additional harmonics. This particular target type was historically developed for analog imaging systems, but has alternatively been utilized for digital imaging systems. Ideally, one would want to measure the modulation of a set of single frequency sinusoids in order to get estimate an optical system MTF, but since sinusoids are challenging to properly construct, bar targets are typically used as a surrogate.

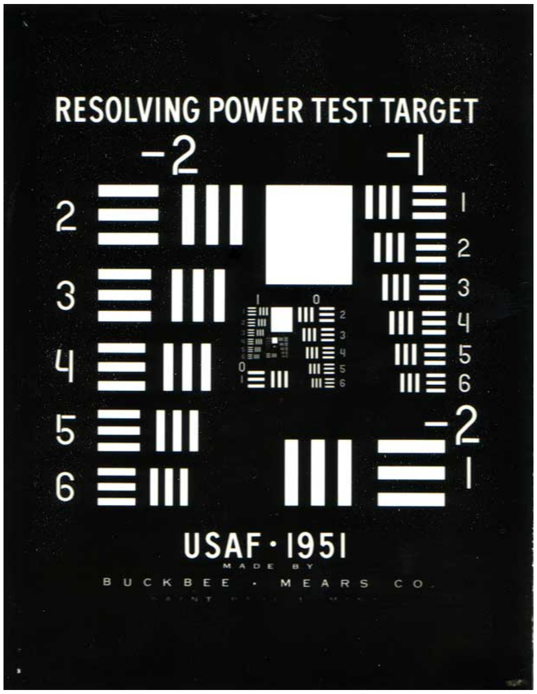

Figure 5: Image of 1951 USAF Bar Target.

Sitter [19], Boreman [3, 6] and Smith [20] all discuss methods of determining the MTF of an imaging system using bar targets. Each method essentially involves imaging a specific set of bars, recording the contrast between sets of black and white bars in the pattern, removing the harmonics associated with a specific bar pattern and recording the modulation of a fundamental spatial frequency associated with a pattern. Each bar set should eventually produce one point on an MTF plot. Considering there are infinite harmonics included in the calculation, a typical rule of thumb for determining the number of harmonics to subtract is stopping at the cut-off frequency of the system's optics. A basic representation of the bar target-based MTF estimation process is,

$$|H(\xi)| = \frac{\pi}{4}[CTF(\xi_f = \xi) + \frac{CTF(\xi_f = 3\xi)}{3} - \frac{CTF(\xi_f = 5\xi)}{5} + ...], \tag{14}$$

where ξ is the spatial frequency (cycles/mm) and contrast transfer function (CTF) is the contrast between a specific set of black and white bars. The $\pi/4$ scale factor accounts for a built-in measurement bias. CTFs are generally slightly larger than their associated MTFs.

This particular MTF estimation method is relatively inexpensive. There is a need for a high quality collimator, a set of bar targets, lens MTF data and some processing software to calculate MTF using one's images.

No matter the harmonic subtraction process, aliasing issues are absolutely included in the measurement; filtering out harmonics present in the bar targets is difficult. Super-resolution approaches, such as subpixel dithering, can reduce aliasing effects, but measurement complexity is significantly increased. Another issue with this specific measurement is that only a discrete number of points on the MTF curve can be calculated for the measurement. Therefore, interpolation must be utilized to generate a smooth, continuous MTF curve. This interpolation step introduces some error into the estimation. In addition, this technique was originally designed for the estimation of a full imaging system. If one were only interested in the FPA MTF, the MTF of the optics would have to be divided out of the composite result. Obtaining the MTF of optics may be challenging. Designers of inexpensive optics may not be able to provide measured MTF data. If measured data is received from a manufacturer, it was most likely generated via optical system modeling software and not actually measured data. This estimation may vary from the actual optical system MTF. Lens designers may also measure the optical MTF with an interferometer at one laser wavelength. The bar target measurement is a polychromatic estimation, so some error is generated with directly comparing these two results. These estimation challenges a can potentially increase the variance of a FPA MTF estimate.

2.2.1.2 Knife Edge Measurement

The current industry standard technique for imaging system resolution evaluation is the slant-edge technique. This method was developed by Kodak employees Burns [7, 8] and Williams [21] in the late 1990's/early 2000's. This basic approach is the current International Standards Organization (ISO) metric for imaging system resolution measurements [4].

The basic knife edge analysis method, shown in Fig. 6, starts with capturing an edge image. This is considered an edge response function (ERF). A derivative is taken of this image, resulting in a line spread function (LSF). A discrete Fourier transform (DFT) is taken of the LSF, producing a spectral response function (SFR). Finally, the entire SFR is normalized so that the MTF(0)=1. The official ISO standard is more detailed, including radiometrically correcting input data and over-sampling to reduce aliasing effects, but the general process shown in the diagram remains the same. When working with a high quality edge, SFR and MTF can be considered equivalent.

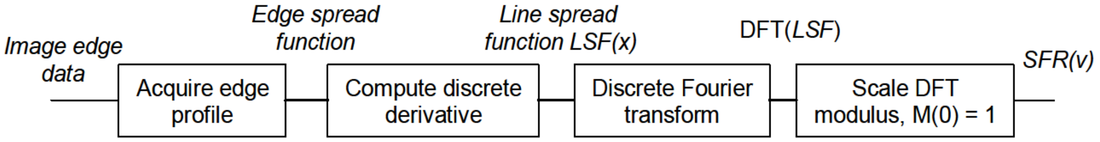

Figure 6: Block diagram outlining basic process for slant edge MTF calculation technique. Image taken from source with permission [21].

Considering this technique only requires a single image, it is a relatively simple resolution estimation method. Roland [22] investigated the stability of this technique, determining target contrast has very little impact on the resulting SFR estimation, but the degree of edge slant can seriously impact the consistency of results. The current ISO standard for the edge slant is 5 degrees [4].

Any pre-processing on images involving quantization or clipping can detrimentally effect the resulting SFR [7]. Also, this technique is a full imaging system MTF estimation method; any indirect estimation of FPA resolution performance will suffer from the same error sources described in the bar target technique.

Others have also experimented with various minor modulations on this particular method, including Chen [23], Kim [24] and Lu [25].

2.2.1.3 Other Indirect FPA MTF Measurement Techniques

Boreman and Ducharme [26] offer a methodology for full imaging system MTF testing using random transparency targets. This utilizes the same linear systems and random processes theory explained in the random laser speckle techniques, Sec. 2.2.2.1. Transition of this technique to IR wavelengths may be challenging considering the difficulty in controlling both the transmission and emission of transparencies.

2.2.2 Direct FPA MTF Estimation Techniques

Direct FPA estimation techniques are methods involving strictly the FPA in the estimation process. No intervening optics are included in the measurement. Intervening optics can add variance to an FPA MTF estimate. These techniques potentially offer more accurate solutions for FPA-only MTF estimation.

2.2.2.1 Random Laser Speckle MTF Estimation

Utilizing laser speckle as a random input process to estimate the MTF of an FPA was first introduced by Glenn Boreman [10, 27, 28]. In his experiments, the FPA and its electronics are treated as a linear, time-invariant and shift-invariant system [29] during the particular measurement. The system input is the power spectral density (PSD) of the laser speckle random process. The linear systems approach utilized in these laser speckle-based estimation techniques is,

$$G_{out}(\xi, \eta) = G_{in}(\xi, \eta)|H(\xi, \eta)|^2, \tag{15}$$

where $G_{in}(\xi, \eta)$ is the input PSD of the laser speckle into the sensor and $G_{out}(\xi, \eta)$ is the estimated PSD from the speckle imagery captured by the sensor under test. Note this process linear systems relationship is only valid when the input random process is wide-sense-stationary (WSS).

Laser speckle, seen in Fig. 7, is an interference phenomena that occurs when coherent light is scattered by an optically rough surface [10]. Optically rough refers to the surface being coarse on the order of the wavelength being analyzed. Laser speckle, historically considered a nuisance to imaging applications, has been thoroughly analyzed by Dainty [30, 31] and Goodman [32], who demonstrate that it has very useful properties. One of laser speckle's most important features is, given the shape and size of the aperture speckle passes through and the distance speckle travels, its PSD is known. Assuming a uniform speckle field and Fresnel approximations are valid for the scenario geometry [32], this PSD can be described by the normalized autocorrelation of the aperture through which the speckle field passes. Taking advantage of this property, one can control the input PSD on the FPA under test. An important characteristic of a laser speckle PSD is its spatial frequency cutoff [32],

$$\xi_{cutoff} = \frac{L}{z\lambda}, \tag{16}$$

where L is the widest extent of the aperture, λ is the laser wavelength and z is propagation distance between the aperture and observation plane. Utilization of this equation allows one to strategically match laser speckle and FPA sampling capabilities when making MTF estimations.

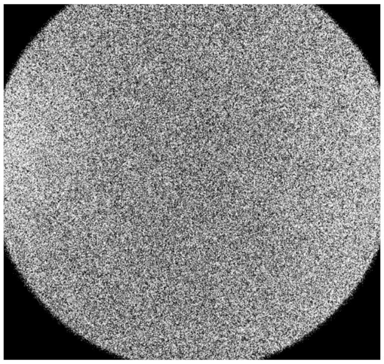

Figure 7: Image of laser speckle.

Initial Laser Speckle MTF Testbed Boreman's original laser speckle MTF testbed, shown schematically in Fig. 8, consists of a $3.39\mu m$ HeNe laser with refractive optics to expand the beam. The laser beam interacted with a fused silica diffuser, generating a uniform speckle field. The field then passes through a square aperture, diffracting the speckle field in a controlled manner, providing a known input PSD into the FPA and ROIC. Originally, Boreman utilized a square aperture, the autocorrelation of which is a triangle, which can be seen in Fig. 9. Note, $\langle I \rangle$ is the expected value of the speckle intensity determined from the first-order speckle statistics.

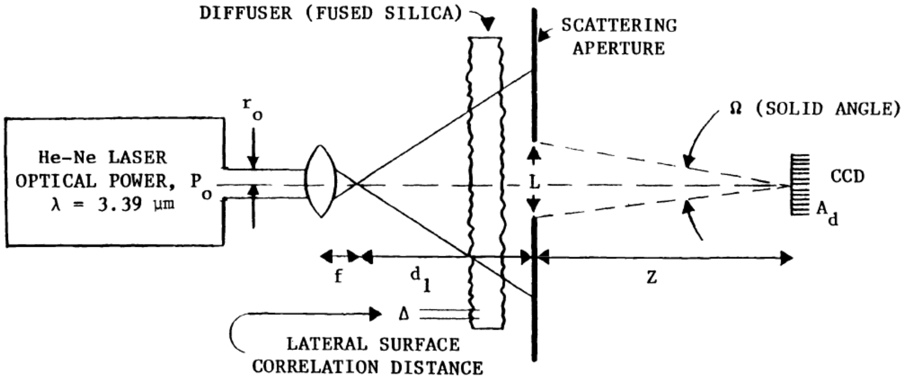

Figure 8: Boreman's original laser speckle testbed. Image taken from source with permission [27].

The output PSD was estimated via a periodogram averaging technique, where

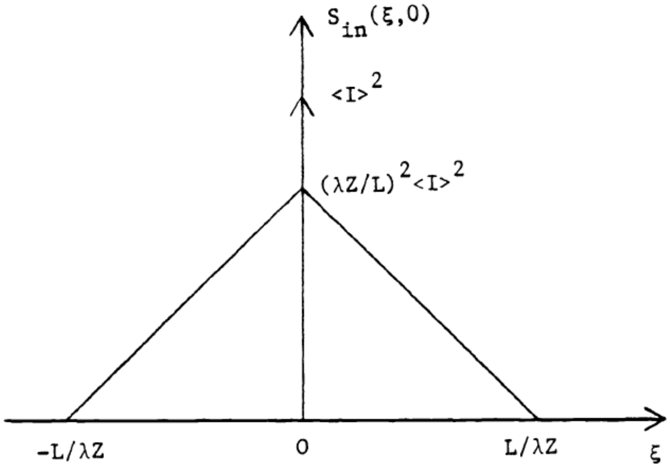

Figure 9: Input PSD of Square Aperture. Image taken from source with permission [27].

a fast-Fourier transform (FFT) was taken of each row or column of a frame, then individually normalized. Each row or column periodogram was averaged with the others in the image, resulting in one ensemble periodogram per frame. The frame periodograms were then averaged together, resulting in a final estimation of the output PSD.

With an input and output PSD determined, Eq. (15) was then applied on a per spatial frequency basis, producing the MTF data points in Fig. (10). The dots and triangles are actual data points resulting from the calculation; lines are curves fitted to the data.

Potential pitfalls with the original testbed include too few periodograms to develop an accurate spectral estimation of the output PSD. Simple uncontrolled movement of the diffuser could potentially result in highly correlated frame realizations which are ineffective at reducing estimation variance.

Addition of Integrating Sphere and Polarizer Attempting to improve FPA testing capability at IR wavelengths, Boreman investigated utilizing an integrat-

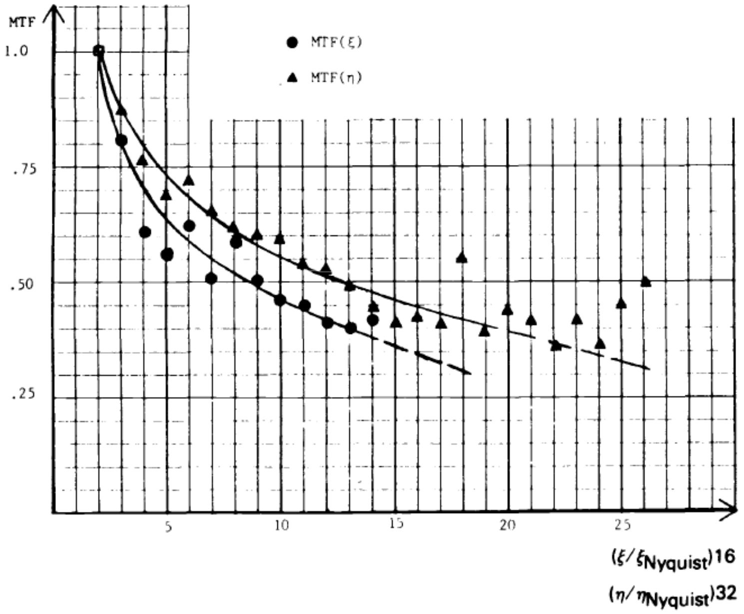

Figure 10: MTF results from Boreman's original testbed. Image taken from source with permission [27].

ing sphere to generate a uniform speckle field [33]. Boreman discovered the use of transmissive diffusers produced anomalies in the input PSD of the laser speckle due to their crystalline nature. In Ref. [32], Goodman's speckle theory analysis proves infinite reflections off a diffuse surface have the same statistical characteristics as a single reflection off a diffuse surface. As a result, integrating spheres are viable options for laser speckle generation. The integrating sphere testbed, shown in Fig. 11, was developed in the visible wavelength using a 632.8nm Helium Neon laser, but was designed with application to IR wavelengths in mind. Most subsequent researchers would adopt the use of an integrating sphere in their own testbed designs.

In addition, a polarizer was added to the integrating sphere output, allowing the analysis to be completed with ideal polarized laser speckle. Although this reduces the overall speckle intensity, it significantly improves the speckle image contrast.

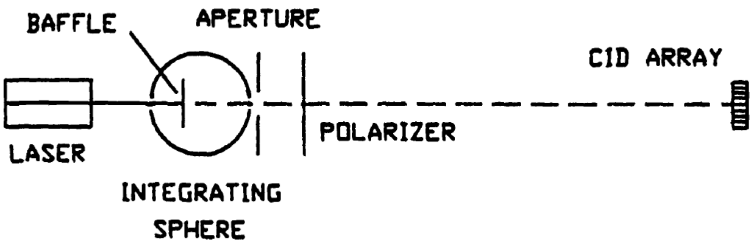

Figure 11: Boreman's integrating sphere testbed. Image taken from source with permission [33].

Measuring Past Nyquist Spatial Frequency Sensiper [34] expanded upon Boreman's testbed efforts, with a primary goal of pushing FPA MTF estimates past the Nyquist spatial frequency limit, meaning the maximum spatial frequency that can be resolved by a focal plane array without the introduction of aliasing. All work published was completed in the visible spectrum, although it is theoretically applicable to IR wavelengths. A new aperture and its corresponding PSD, shown in Figs. 12(a) and 12(b), were introduced to the testbed.

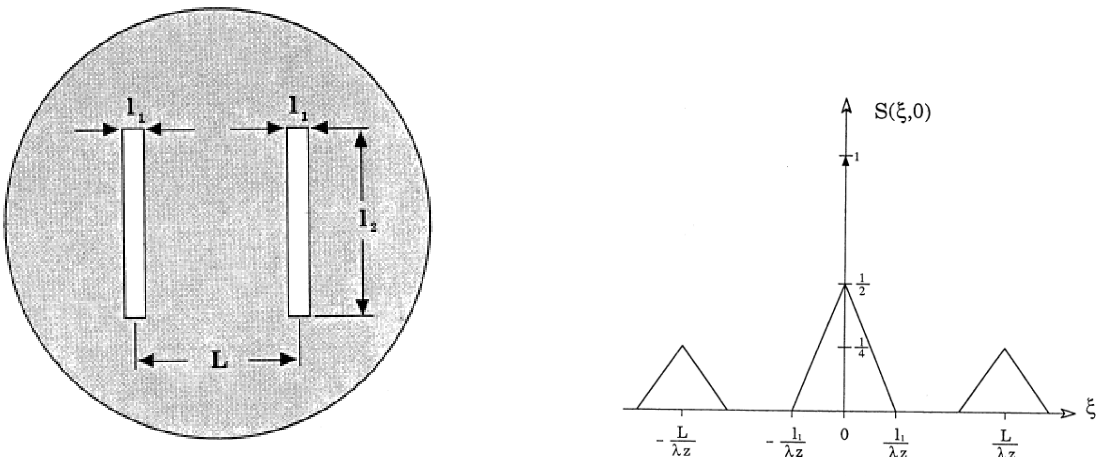

(a) (b)

Figure 12: (a) Sensiper's Two Slit Aperture, (b) PSD of Sensiper's Aperture. Images taken from source with permission [34].

In this estimation process, one MTF data point is recorded per measurement; the spatial frequency, ξ, of the measurement is set to the small triangle peak location, $\xi = L/z\lambda$. In this equation, L is the center-to-center spacing between slits, z is the distance between the aperture plane and focal plane, and λ is the laser wavelength. At aperture-to-FPA distances in which the sideband triangles are above the Nyquist frequency, the triangles are aliased symmetrically about Nyquist into lower frequencies. Since the input PSD to the FPA is bandlimited, aliased frequencies can be unfolded and spatial frequency data from zero to twice the Nyquist limit can be plotted, as shown in Fig. 13.

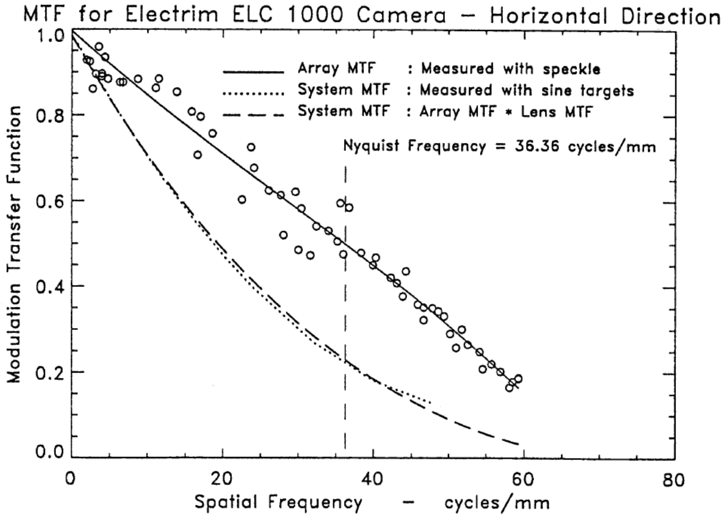

Figure 13: MTF plots from Sensiper's test. Image taken from source with permission [34].

The data collected, represented by circles in Fig. 13, had an extremely high variance. One cause of error could be misalignment between the FPA and aperture. This technique required 91 measurements to produce an MTF curve; it is a very time consuming measurement leaving many opportunities for mistakes. Oversimplification of the MTF calculation process could also lead to error; contribution of spatial frequency content from outside of the peak sideband triangle is ignored. In addition, the use of slits as apertures limits the laser speckle irradiance at the FPA, restricting the overall SNR during measurements; low power lasers and noisy FPAs may be difficult to utilize in this testbed. Pozo [35] attempted measurements with a very similar double slit aperture, producing similar results.

Ducharme [12, 36] introduced a new cross aperture design, which can be seen in Fig. 14(a). This aperture provides a constant input PSD magnitude across spatial frequencies from near DC to the FPA's Nyquist limit, as shown in Fig. 14(b). This design allows for MTF estimation from 0 to twice Nyquist spatial frequency of the FPA with only two measurements via use of a novel frequency unfolding technique.

The method requires data to be collected at two different propagation distances. The data collected at the first position is called the Nyquist set, where the flat input PSD cuts off at Nyquist. The data collected at the second position is referred to as the twice Nyquist set, where the flat input PSD cuts off at twice Nyquist. Each set is processed using a 2D FFT algorithm, producing an output PSD estimate. The Nyquist set produces the output PSD from spatial frequencies at 0 to the Nyquist limit of the FPA, $G_{0-Ny}(\xi)$. The twice Nyquist set contains the same data as the Nyquist set, plus the aliased PSD data from spatial frequencies out to twice the Nyquist folding frequency. This aliased data needs to be extracted. The extraction process is,

$$G_{2Ny-Ny}(\xi) = G_{2Ny,out}(\xi) - G_{0-Ny}(\xi), \tag{17}$$

where the twice Nyquist output PSD, $G_{2Ny,out}(\xi)$, is subtracted from the Nyquist output PSD, $G_{0-Ny}(\xi)$. Once the data past the Nyquist limit is extracted, it then needs to be properly unfolded,

$$\begin{aligned} G_{Ny-2Ny}(\xi) =& G_{2Ny-Ny}(2\xi_{Ny} - \xi), \\ & \text{for } \xi_{Ny} < \xi < 2\xi_{Ny}. \end{aligned} \tag{18}$$

The resulting output PSDs are combined,

$$G_{out,final} = \begin{cases} G_{0-Ny}(\xi) & 0 < \xi < \xi_{Ny} \\ G_{Ny-2Ny}(\xi) & \xi_{Ny} < \xi < 2\xi_{Ny}, \\ \end{cases} \tag{19}$$

resulting in a full output PSD over spatial frequencies of 0 to twice the Nyquist limit of the FPA. This technique, however, does not provide an accurate estimate for zero spatial frequency; therefore, it is difficult to properly normalize the rest of the MTF data. Also, the thin slits limit speckle signal through to the FPA, creating potential SNR issues.

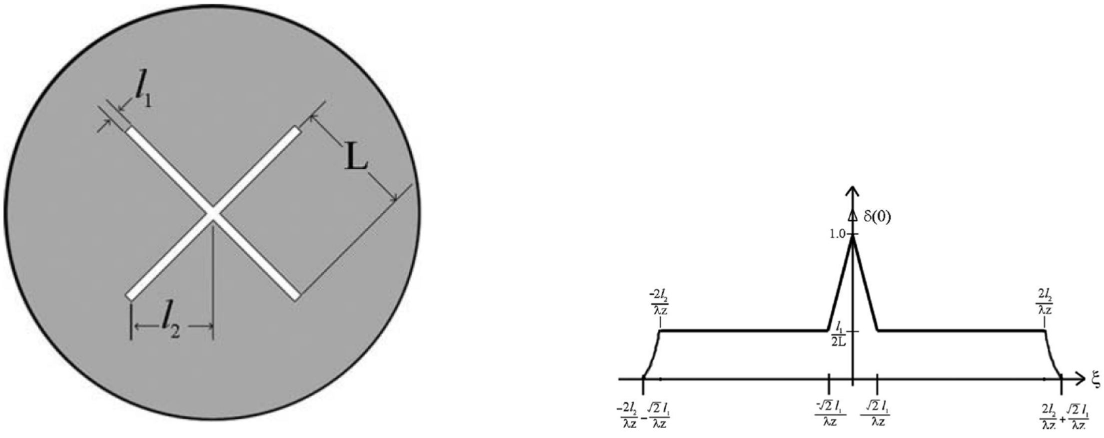

(a) (b)

Figure 14: (a) Ducharme's Cross Aperture, (b) PSD of Ducharme's Aperture. Images taken from source with permission [12].

Chen [37] experimented with extending Boreman's original measurement [10] out to twice Nyquist spatial frequency of the FPA by measuring the amplitude of the electric field just past the diffuser, then using the RS propagation integral to propagate the field,

$$E_o(x,y,z) = \frac{iz}{\lambda}\int_{-\infty}^{\infty}\int_{-\infty}^{\infty} dx_a dy_a E_a(x_a,y_a,0)\frac{exp\Bigg[-i\frac{2\pi}{\lambda}\sqrt{z^2+(x-x_a)^2+(y-y_a)^2}\Bigg]}{z^2+(x-x_a)^2+(y-y_a)^2}, \tag{20}$$

where E_a is the electric field at the aperture plane, E_o is the electric field at the observation plane, z is the propagation distance and λ is the laser wavelength. This allowed the author to generate a mathematical description of the input PSD despite violating paraxial approximations with the testbed geometry. Accurate estimation of the electric field amplitude seems challenging and the use of a transmissive diffuser may alter the laser speckle statistics. Also, the super-resolution microscan dithering technique utilized when estimating the output PSD may be challenging with large IR dewar assemblies without the introduction of additional optics or mirrors.

Other Laser Speckle-based MTF Estimation Technique Modifications Barnard [11] applied the foundations of Boreman's speckle research to state-of-the-art mid-wave infrared (MWIR) sensors by utilizing quantum cascade lasers (QCL), not previously available. Barnard utilized Welch's procedure to estimate the output PSD from the laser speckle images. Welch's procedure involves generating multiple periodograms from each speckle image by performing two dimensional FFTs on overlapped, windowed segments of each image. This methodology efficiently increased the number of periodograms available for averaging, decreasing the overall variance in the spectrum estimation process. In addition, all input and output PSD estimation calculations were performed in two dimensions, producing a unique full two dimensional estimation of the FPA MTF as shown in Fig. 15.

Astar [38] theorized an alternative aperture design to increase optical throughput of Boreman's integrating sphere testbed. This design has yet to be fabricated. The

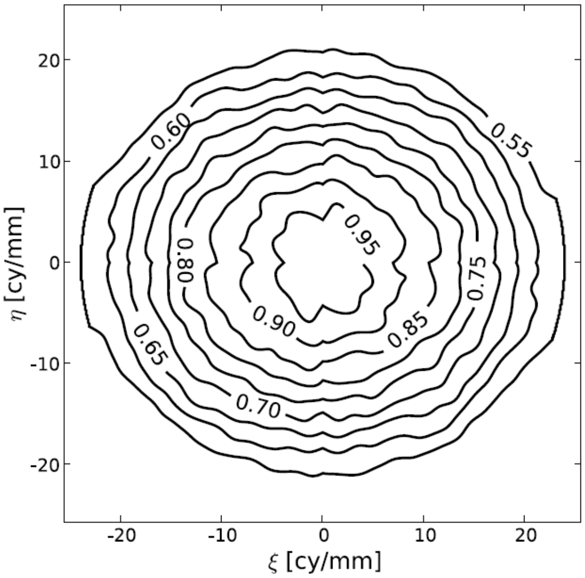

Figure 15: Image of two dimensional MTF estimation. Image taken from source with permission [11].

chemical vapor deposition process required to produce it would involve a substrate of some kind, adding an extra window to the optical chain. This could lead to transmission issues for certain IR bands and anomalies being produced in the input PSD, similar to Ref. [27].

Ducharme [39] demonstrated the viability of utilizing holographic elements in place of an integrating sphere generating the random laser speckle input necessary for focal plane MTF estimation. Generation of holograms is a time consuming process and expansion to IR wavelengths is not straightforward.

Ducharme [40] investigated a microlens array as an efficient alternative to an integrating sphere for laser speckle generation. Validated measurement results with a 632.8nm laser out to the FPA Nyquist limit were provided. Microlens arrays, as shown in Fig. 16, allow for significantly more laser throughput through a system for multiple reasons. First, transmissivity of a lens is much higher than the optical throughput of an integrating sphere. Also, microlenses preserve the laser polarization, therefore there is no need for placing a polarizer as the output of the diffraction aperture, which reduces the transmission by 50%. Disadvantages to this technique include the need for broad bandpass lenses or multiple sets of lenses for different wavelengths. Additionally, since lenses are refractive elements, they may introduce unwanted anomalies in the laser speckle.

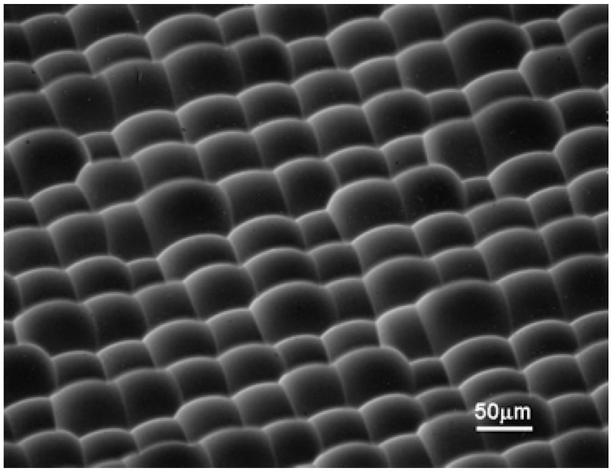

Figure 16: Magnified image of microlens array. Reprinted with permission from [40] © The Optical Society.

2.2.2.2 Other Direct FPA MTF Estimation Methods

Ying [41] introduced a novel method for direct FPA MTF estimation using scanning knife edges to generate edge spread functions over FPA elements. This is an extension of the slant edge technique described in Sec. 2.2.1.2, but generated without intervening optics. This technique allows direct measurements of FPAs past twice Nyquist. Its drawbacks include the need for precision alignment, high quality reflective optics and only being capable of polychromatic MTF estimations.

Estribeau [42] fabricated a unique complementary metal-oxide-semiconductor (CMOS) sensor with a built-in knife edge directly on the focal plane. Use of a monochromator allowed the capture of MTF measurements at different wavelengths. Using this technique in the IR requires access to fabrication facilities and could lead to calibration challenges for pixels on the knife edge. Ultimately, a destructive method is too costly for consideration.

Barnard [43,44] estimated an FPA's MTF by projecting Young's fringes of varying spatial frequencies onto the device under test. Lack of signal through pinholes and the windowing effect of the pinholes on sinusoidal fringes made this a challenging measurement. Song [45] and Greivenkamp [46] experimented with collimators, mirrors and beam splitters to project fringe patterns of varying spatial frequencies onto focal planes. Zhao [47] and Marchywka [48] created similar test beds using two different mirrors. This particular setup is only capable of measurements at a single wavelength without the purchase of a reflective collimator and a broadband beam splitter.

Scanning spot size techniques, such as Takacs [49], have also been implemented to directly estimate the resolution performance of infrared FPAs. In such techniques, a diffraction-limited laser spot is scanned across an FPA at sub-pixel resolution to generate impulse response estimations. Drawbacks to such methods include challenging measurement alignment requirements and issues generating small enough laser spot sizes, especially in the LWIR, to make accurate FPA resolution estimations.

2.2.3 FPA Performance Comparison: MTF versus Sensitivity Dilemma

Examining the ideal FPA MTF model in Eq. (11) leads one to believe that reducing the size of detector pixels leads to better system performance. Extrapolation of Eq. (11) to different pixel active area widths is shown in Fig. 17, where the FPA pixel pitch is held constant at 30μm. As the detector active area decreases, the FPA MTF increases. The FPA Nyquist frequency is also plotted in Figure 17; the same aliasing concerns and challenges apply for the demonstrated FPA MTFs with longer spatial frequency cutoffs as discussed in Sec. 2.1.5.

Additionally, a system designer has to also consider the detector element's active

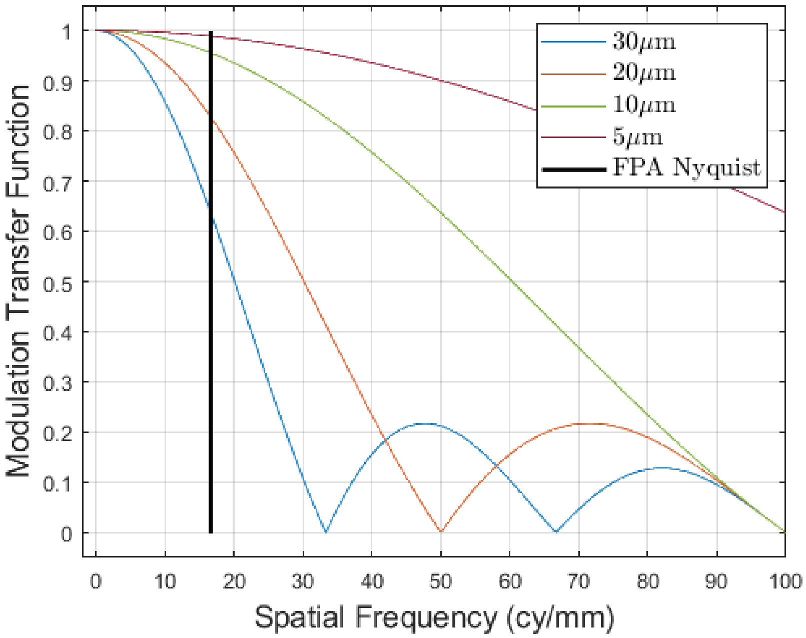

Figure 17: Graphical representation of the change in FPA MTF as a function of change in detector element active area width.

area and it's effect on the sensitivity of an imaging system. Optical system design trades were not investigated in the following comparison. Holst [50], Boreman [3] and Eismann [51] develop mathematical models of imaging system sensitivity, ultimately describing systems using "noise equivalent" metrics, such as noise equivalent irradiance (NEI). NEI is defined as the difference between incident signal and background irradiance needed to produce a SNR of one for a given system. Utilizing the system development from Ref. [51] for this discussion, a metric for aggregate FPA noise in terms of root mean squared (RMS) electrons is introduced,

$$\sigma_n = \sqrt{\sigma^2_{n,shot} + \sigma^2_{n,dark} + \sigma^2_{n,johnson}}, \tag{21}$$

where $\sigma_{n,shot}$ is the RMS electrons generated from shot noise, $\sigma_{n,dark}$ is the dark current electrons and $\sigma_{n,johnson}$ is the Johnson noise electrons. These noise terms are shown as,

$$\sigma_{n,shot} = \sqrt{N}, \tag{22}$$

$$\sigma_{n,dark} = \sqrt{\frac{J_d A_d t_d}{e}}, \tag{23}$$

$$\sigma_{n,johnson} = \sqrt{\frac{2kT_d t_d}{e^2 R_{eff}}}, \tag{24}$$

where N is the mean number of photoelectrons collected by the system. The number of photoelectrons can be estimated by $N = (A_d t_d / hc) \int \eta(\lambda) E_d(\lambda) \lambda d\lambda$, where A_d is the active area of the detector elements, t_d is the FPA integration time, h is Planck's constant, c is the speed of light, η is the detector QE, λ is the wavelength of interest and E_d is the irradiance on the FPA. From the dark current and Johnson noise calculations, J_d is the dark current density, e is the electron charge, T_d is the FPA temperature and R_{eff} is the effective detector material resistance. Shot noise and dark current noise are functions of detector active area. Note that there many more sources of noise in need of consideration ($1/f$, kTC, generation-recombination...) when analyzing an actual IR system, but these three fundamental noise sources are sufficient for the purpose of this discussion. The system SNR ratio can then be expressed in terms of photoelectron level,

$$SNR = \frac{N}{\sigma_n}. \tag{25}$$

Setting SNR equal to one and solving for irradiance, a telling relationship between NEI and detector active area is shown,

$$\begin{aligned} NEI &= \frac{hc}{\lambda} \frac{\sigma_n}{A_d t_d \eta}, && (26) \\ &= \frac{hc}{\lambda} \frac{1}{A_d t_d \eta} \sqrt{\frac{\lambda}{hc} A_d t_d \eta E_d + \frac{J_d A_d t_d}{e} + \frac{2kT_d t_d}{e^2 R_{eff}}}, && (27) \end{aligned}$$

where E_d is the mean irradiance at the FPA. No matter the dominant noise, it is apparent that detector active area and sensitivity are inversely related. Fig. 18 shows NEI curves for a nominal imaging system operating in a background-limited performance (BLIP), meaning the shot noise term, the term dependent on signal irradiance incident on the FPA, is the dominating noise component.

Although a smaller detector theoretically leads to a higher resolution, it also leads to a less sensitive overall imaging system. When evaluating potential detector element sizes, it is vital to consider system resolution, sampling and sensitivity in the decision process.

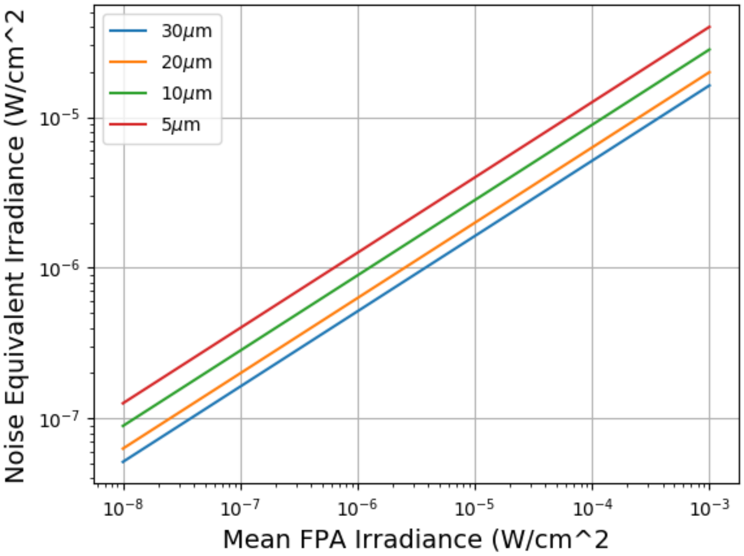

Figure 18: Graphical representation of the change in NEI as a function of change in detector active area width.

2.3 Analytical Laser Speckle Field ACF Development

This section reviews the development of a laser speckle field ACF using RS electric field propagation, rather than the Fresnel propagation [11] utilized in conventional speckle-based FPA MTF estimation efforts. This derivation is foundational to both the generalized FPA MTF estimation method developed in Chapter IV and the iterative maximum likelihood-based impulse estimation approach introduced in Chapter V, due to the validity of this ACF approach in nonparaxial test geometries.

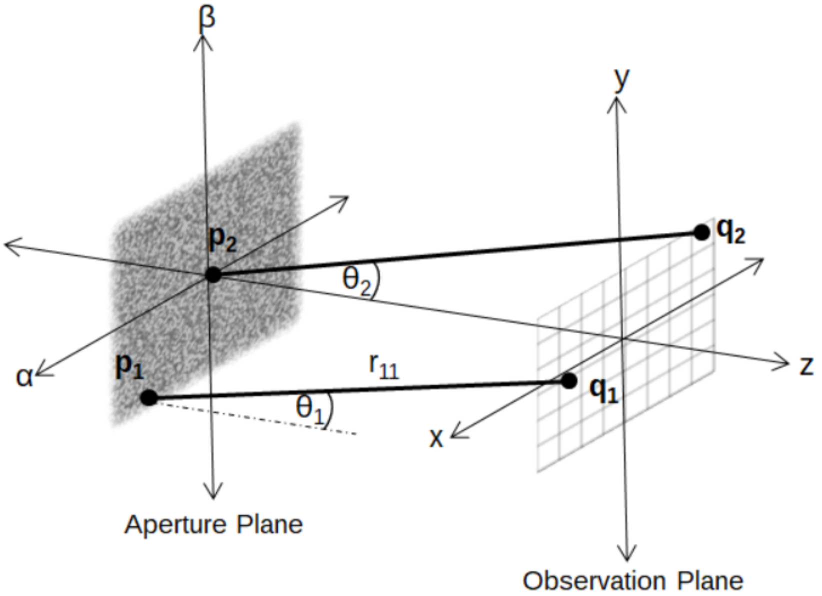

Figure 19: Free space propagation geometry for observation plane speckle irradiance autocorrelation function computation.

Development of an analytical observation plane speckle field function begins with utilizing the RS diffraction formula to propagate the speckle field at $\mathbf{p_1}$ and $\mathbf{p_2}$ in the aperture plane to $\mathbf{q_1}$ and $\mathbf{q_2}$ in the observation plane,

$$\begin{aligned} A(\mathbf{q}_1) &= \frac{1}{j\lambda}\int\int_{-\infty}^{\infty}\frac{a(\mathbf{p}_1)exp[jkr_{11}]}{r_{11}}cos(\theta_1)d\alpha_1 d\beta_1, \\ A(\mathbf{q}_2) &= \frac{1}{j\lambda}\int\int_{-\infty}^{\infty}\frac{a(\mathbf{p}_2)exp[jkr_{22}]}{r_{22}}cos(\theta_2)d\alpha_2 d\beta_2, \end{aligned} \tag{28}$$

where $a(\mathbf{p_1})$ is the complex amplitude of the speckle field at (α_1, β_1), $A(\mathbf{q_1})$ is the complex amplitude of the propagated speckle field at (x_1, y_1), r_{11} is the distance from $\mathbf{q_1}$ to $\mathbf{p_1}$ and θ_1 is the angle between r_{11} and the scattering plane's normal vector. The RS propagator is valid so long as $r_{11} \gg \lambda$.

Following the development detailed in Ref. [11], the ACF of the observation plane electric field, $\Gamma_A(\mathbf{q_1},\mathbf{q_2})$, is computed via the expected value of the product of the field amplitude at point $\mathbf{q_1}$ and the complex conjugate of the amplitude at point $\mathbf{q_2}$

$$\Gamma_A(\mathbf{q_1},\mathbf{q_2}) = \overline{A(\mathbf{q_1})A^*(\mathbf{q_2})}. \tag{29}$$

Inserting Eq. (28) into Eq. (29) results in,

$$\Gamma_A(\mathbf{q_1},\mathbf{q_2}) = \frac{1}{j\lambda}\int\int_{-\infty}^{\infty}\int\int_{-\infty}^{\infty}\overline{a(\mathbf{p_1})a^*(\mathbf{p_2})}\frac{exp[jk(r_{11}-r_{22})]}{r_{11}r_{22}}cos(\theta_1)cos(\theta_2)d\alpha_1 d\beta_1 d\alpha_2 d\beta_2. \tag{30}$$

Eq. 29 is then applied to the aperture plane speckle field, resulting in the aperture-to-observation plane relationship,

$$\Gamma_A((\mathbf{q_1},\mathbf{q_2}) = \frac{1}{j\lambda}\int\int_{-\infty}^{\infty}\int\int_{-\infty}^{\infty}\Gamma_a(\mathbf{p_1},\mathbf{p_2})\frac{exp[jk(r_{11}-r_{22})]}{r_{11}r_{22}}cos(\theta_1)cos(\theta_2)d\alpha_1 d\beta_1 d\alpha_2 d\beta_2. \tag{31}$$

Next, the assumption is made that the aperture plane speckle field ACF is sufficiently narrow that it can be represented by a delta function,

$$\Gamma_a(\mathbf{p_1},\mathbf{p_2}) = \kappa I(\alpha_1,\beta_1)\delta(\alpha_1-\alpha_2,\beta_1-\beta_2), \tag{32}$$

where $I(\alpha_1,\beta_1)$ is the spatial distribution of the speckle irradiance as a function of the local mean at the aperture and κ is a scalar constant. Making the trigonometric substitution $cos(\theta)=\frac{z}{r}$, where z is the on-axis propagation distance, the observation plane ACF simplifies to,

$$\Gamma_A(\mathbf{q_1},\mathbf{q_2}) = \frac{\kappa z^2}{\lambda^2}\int\int_{-\infty}^{\infty}I(\alpha,\beta)\frac{exp[jk(r_{11}-r_{22})]}{(r_{11}r_{22})^2}d\alpha d\beta. \tag{33}$$

This development of a speckle field ACF is valid on nonparaxial geometries due to its utilization of the RS diffraction integral and foundational to the development of the analytical speckle irradiance ACF utilized in the FPA resolution estimation methodologies introduced in Chapters IV and V.

2.4 Wigner Distribution Function

When analyzing electro-optic subsystems, it is often useful to represent a spatial signal, $X(\mathbf{q})$, by means of its frequency spectrum in the spatial frequency domain. A spatial signal's frequency spectrum can be determined via application of the Fourier transform,

$$\hat{X}(\mathbf{f}) = \int_{-\infty}^{\infty} X(\mathbf{q}) exp[-j2\pi \mathbf{f}\mathbf{q}'] d\mathbf{q}', \tag{34}$$

where $\hat{X}$ is the Fourier transform of X, $\mathbf{q}$ is the spatial coordinate pair (x, y) and $\mathbf{f}$ and is the spatial frequency coordinate pair (ξ, η). The frequency spectrum resulting from the Eq. (34) transform is a *global* signal representation as a function of spatial frequency. However, certain applications require description of a signal in terms of its *local* frequency spectrum. The WDF [53, 54] is a mathematical function which describes the local frequency spectrum of a signal.

2.4.1 Wigner Distribution Function: Definition

The WDF, $W(\mathbf{q}, \mathbf{f})$, of the signal $X(\mathbf{q})$ is defined as,

$$W(\mathbf{q}, \mathbf{f}) = \int_{-\infty}^{\infty} X(\mathbf{q} + \frac{\mathbf{q}'}{2}) X^*(\mathbf{q} - \frac{\mathbf{q}'}{2}) exp[-j2\pi \mathbf{f}\mathbf{q}'] d\mathbf{q}' \tag{35}$$

where the asterisk denotes complex conjugation, $\mathbf{q}'$ is a spatial coordinate pair and $\mathbf{q}$ is the coordinate pair of interest. The WDF can alternatively be defined in the frequency domain,

$$W(\mathbf{q},\mathbf{f}) = \int_{-\infty}^{\infty} X(\mathbf{f}+\frac{\mathbf{f'}}{2})X^*(\mathbf{f}-\frac{\mathbf{f'}}{2})exp[-j2\pi\mathbf{f'}\mathbf{q}]d\mathbf{f'} \tag{36}$$

where $\mathbf{f}$ and $\mathbf{f'}$ are spatial frequency pairs. The WDF represents signal in space and frequency simultaneously, forming an intermediate signal description between the space representation $X(\mathbf{q})$ and the frequency representation $X(\mathbf{f})$ of the signal of interest.

Properties of the WDF include:

- It is a real function.
- A space or frequency shift of the signal yields the same shift for its WDF.
- It is limited to the space interval and frequency range of the signal it is being applied to.

2.4.2 Wigner Distribution Function: Application to Stochastic Signals

The WDF can also be applied to stochastic signals. Suppose a random process, X is being analyzed. Applying Eq. (29) to the random process X results in an ACF, Γ_X, for the random process,

$$\Gamma_X(\mathbf{q_1},\mathbf{q_2}) = \overline{X(\mathbf{q_1})X^*(\mathbf{q_2})}. \tag{37}$$

The Wigner spectrum [55,56], W_S, is the expected value of the WDF and can be used to analyze the instantaneous spectral content of a non-WSS stochastic process [55,56].

$$W_S(\mathbf{q},\mathbf{f}) = \int_{-\infty}^{\infty} \Gamma_X(\mathbf{q}+\frac{\mathbf{q'}}{2},\mathbf{q}-\frac{\mathbf{q'}}{2})exp[-j2\pi\mathbf{f}\mathbf{q'}]d\mathbf{q'}, \tag{38}$$

Here, the Wigner spectrum describes the random process in terms of its positional power spectrum. The basic properties for the WDF are also applicable to the Wigner spectrum. This application to random signals is utilized in Section 4.3.3.1 to quantify the error associated with making WSS assumptions regarding the laser speckle random process.

2.5 Introduction to Experimental Detector Architecture and Device Performance Trade-offs

The focus of this research effort is to improve resolution estimation capabilities for emerging infrared FPA architectures. Experimental and analytical correlations between detector architecture and device performance are detailed in Appendix C. For reference, basic descriptions of bulk p-n photodiodes, strained-layer-superlattice (SLS) nBn III-V detectors and discussions of device differences are included in Appendix B. Prominent examples of device architecture impact on FPA MTF are highlighted. Detector design decisions and related device sensitivity effects, focusing mainly on dark current and QE are also investigated. Design investigations begin with comparisons of resolution performance between reticulated and unreticulated L3 bulk InSb devices [57], including discussion of L3's latest reticulated high operating temperature MWIR type-II nBn SLS devices [58] in Section C.1. Additionally, Section C.2 highlights Diagnostic/Retrieval Systems' (DRS) patented high-density vertically integrated photodiode (HDVIP) detector design [59, 60]. DRS modeling results demonstrate the need for full pixel reticulation to achieve ideal FPA MTF performance. Resolution and sensitivity estimation measurements from HRL's dual band nBn SLS FPA design [61, 62] are also discussed in Section C.3. HRL's results demonstrate the feasibility of high resolution nBn SLS detectors with decent sensitivity, if individually etched pixels are properly passivated with adequate dielectric materials. Finally, University of New Mexico's Professor Krishna and students investigated the effect of pixel reticulation on nBn SLS device dark current [63] in Section C.4. Results showed dark current differences between deep and shallow etched devices of an order of magnitude at 77K and a roughly 50% difference in favor of the swallow-etched devices at 150K. Krishna's results demonstrate the challenges associated with balancing FPA resolution and sensitivity performance when designing FPAs.

This device overview and related FPA performance challenges are presented to demonstrate the need for improving FPA resolution estimation capability, specifically for novel architecture, lambda scale infrared FPA. A majority of reviewed FPA resolution analysis was performed via modeling or indirect knife-edge estimates. Additionally, presented direct FPA MTF estimation attempts would benefit from unbiased validation. The following chapters are devoted to improving direct speckle-based MTF estimation techniques in support of understanding the resolution capability of various FPA designs.

2.6 Conclusion

This background supplied critical technical support for the research conducted in the following chapters. The concept of MTF was introduced, focusing on ideal detector assumptions and characteristics impacting resolution performance, specifically crosstalk. Next, an extensive set of FPA resolution methods was presented; the advantages and disadvantages of each technique were considered. After that, the analytical development of a laser speckle electric field ACF using RS diffraction integrals was described. Then, the WDF was introduced and presented with respect to stochastic processes. Finally, various IR detector designs were introduced, focusing on detector architecture and associated impact on device resolution. Subsequent chapters focus on the development of FPA MTF estimation methods, with the goal of accurately characterizing novel FPA devices like those presented in Section 2.5 and detailed in Appendix C.

III. Investigation of Speckle Imagery Spectral Estimation Challenges for Modulation Transfer Function Measurements

In order to apply adaptations of speckle-based focal plane array (FPA) modulation transfer function (MTF) estimation techniques introduced in Section 2.2.2.1 to infrared (IR) detector designs described in Section 2.5 and detailed in Appendix C, the speckle image power spectral density (PSD) estimation process must be optimized. The spectral estimation chapter explores various factors influencing the focal plane array (FPA) speckle imagery power spectral density (PSD) estimation process. This chapter is based on both a Society of Photo-Optical Instrumentation Engineers (SPIE) Defense and Commercial Sensing (DCS) Proceedings paper [64] and an SPIE Optical Engineering journal article [65] that was peer reviewed and published. This analysis influences key speckle testbed hardware decisions such as aperture size, aperture shape and microscanning hardware selection in Chapters IV and V. This estimation study also examines important periodogram estimation parameters, such as number of speckle images, periodogram window type and window size. These observations are incorporated into subsequent experimental FPA analysis efforts in Chapter IV.

3.1 Introduction

Laser speckle-based MTF methods have been utilized to determine resolution performance of FPAs since the mid-1980's [10, 27], as discussed in Section 2.2.2.1. MTF estimation success is dependent on accurately estimating the speckle image spectral content, in terms of PSD. Section 2.2.2.1 details numerous PSD estimation variations that have been attempted, such as one-dimensional fast-Fourier-transforms (FFTs) [6, 66], full image two-dimensional FFTs [12], use of various diffraction apertures [36, 38, 67] and segmenting and windowing of the image data [11]. The purpose of this chapter is to explore the benefits and disadvantages of these techniques using simulated random process inputs and actual infrared (IR) focal plane imagery. Additionally, the importance of signal-to-noise ratio (SNR) with regard to PSD estimation accuracy is also explored. MTF estimation is utilized to highlight the effectiveness of each investigated PSD estimation technique. The results will provide utility with regards to improving current and future estimation efforts.

3.2 Number of Image Realizations and Estimation Accuracy

PSD estimation accuracy is highly dependent on the number of independent measurement realizations available [68]. This section quantifies this idea using simulated laser speckle imagery and discusses the practical challenges encountered when attempting to increase the number of independent speckle instances in a particular measurement.

3.2.1 Simulation

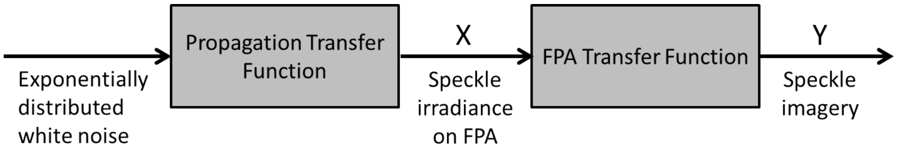

Figure 20: Block diagram outlining the process for simulating laser speckle and its transition through the FPA MTF estimation testbed. This analysis is reliant on conventional linear systems analysis

Simulation of speckle field generation, propagation and collection by a focal plane was accomplished by using an idealized linear systems approach. A block diagram illustrating the simulation's linear system chain is shown in Fig. 20. Delta-correlated random speckle was simulated as a random white noise exponentially distributed irradiance incident on a particular aperture. A free space propagation transfer function was chosen to generate speckle, X, with the appropriate second-order statistics at the focal plane, assuming valid Fresnel diffraction conditions. For the case of a square aperture, as shown in Fig. 21, the propagation transfer function is a product of triangle functions,

$$H_p(\xi,\eta) = \sqrt{tri\Big(\xi\Big/\Big(\frac{L}{\lambda z}\Big)\Big)tri\Big(\eta\Big/\Big(\frac{L}{\lambda z}\Big)\Big)}, \tag{39}$$

where L is the aperture width, λ is the wavelength of interest, ξ is the x-direction spatial frequency coordinate, η is the y-direction spatial frequency coordinate and z is the distance between the aperture and focal plane. Next, an additional transfer function describing an ideal FPA as an integral sampler of the input speckle irradiance, as introduced in Section 2.1.4, is displayed in Fig. 22,

$$H_{FPA}(\xi,\eta) = \left|\frac{sin(\pi\xi w_x)}{\pi\xi w_x}\frac{sin(\pi\eta w_y)}{\pi\eta w_y}\right|, \tag{40}$$

where w_x and w_y are the vertical and horizontal dimensions of the individual active detector elements. The scenario is established such that the input speckle irradiance is bandlimited and properly sampled by the FPA to avoid aliasing issues. The total combined system transfer function, $H_T(\xi,\eta)$,

$$H_T(\xi,\eta) = H_p(\xi,\eta)H_{det}(\xi,\eta), \tag{41}$$

which then leads to the relationship between the ideal measured speckle PSD and the input speckle PSD,

$$G_{out}(\xi,\eta) = G_{in}(\xi,\eta)|H_T(\xi,\eta)|^2. \tag{42}$$

When this transfer function is applied to the delta-correlated input speckle, the simulation outcome is the generation of laser speckle image realizations, Y, with the appropriate statistics for the simulated speckle testbed. Note this process linear systems relationship is only valid when the input random process is wide-sense-stationary (WSS). The development of Eq. (42) was completed in the continuous domain for reader ease. The simulation scenario is established such that G_{in} is bandlimited and properly sampled such that no aliasing occurs.

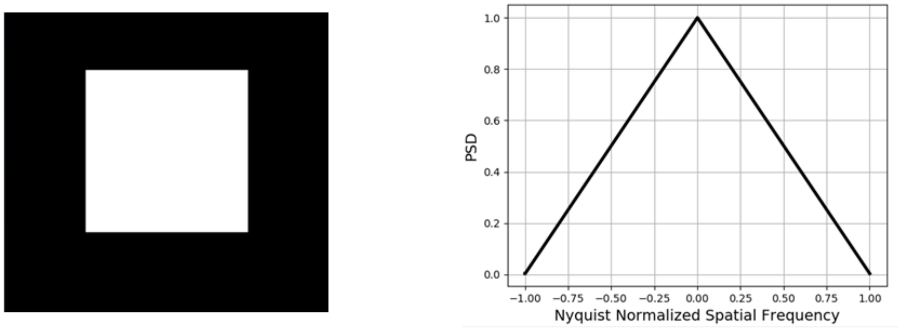

Figure 21: Image representing the square diffraction aperture and the associated one-dimensional transfer function, $H_p(\xi, \eta)$.

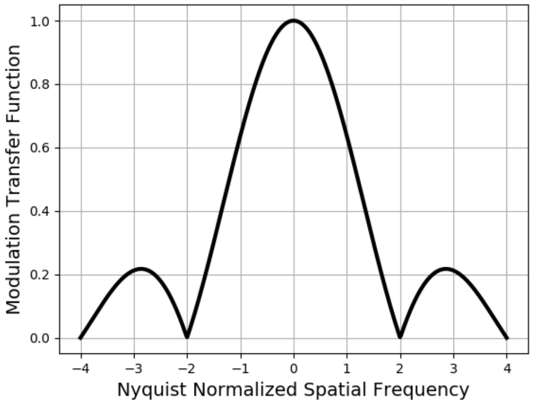

Figure 22: One-dimensional FPA modulation transfer function, $|H_{FPA}(\xi)|$. This MTF is representative an FPA with 100% fill factor ideal square detector elements.

In order to simulate the effects of various PSD estimation techniques, a number of speckle image irradiance realizations was generated and used as input to the linear system in Fig. 20. Simulated speckle images as measured by the ideal focal plane were then used to estimate PSDs similar to those measured in the laboratory setup described in Appendix A. This technique allows for a more streamlined approach than applying computationally complex field propagation integrals.

A mean square error metric, shown in Eq. (43), was chosen as a measure of performance for estimating the PSD of the simulated detected speckle irradiance,

$$G_{error} = \sum_{\xi_{min}}^{\xi_{max}} \sum_{\eta_{min}}^{\eta_{max}} \frac{[G_{out}(\xi_i, \eta_i) - \widehat{G}_{out}(\xi_i, \eta_i)]^2}{N}, \tag{43}$$

where $G_{out}(\xi, \eta)$ is the actual expected PSD and $\widehat{G}_{out}(\xi, \eta)$ is the estimated PSD and N is the total number of points in the PSDs. Using a standard periodogram averaging method for estimating the PSD, it is anticipated the variance, or error of the estimate, should decrease as a function of the number of periodograms averaged in the estimate. This is reflected in the mean square error as a function of the number of realizations used in the periodogram averaging, as demonstrated in Table 1.

Table 1: Number of realizations versus mean squared error, G_{error}, comparison. Increasing the number of independent realizations in an estimation effort decreases the estimate variance.

Number of Realizations	Mean Squared Error
10	0.02864
100	0.00165
1000	0.00020
10000	0.00003

The PSD estimates for these specific cases are shown in Fig. 23, illustrating the error impact compared to the actual expected PSD. The results reveal a high variance estimator when an insufficient number of realizations is utilized.

3.2.2 Number of Speckle Realizations Versus Estimation Approaches

The number and size of individual speckle realization images used to perform PSD estimations has varied dependent on the researcher's specific approach for speckle-

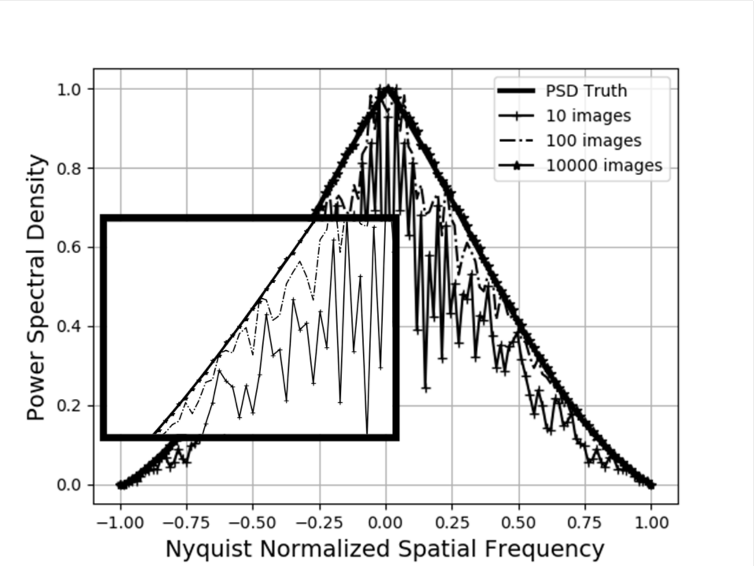

Figure 23: 1-D Slice of simulation of output PSD estimations, $G_{out}(\xi)$, with varying realizations. Increasing the number of independent realizations in an estimation effort decreases the estimate variance.

based FPA MTF estimation. Ducharme [12](100 images) and Chen [37](25 images) based their PSD estimation on full image, two dimensional techniques. This leads to high spatial frequency resolution PSD estimates, but a relatively low number of independent realizations [68]. Alternatively Barnard [11] used Welch's procedure [69], which involves dividing individual speckle images into overlapping segments, applying a window to each segment, calculating a periodogram from each windowed segment and finally ensemble averaging these periodograms to develop an output PSD estimate. Utilizing smaller windows reduces the spectral resolution and results in a biased estimate, however it significantly increases the number of realizations available per speckle image, reducing estimation variance. Both of these techniques were applied to the same 100 noise images, producing the output PSD estimates shown in Fig. 24. Mean squared errors between these estimates and the truth PSD were calculated and are displayed in Table 2, showing an eight-fold error decrease moving from the full image estimation technique to the segmented and windowed technique. Although the mean square error metric gives a general indication of estimate accuracy, it fails to capture the excessive estimate variance remaining when the standard periodogram averaging technique is used. It is important to mention that while both PSD estimation techniques were applied to a scenario featuring square aperture in this example, Ducharme [12] utilized a cross aperture in some measurement efforts to extend estimations beyond the FPA's Nyquist folding frequency. Section 3.5 investigates the application of these estimation techniques to other apertures.

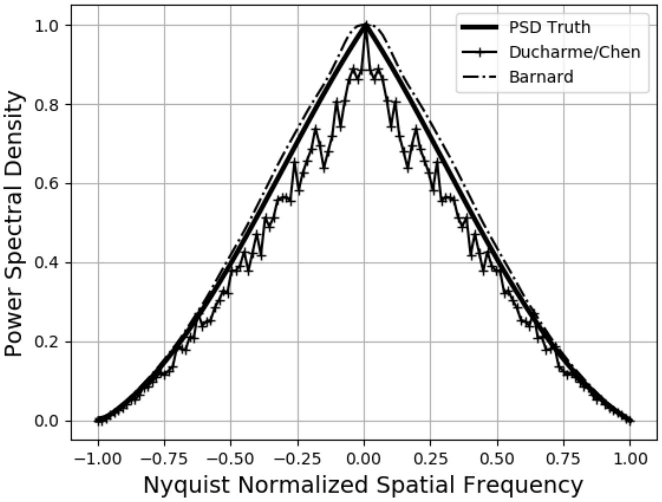

Figure 24: Visual comparison of output PSD, $G_{out}(\xi)$, estimation techniques. Welch's spectral estimation method used by Barnard produces a more accurate estimation than the full-image periodogram technique employed by Ducharme and Chen.

Table 2: Comparison of output PSD, $G_{out}(\xi)$, estimation techniques. Welch's spectral estimation method used by Barnard produces an estimation that is eight times more accurate than the full-image periodogram technique employed by Ducharme and Chen.

Estimation Type	Mean Squared Error
Barnard [11]	0.00058
Ducharme [12]/Chen [37]	0.00471

3.2.3 Practical Limitations of Increasing Independent Realizations

The simulation results in the previous sections highlight the importance of maximizing the number of independent speckle realizations when attempting to obtain accurate PSD estimates. A recent MTF estimation testbed configuration [11] synchronized a scanning mirror with image captures [11], attempting to capture independent speckle image realizations. Correlation analysis of this technique revealed high similarity between adjacent frames despite mirror scanning efforts [70]. These correlations are demonstrated in Fig. 25, where the horizontal and vertical axes represent the angular displacement of the mirror between image collections, each dot represents an image collection, and the dot color represents the correlation between the initial collected frame (bottom left dot) and the remaining frames in the image set. Due to the small angular displacement between samples, the adjacent frames are highly correlated. This correlation decreases as the angular displacement between mirror scans increases. Limitations in piezo-electric transducer (PZT) travel range constrain the overall angular spread that can be achieved on a per frame basis.

An obvious solution to the lack of independent realizations is simply to increase the number of independent frames used in the analysis. An earlier mid-wave IR (MWIR) testbed configuration [11] utilized an early MWIR quantum cascade laser (QCL). For these measurements, the coherence length of the laser was increased by incorporating an external grating in the optical path. Due to temperature fluctuations, this setup exhibited instabilities on the order of a tenth a second, thus limiting collection time lengths. Current QCL technology includes internal distributed feedback (DFB) systems, significantly increasing laser stability. This advancement allows for the potential of increasing the number of independent speckle images that can be collected for any MTF measurement given the extended length of time available for data collection.

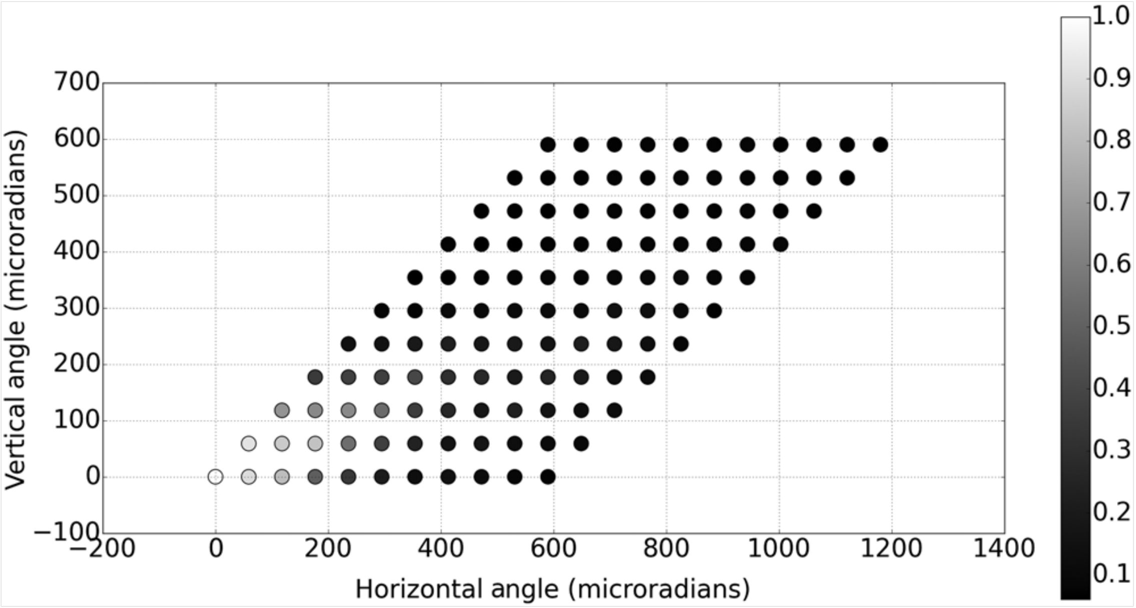

Figure 25: Correlation between images in a speckle set. Notice the high correlation between images collected at adjacent mirror positions. Significant angular displacement (200μ rad or greater) is required for the collection of independent image realizations.

Another practical limitation to increasing the number of speckle realizations collected with cryogenically cooled IR systems is the cold stop within the dewar restricting the number of usable image pixels. In a typical pour-filled dewar, the cold stop physically limits the spatial extent of the speckle field reaching the FPA, even though apertures as large as F/2 are typically used. In a typical high-definition (HD) format FPA (1280 × 720), an approximately 500 × 500 pixel image center is usable for analysis, as can be seen in Fig. 26 (b). Typical thermoelectric-cooled short-wave IR (SWIR) FPAs are mounted in less restrictive packages, leaving the entire array available for analysis, as shown in Fig. 26 (a). IR dewars add challenges to PSD estimations since smaller image sizes lead to fewer independent realizations, contributing to higher estimation variance.

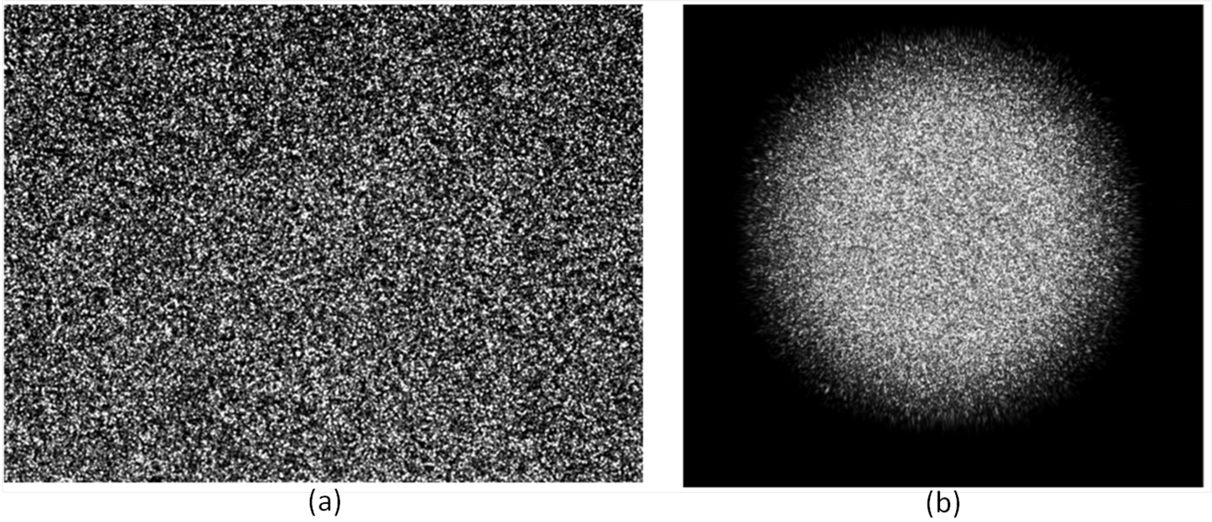

Figure 26: (a) Full SWIR speckle image compared to (b) full MWIR speckle image. The cold filter and shield limit the speckle field from impinging on the full MWIR focal plane. This limits the number of pixels available for analysis, lowering the number of realizations utilized on a per image basis when using Welch's estimation method.

3.3 Window Type

Windowing of speckle data segments is another output PSD estimation alternative with which researchers have experimented. Boreman [10], Sensiper [67], Ducharme [12] and Chen [37] opted to calculate their periodograms on full images without windowing, which in the spatial domain is essentially multiplying their speckle image with a rectangle function due to limitations of the focal plane size and shape. In the spatial frequency domain, this is the same as convolving the speckle's spectral content by the magnitude squared of a sinc function [69]. Barnard [11] utilizes a Hamming window in a effort to smooth out output PSD estimates and increase the independence of overlapping image segment realizations. The spatial and spectral representations of these filter options are shown in Figs. 27 and 28. Although the sinc filter offers a more desirable narrow mainlobe, leading to higher spectral resolution, it also suffers from significantly higher sidelobes, which can contaminate the measurement of the frequencies within the mainlobe.

To compare the rectangular and Hamming windowing techniques, PSD estimates were made on the same 100 noise images using conventional estimation techniques that utilize both types of windows. The first technique considered is Barlett's method [71], in which an image is split into non-overlapping segments, a periodogram is calculated from each non-windowed image segment and the periodograms are averaged, resulting in a PSD estimate. Welch's method, described in Section 3.2.2, was also used in this analysis. The results of this simulation, shown in Fig. 29, demonstrate the use of the Hamming window allows for a better overall match to the truth spectrum, especially at high spatial frequencies.

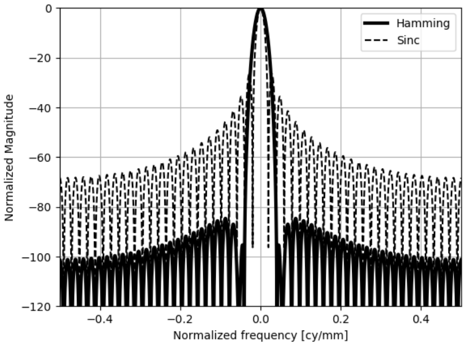

Figure 27: Frequency domain comparison of Hamming window and rectangular window-based image filtering techniques. The sinc-squared function has a more desirable narrow mainlobe, however its sidelobes are on the order of 10^5 times larger, greatly increasing the opportunity for spectral leakage.

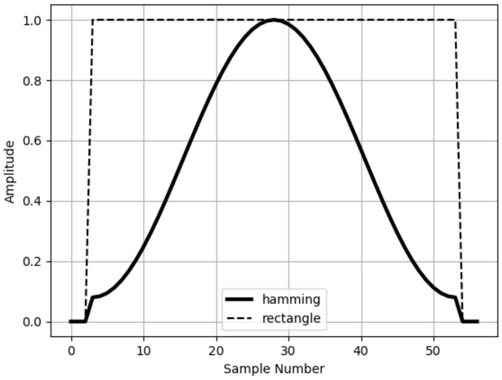

Figure 28: Comparison of the Hamming window and the rectangular window in the spatial domain. The Hamming window is a intentional estimation decision made by the user, whereas the rectangular window is a natural occurrence due to the physical limitation of the size of the focal plane under test.

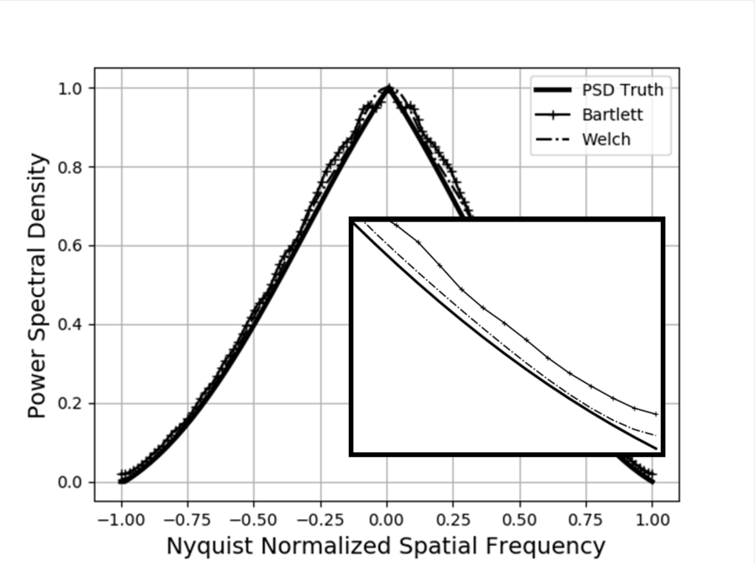

Figure 29: Output PSD, $G_{out}(\xi)$, simulation results: Hamming window versus no window. The use of the Hamming window produces more accurate PSD estimation results especially at vital high spatial frequencies.

3.4 Window sizes

Variation of realization segment size is another parameter in the spectral estimation trade space. Boreman's early speckle research [10, 27] involved one-dimensional periodogram estimations of 63×31 element FPAs. Sensiper [67] performed the same analysis on a 192×165 element FPA. Ducharme [12] and Chen [37] utilized full visible FPAs as their realization segments, both using single-digit megapixel sensors. Barnard [11] initially used a 1000×1000 sensor and split each image into smaller realization segments.

The obvious trade when considering which realization segment size to use for periodogram creation is balancing between resolution and number of total periodgrams. Larger segments lead to higher resolution estimates, but the use of more periodograms decreases the overall variance. If an unlimited number of realizations were available, a higher resolution estimate would be optimal. However, as demonstrated by Fig. 25, collecting large numbers of independent images can be challenging. Additionally, Fig.

26 shows that due to dewar and cold stops restricting light in MWIR and long-wave IR (LWIR) systems, full FPAs are not usable in the analysis, also limiting the number of available realizations.

Small non-uniformities in speckle image fields also add challenges, effecting the selection of realization segment size for analysis. Although an integrating sphere is utilized in most laser speckle testbeds as an attempt to generate uniform intensity laser speckle, spatial non-uniformities still exist. These non-uniformities are less apparent on a small image segment scale. However, on a full image scale, they introduce large DC offsets into the output PSD estimation. These large DC offset errors are apparent in output PSD estimations made from real MWIR speckle imagery shown in Fig. 30. Although higher resolution estimations are theoretically optimal, smaller realization segments are more robust to slight image non-uniformities, producing more accurate results. Note, although different window sizes were utilized for the estimations in Fig. 30, zero padding was applied to the FFT calculations to ensure a common spectral estimation size, allowing results to be easily plotted on the same graph. Considering that MTF curves are slowly varying and smooth in nature, making lower resolution estimates is appropriate for this particular application.

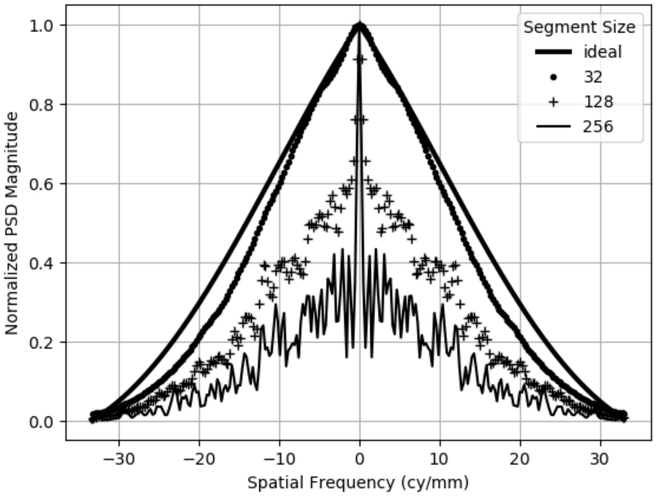

Figure 30: Output PSD, $G_{out}(\xi)$, estimation results with varying realization segment size. As the segment size increases, non-uniformities in the speckle image lead to erroneous output PSD estimations with significant increases in spectral content at DC.

3.5 Input Aperture Shape and Estimation Technique

Researchers have experimented with various apertures to propagate the laser speckle field to the FPA. The PSD of the laser speckle impinging on the surface of the FPA is the scaled autocorrelation of the diffracting aperture [32]. Ducharme [12] attempted to exploit the constant magnitude of the cross aperture's power spectral density over a broad range of spatial frequencies, shown in Fig. 31, to estimate the MTF of FPAs beyond their Nyquist folding frequency. Ducharme utilized a brute-force full image periodogram estimating technique to approximate the speckle image PSD. To explore whether Welch's method could improve spectral estimation accuracy of a speckle measurement featuring a cross aperture, a simulation was completed using 100 noise images. The square aperture propagation transfer function was replaced by a cross aperture and both Welch's method and brute-force periodogram estimations were attempted.

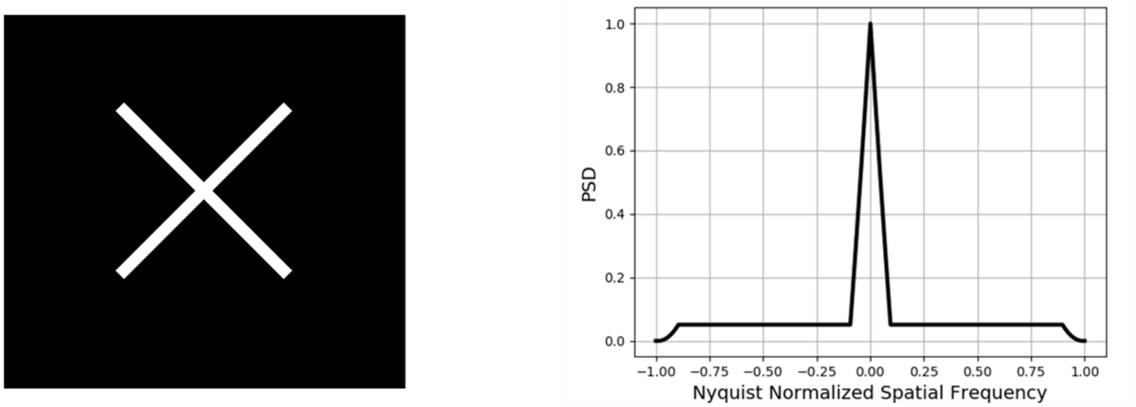

Figure 31: Images of a cross aperture function, left, and its associated one dimensional power spectral density $G_2(\xi)$, right. The power spectral density is the scaled autocorrelation of the aperture function.

The results of applying these estimation techniques, shown in Fig. 32 and Table 3, demonstrate that due to the sharp features of the PSD for a testbed featuring a cross aperture, Welch's procedure is not the optimal spectral estimator for this particular scenario. The windowing feature of Welch's procedure lends the technique towards being a better estimator for a smooth PSD, rather than one with abrupt changes. While the cross aperture seems potentially useful for high spatial frequency PSD estimations, the low input PSD magnitude at high frequencies coupled with the low speckle irradiance at the FPA's surface due to the narrow slits make PSD estimations challenging, especially in the presence of focal plane noise.

Table 3: Comparison of output PSD, $G_{out}(\xi)$, estimation techniques while using a cross-shaped diffracting aperture. The brute-force periodogram averaging technique is sixteen times more accurate in this given scenario.

PSD Estimation Technique	Mean Squared Error
Welch's Method	0.00897
Periodogram Averaging	0.00054

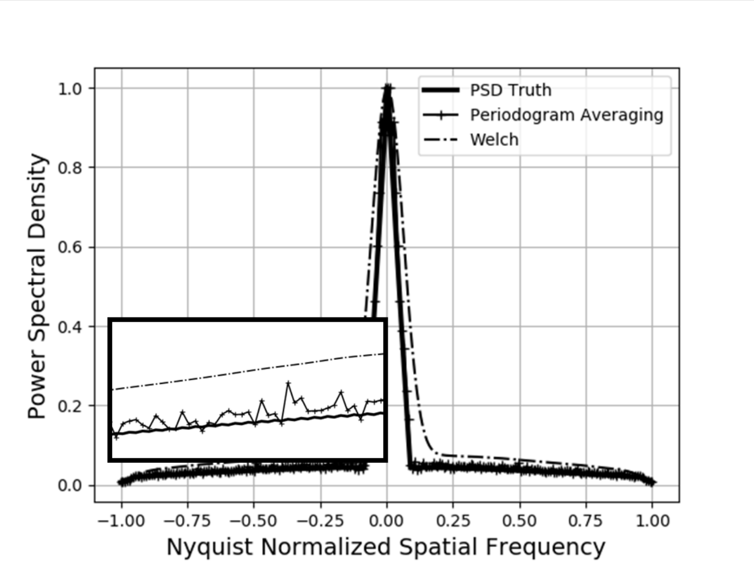

Figure 32: Comparison of output PSD, $G_{out}(\xi)$, estimation techniques using the cross aperture. Autocorrelation of the cross aperture generates a speckle input PSD, $G_2(\xi)$, with sharp features which are difficult to estimate when using Welch's procedure.

3.6 Testbed Noise Investigation

During the MTF estimation process, various noise sources impact measurement accuracy, including shot noise, dark current, Johnson noise, quantization noise and ROIC noise. This section explores the effect of noise sources on the PSD estimation process.

3.6.1 Laser Speckle SNR

Previous speckle contrast research [32,72] defines SNR as $SNR = \mu/\sigma$, where μ is the mean digital image count and σ represents the image's digital count standard deviation, which yields a constant when considering laser speckle images. The strength of the average intensity and intensity fluctuations are essentially equivalent in laser speckle imagery, with slight variation given the specific scenario geometry.

This conventional SNR definition treats laser speckle variance as the noise component in the SNR parameter, whereas in this specific testbed application, the laser speckle is actually the signal of interest. Since laser speckle irradiance on the FPA is a random process, its variance can be considered the signal AC power component [73] and its standard deviation can be utilized as the numerator in a more situation-appropriate SNR definition,

$$SNR = \sigma_{sig}/\sigma_{noise}, \tag{44}$$

where, σ_{sig} is the laser speckle signal standard deviation and σ_{noise} is the digital count standard deviation generated from non-signal-related sources, such as dark-current, analog-to-digital conversion, read-out electronics and Johnson noise. Goodman found the average number of photoevents generated per detector element can be represented as a negative binomial random variable in a free-space speckle propagation testbed [72]. An example propagation scenario is depicted in Fig. 33. This is due to the negative exponential distribution of the laser speckle intensity being conditional on the Poisson nature of the photon arrival process. The standard deviation of the average number of photoevents is,

$$\sigma_K = \hat{K}\sqrt{(\frac{1}{\hat{K}} + \frac{1}{M})}, \tag{45}$$

where $\hat{K}$ is the mean number of photoevents that occur on a detector element and M is the number of spatial degrees of freedom,

$$M = \left[\frac{1}{A_d^2}\int\int_{-\infty}^{\infty} K_D(\Delta x, \Delta y)|\mu(\Delta x, \Delta y)|^2\right]^{-1}, \tag{46}$$

where A_d is the area of a single detector element, $|\mu|^2$ is the spatial coherence function of the speckle field and K_D is the deterministic autocorrelation function of a detector element. Note σ_{sig} and σ_K are equivalent for this effort. Essentially, the impact of Poisson photon noise is masked by the negative exponential distribution of the laser speckle input.

A radiometric analysis of the speckle propagation scenario depicted in Fig. 33 begins with the calculation of the photon flux incident on the detector element,

$$\Phi_d = L_s A_s \Omega_d, \tag{47}$$

where L_s is the speckle field radiance passing through the diffracting aperture, A_s. Additionally, Ω_d is the solid angle subtended by the detector element. Paraxial approximations are appropriate in this scenario. The mean number of photoevents generated per detector element, $\hat{K}$, equals the photon flux incident on the detector element, Φ_d, multiplied by the detector quantum efficiency (QE), η_d. Utilizing the radiometric propagation scenario in Eq. (47) and combining all testbed geometry constants into one term, β, leads to the mean number of photoevents represented as,

$$\begin{aligned} \hat{K} &= \eta_d \Phi_d, \\ \hat{K} &= \eta_d L_s A_s \Omega_d = \beta A_s, \end{aligned} \tag{48}$$

highlighting its dependence on diffracting aperture area, A_s. Applying Eq. (48) to the signal standard deviation demonstrates the dependence of SNR on aperture area,

$$\sigma_{sig} = \beta A_s \sqrt{\left(\frac{1}{\beta A_s} + \frac{1}{M}\right)}. \tag{49}$$

3.6.2 Estimation Dependence on SNR

To investigate the effect of SNR and aperture area on PSD estimation, a nominal experimental testbed SNR was calculated as a simulation reference point. First, σ_{noise} was estimated by inserting an opaque cold stop in front of a representative

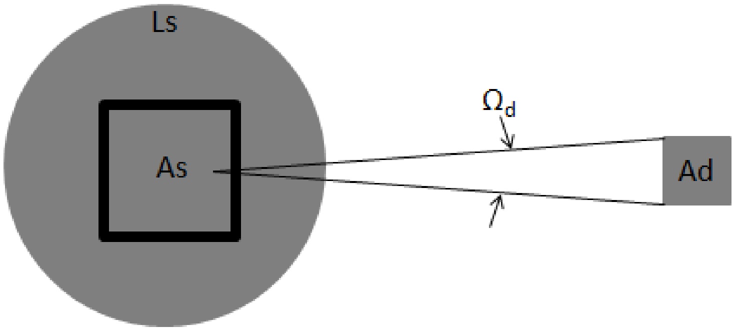

Figure 33: Geometry of laser speckle free-space propagation through a given diffracting aperture, A_s, to the detector element surface. The detector element active area, A_d, has been proportionally enlarged for clarity.

focal plane and measuring the digital counts collected with the system. Next, σ_{sig} was estimated using the variance of the central region of a speckle image similar to the one shown in Fig. 26, then subtracting σ_{noise} calculated in the previous step. These standard deviation parameters were then applied to Eq. (44), yielding a testbed SNR estimation of 180, which was used as a reference point for the following simulations.

Utilizing a square and cross aperture designed to have the same cutoff frequencies, a testbed-representative level of residual system noise, σ_{noise}, of 2.07 counts was added to each simulation and PSD estimations were made, as can be seen in Figs. 34-37. Note the cross aperture, demonstrated in Fig. 31, has approximately five times less aperture area than a rectangular aperture shown in Fig. 21, meaning the testbed SNR is approximately $\sqrt{5}$ times lower with the cross aperture than with the square aperture. Figs. 34-37 illustrate the PSD estimation results for square and cross apertures. As can be seen from the images, PSD estimations using testbeds with SNRs on the order of 100 are relatively unaffected by noise. However, the cross aperture measurement will be more susceptible to noise corruption due to its area disadvantage. Figs. 34 and 35 demonstrate Welch's procedure is a more accurate PSD estimation option when using the square aperture. In contrast, the sharp features of the cross aperture autocorrelation are unfavorable when used in combination with

Welch's spectral estimation procedure due to smoothing resulting from data windowing, as shown in Fig. 37. The brute-force periodogram estimation technique is a more accurate option for estimating the PSD of a testbed with a cross propagation aperture as Fig. 36 demonstrates. Table 4 lists the mean square errors of the above measurements, showing that when making output PSD estimations with a square aperture, Welch's spectral estimation technique delivers the most accurate results; however, brute-force periodogram averaging is the more accurate technique when a cross aperture is used.

Ultimately, the end goal of estimating output PSD, $G_{out}(\xi)$, is to estimate the corresponding MTF, or resolution performance, of the FPA under test. Eq. (50) is utilized to estimate the system MTF,

$$G_{out}(\xi) = G_{in}(\xi)|H_{FPA}(\xi)|^2, \tag{50}$$

where $G_{in}(\xi)$ is the PSD input into the system, $G_{out}(\xi)$ is the output PSD estimation from the speckle imagery and $H_{FPA}(\xi)$ is transfer function describing the focal plane. For simplicity, this analysis is completed in one dimension. Analysis is performed assuming a WSS input random process and a paraxial propagation geometry. Therefore, the assumption of the PSD being separable in Cartesian coordinates is valid. Utilizing the output PSDs, $G_{out}(\xi)$, estimated in Figs. 34-37 and appropriate theoretical input PSDs, $G_{in}(\xi)$, displayed in Figs. 21 and 31, FPA MTF estimations were made for each of the given scenarios. The resulting MTF estimates are displayed in Figs. 38-41. Given the testbed limitations of 100 speckle images per analysis, Figs. 38 and 40 demonstrate that brute-force periodogram averaging results in high variance MTF estimates. There are simply not enough speckle realizations available to produce dependable MTF estimations using the periodogram averaging spectral estimation technique. Fig. 41 highlights the discord between the sharp features of the

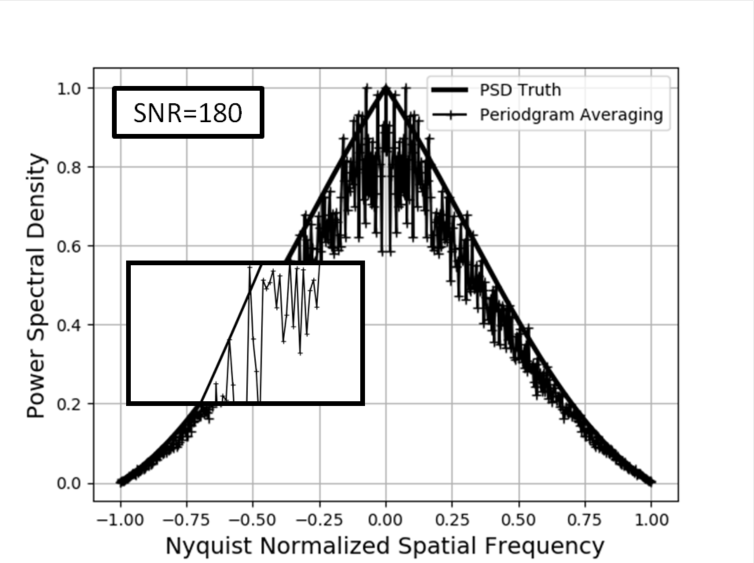

Figure 34: Estimation of laser speckle image's output PSD, $G_{out}(\xi)$, using a square propagation aperture, testbed-representative 100 noise images, brute-force periodogram averaging estimation technique and inputting representative sensor noise. The high variance due to the low number of periodogram realizations used. The minimal impact of added residual noise due to the high SNR scenario.

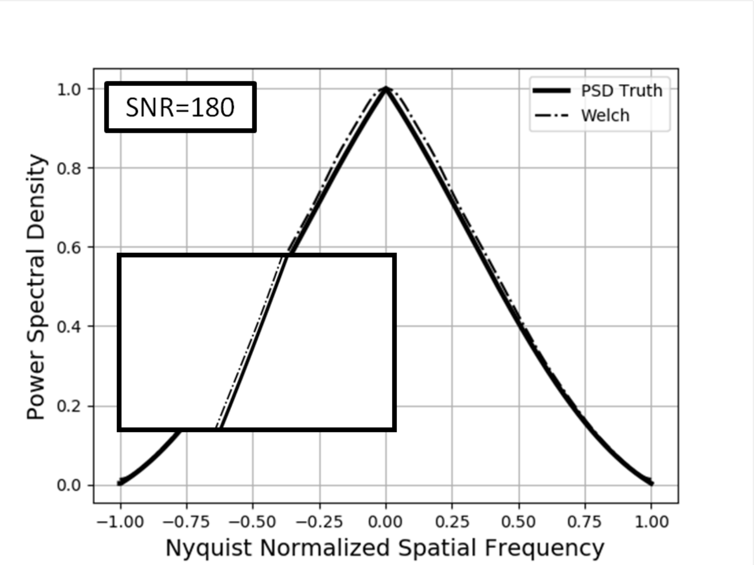

Figure 35: Estimation of laser speckle image's output PSD, $G_{out}(\xi)$, using a square propagation aperture, testbed-representative 100 noise images, Welch's spectral estimation technique and inputting representative sensor noise. The PSD overestimation near the zero spatial frequency due to a nonphysical condition related to the biased Welch's PSD estimation procedure. The minimal impact of added residual noise due to the high SNR scenario.

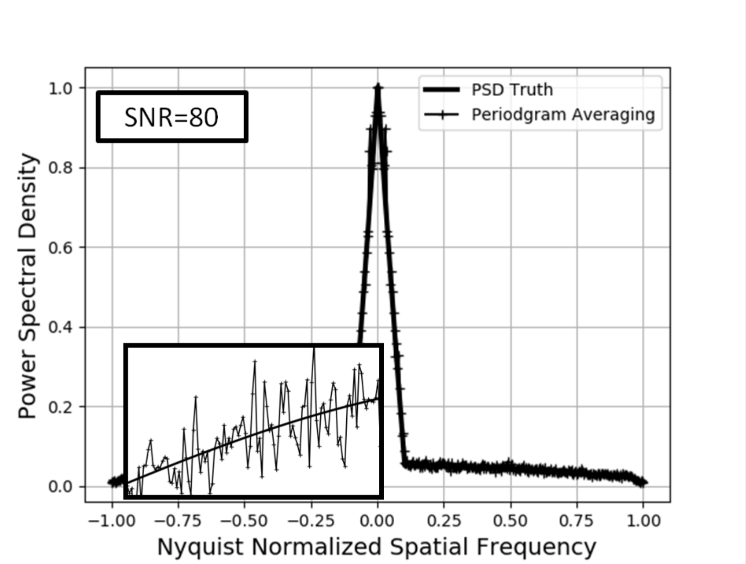

Figure 36: Estimation of laser speckle image's output PSD, $G_{out}(\xi)$, using a cross propagation aperture, testbed-representative 100 noise images, brute-force periodogram averaging estimation technique and inputting representative sensor noise. The periodogram estimation technique appears to accurately estimate the truth output PSD. The minimal impact of added residual noise due to the high SNR scenario.

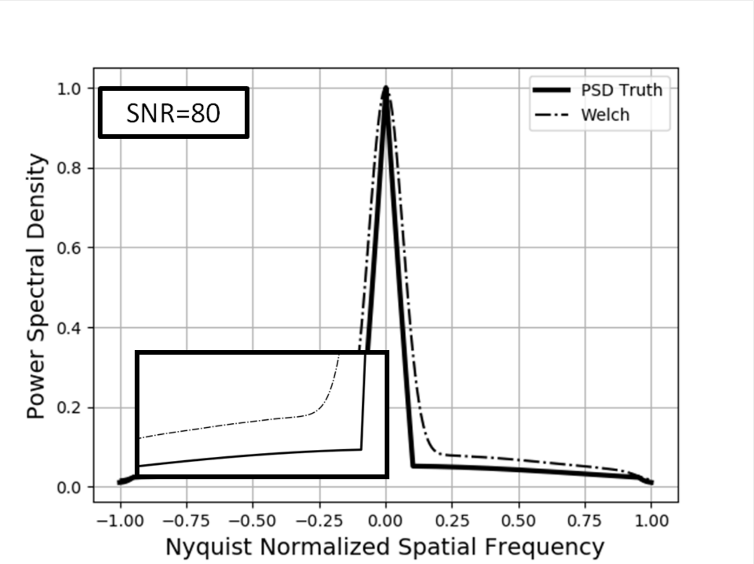

Figure 37: Estimation of laser speckle image's output PSD, $G_{out}(\xi)$, using a cross propagation aperture, testbed-representative 100 noise images, Welch's spectral estimation technique and inputting representative sensor noise. The sharp features of cross aperture autocorrelation are unfavorable when used in combination with Welch's spectral estimation procedure due to smoothing resulting from data windowing.

Table 4: Comparison of output PSD, $G_{out}(\xi)$, mean square errors using different spectral estimation techniques and propagation apertures. Results show that when making output PSD estimations with a square aperture, Welch's spectral estimation technique delivers the most accurate results, however brute-force periodogram averaging is the more accurate technique when the laser speckle is propagated with a cross aperture.

PSD Estimation Technique	Aperture Type	Mean Squared Error
Periodogram Averaging	Square	0.00883
Welch's Method	Square	0.00036
Periodogram Averaging	Cross	0.00029
Welch's Method	Cross	0.00686

cross aperture's autocorrelation and the data windowing and subsequent smoothing of Welch's spectral estimation procedure. This combination results in an inaccurate FPA MTF estimation. The most accurate MTF estimation given the testbed limitations is a combination of the square propagation aperture and Welch's spectral estimation technique, as demonstrated in Fig. 39. Notice the estimated MTF matches to within one percent of the truth MTF aside from an initial mismatch at DC due to a nonphysical condition related to the biased Welch's PSD estimation procedure [11]. Additionally the high spatial frequency mismatch results from a divide by zero condition induced by the use of Eq. (50) for estimation.

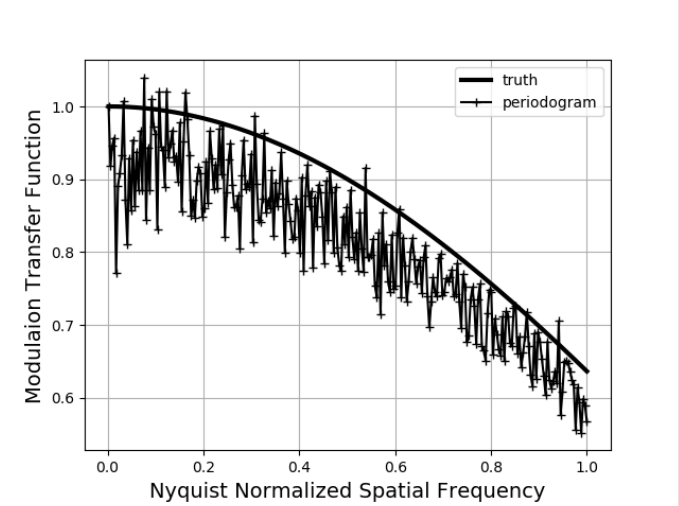

Figure 38: Modulation transfer function estimation of a simulated FPA using a square propagation aperture and brute-force periodogram averaging for output PSD, $G_{out}(\xi)$, estimation. The lack of realizations results in a high variance MTF estimate.

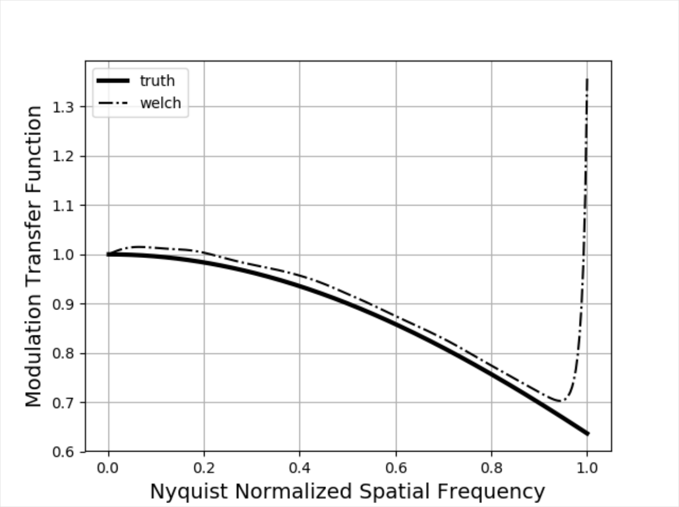

Figure 39: Modulation transfer function estimation of a simulated FPA using a square propagation aperture and Welch's method for output PSD, $G_{out}(\xi)$, estimation. The estimated MTF matches to within one percent of the truth MTF aside of an initial mismatch at DC due to a nonphysical condition related to the biased Welch's PSD estimation procedure. Additionally the high spatial frequency mismatch results from a divide by zero condition induced by the use of Eq. (50) for estimation.

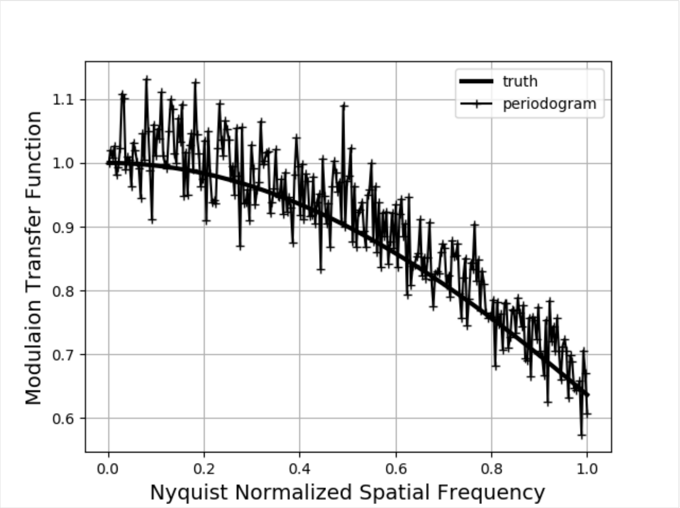

Figure 40: Modulation transfer function estimation of a simulated detector using a cross propagation aperture and brute-force periodogram averaging for output PSD, $G_{out}(\xi)$, estimation. The lack of realizations results in a high variance MTF estimate.

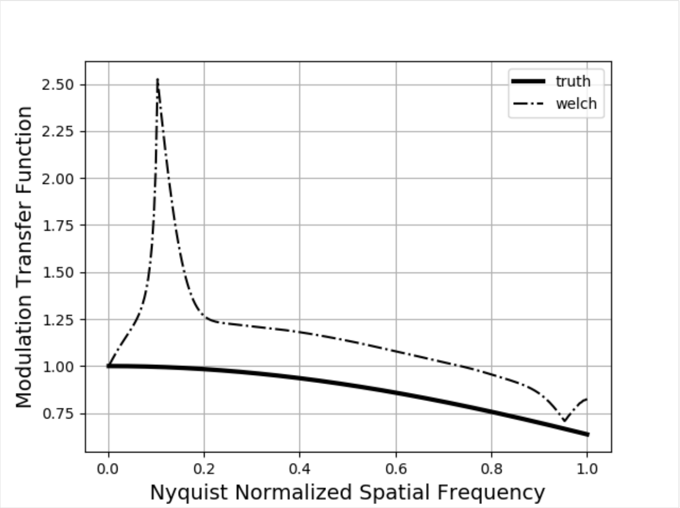

Figure 41: Modulation transfer function estimation of a simulated FPA using a cross propagation aperture and Welch's method for output PSD, $G_{out}(\xi)$, estimation. Fig. 37 demonstrates the overestimation of the sharp features of this particular input PSD due the data windowing and subsequent smoothing included in Welch's spectral estimation procedure. The final result is an inaccurate FPA MTF estimation.

3.7 Conclusion

Results of this analysis demonstrate the importance of utilizing as many independent realizations as possible when estimating speckle statistics such as PSDs, while at the same time emphasizing the real-world challenges associated with collecting independent realizations. This effort demonstrated that when estimating the spectral content of speckle images, making the tradeoff of increasing speckle image realizations via utilizing smaller image segments despite driving down estimation resolution is a fair compromise; this trade results in PSD estimations with lower variances and results that are more robust to image non-uniformities. The general slowly varying nature of an MTF curve allows for a lower resolution estimate.

Additionally, this effort investigated the impact of signal-independent noise and the utilization of different apertures have on spectral estimation accuracy. Theoretical results showed a larger area aperture allows more signal to reach the focal plane, leading to higher SNR measurements and more accurate PSD estimations. This is specifically important in thermal IR applications, where component expense and maturity make achieving high system SNRs more challenging.

Finally, the quality of the output PSD estimations were examined utilizing the resultant MTF estimation. Results show that given the testbed limitations of 100 speckle images per analysis, brute-force periodogram averaging results in high variance MTF estimates. In addition, the disconnect between the sharp features of the cross aperture's autocorrelation and the data windowing and subsequent smoothing of Welch's spectral estimation procedure result in inaccurate MTF estimations. The most accurate MTF estimation given the testbed limitations is a combination of the square propagation aperture and Welch's spectral estimation technique. The refinement of PSD estimation techniques accomplished in this chapter were applied to the Chapter IV experimental MTF estimation efforts.

IV. Generalized Focal Plane Array Modulation Transfer Function Estimation Approach for Non-Stationary Laser Speckle Random Processes

The generalized focal plane array (FPA) modulation transfer function (MTF) estimation approach chapter introduces a methodology for FPA MTF estimation for test geometries violating Fresnel approximation assumptions. This chapter is based on Society of Photo-Optical Instrumentation Engineers (SPIE) Optical Engineering paper currently in review for publication in Spring 2022. This paper presents a generalized approach for determining the FPA system input power spectral density (PSD), utilizing numerical evaluation of Rayleigh-Sommerfeld (RS) speckle irradiance autocorrelation functions (ACFs), speckle irradiance spectral analysis using the Wigner distribution function (WDF) and experimental error quantification incurred from making wide-sense-stationary (WSS) assumptions regarding the associated laser speckle random process. The effort's final result is an experimental demonstration of FPA resolution estimation technique in a non-paraxial test scenarios, using the generalized input PSD approach developed in this chapter, along with the output speckle image PSD estimation techniques optimized via the Chapter III analysis.

4.1 Introduction

Infrared (IR) detector technology continues to trend towards larger format FPA and smaller pixel pitch devices to support a broader span of increasingly demanding operational missions. Smaller pitch devices increase the potential for greater lateral carrier diffusion effects and subsequent device resolution performance degradation [74]. Strained-layer-superlattice (SLS) detectors, described in Appendix B, are an emerging IR device technology which have many potential advantages over historic IR detector materials and designs including: higher operability, better yield, theoretically lower dark current and lower manufacturing costs. However, SLS devices are a less mature technology than conventional IR detector materials with much higher horizontal-to-vertical carrier mobility ratios due to their structure [75], increasing the potential for lateral carrier diffusion issues. Pixel reticulation and passivation are options to maintain optimal resolution performance. However, minimizing these processes when possible is preferred considering their significant impact on device yield, which increases overall imaging system cost. The ability to directly measure the resolution of these small pitch SLS devices is vital to the design of high-performance, yet cost-effective imaging systems.

Laser speckle-based MTF estimation is an established direct FPA estimation technique [10, 36, 76]. More recently, this technique has been applied to measurement of the MTF of large format mid-wave IR (MWIR) FPAs [11, 70]. Implementation has relied on using Fresnel propagation to quantify the PSD of the speckle incident on the FPA, satisfying the small-angle approximation required to compute a closed-form solution. The inherent diffraction limitations in this methodology prevent utilization of this speckle-based approach for lambda scale FPAs, meaning the detector pixel pitch is approximately equal to the desired detection wavelength. This chapter presents a generalized approach for estimating the MTF of FPAs by utilizing scalar RS propagation and numerical computation of the incident speckle irradiance ACF on the FPA, which must be considered when the Fresnel approximation is violated. Spectral analysis based on applying the WDF [54] allows quantification of errors incurred from applying the conventional input-output PSD linear systems relationship requiring wide-sense stationarity of the laser speckle random process. Ultimately, this technique provides a method for determining the MTF for cases that would violate paraxial limitations imposed by the Fresnel approximation.

Section 4.2 introduces the numerical evaluation of the RS and Fresnel speckle irradiance ACF, which are used as the basis for the exploration of speckle ACF invariance within various test geometries. Next, the conventional Fresnel approximation constraints are discussed within the confines of a speckle FPA MTF estimation testbed. Then, the ACF numerical evaluation process is explained. Section 4.3 begins with a verification of the ACF computations. Next, the numerically evaluated RS and Fresnel ACFs are quantitatively compared for various propagation geometries. Then, the error due to the WSS assumption is quantified based on comparisons between the computed input PSD and the spectrum evaluated using the WDF. After that, the generalized FPA MTF estimation methodology is demonstrated experimentally on an optical testbed. Finally, Section 4.4 summarizes the physical regions where the demonstrated MTF estimation techniques are theoretically valid.

4.2 Theoretical Development

4.2.1 Speckle-based MTF Estimation/ACF Development

As described in Section 2.2.2.1, the conventional approach to speckle-based MTF estimation of FPAs assumes the detector and its associated read-out electronics to be a linear time invariant and spatially shift invariant system. Speckle is utilized as a wide sense stationary random process input into the FPA to characterize the system's transfer function [27], as shown in Eq. (15). In this analysis, G_{in} is typically determined analytically via a Fresnel diffraction-based development of the free space propagation geometry under analysis [32]. Section 2.3 describes Barnard's approach [11] to developing an analytical observation plane speckle field correlation function utilizing the RS diffraction integral. This theoretical development takes place in the continous domain for ease of reader understanding. Applying the Siegert relation [77] to Eq. (33), an analytical expression for the speckle observation plane irradiance ACF is developed as,

$$\Gamma_I(\mathbf{q_1}, \mathbf{q_2}) = \overline{I}^2[1 + \left|\frac{\Gamma_A(\mathbf{q_1}, \mathbf{q_2}}{\Gamma_A(0,0)}\right|^2]. \tag{51}$$

where $\overline{I}$ is the expected value of the speckle irradiance determined from the first-order speckle statistics. This formulation is valid so long as $r \gg \lambda$ and the delta correlated speckle assumption holds. Computation of Eq. (51) allows for investigation of the validity of ACFs computed with Fresnel approximations in non-paraxial geometries.

Development of a spatially invariant speckle field ACF involves applying the small-angle approximation [78] in Eq. (52) for the distance between aperture-observation-plane positions to Eq. (33),

$$r = z\left[1 + \frac{1}{2}\left(\frac{x-\alpha}{z}\right)^2 + \frac{1}{2}\left(\frac{y-\beta}{z}\right)^2\right], \tag{52}$$

where z is the propagation distance, (α, β) are aperture plane coordinates (Fig. 19 for reference) and (x, y) are observation plane coordinates. Application of this approximation results in the following speckle field ACF,

$$\Gamma_A(\Delta x, \Delta y) = \frac{\kappa}{\lambda^2 z^2}\int\int_{-\infty}^{\infty} I(\alpha, \beta) exp[-j\frac{2\pi}{\lambda z}(\alpha\Delta x + \beta\Delta y)]d\alpha d\beta, \tag{53}$$

and subsequent speckle irradiance ACF,

$$\Gamma_I(\Delta x, \Delta y) = \overline{I}^2[1 + \left|\frac{\Gamma_A(\Delta x, \Delta y)}{\Gamma_A(0,0)}\right|^2], \tag{54}$$

where $\Delta x = x_1 - x_2$ and $\Delta y = y_1 - y_2$. The function conversion from individual points in the observation plane to a generic $x - y$ separation distance demonstrates the function's spatial invariance. Since the ACF function is spatially invariant, the Wiener-Khinthine theorem is applicable and the speckle irradiance has a valid PSD, G_{in}, which can be used in Eq. (15) to evaluate the transfer function of the FPA under test.

4.2.2 Conventional Fresnel Approximation Constraints

To maintain the validity of Eq. (52)'s small angle approximation applied in Eq. (54), the propagation angle has typically been restricted to less than 10 degrees [11]. The propagation geometry is shown in Fig. 42, where L is the diffracting aperture width, D is the width of the FPA region of interest (ROI) and Θ_{max} is the maximum propagation half angle (MHA). Ref. 11 demonstrates the MHA can be derived via the relationship between the aperture width, FPA ROI and propagation distance. The width of the FPA ROI can be represented as $D = Nd_p$, where N is the number of detector elements in a single dimension and d_p is the FPA's detector pitch. Given $\xi_{spec} = \frac{L}{\lambda z}$ is the spatial frequency cutoff of laser speckle and $\xi_{Ny} = \frac{1}{2d_p}$ is the FPA Nyquist sampling frequency, setting $\xi_{spec} = \xi_{Ny}$ and performing some algebraic simplifications results in the MHA representation,

$$\Theta_{max} = tan^{-1}(\frac{1}{4}(\frac{\lambda}{d_p} + \frac{N\lambda}{L})), \tag{55}$$

where MHA is now dependent on wavelength. This λ-MHA comparison demonstrates how paraxial constraints limit applicability of the Fresnel approximation when lambda scale FPAs are the devices of interest. When lambda scale devices are considered under the presented speckle propagation geometry, the MHA is larger than the standard accepted 10° cutoff, as shown in Fig. 43. However, this angle limitation is subjective in nature and largely dependent on the application. To determine Eq. (15)'s applicability to lambda scale FPA resolution analysis, a quantitative analysis of the validity of ACFs computed with Fresnel approximations in the proposed scenario is required.

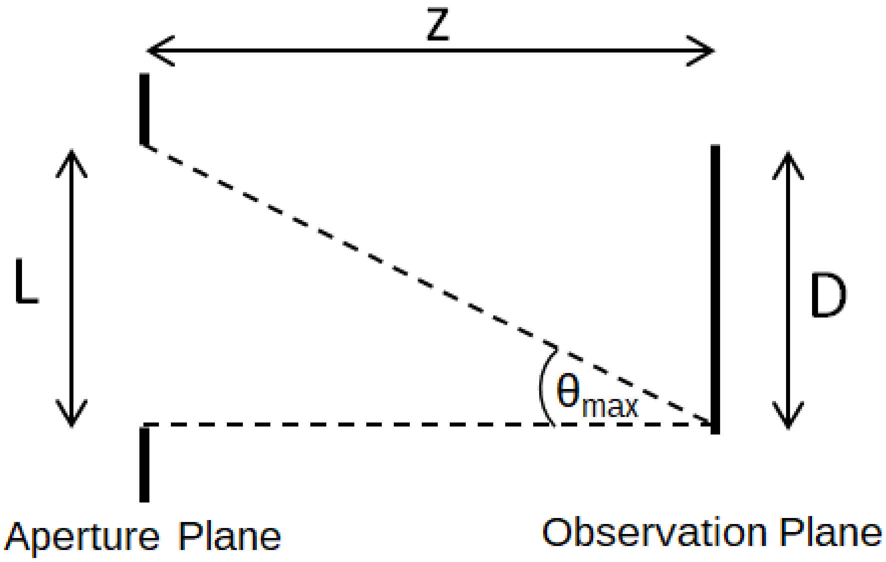

Figure 42: Simplified speckle propagation geometry highlighting the maximum propagation angle, Θ_{max}, between the aperture plane and observation plane.

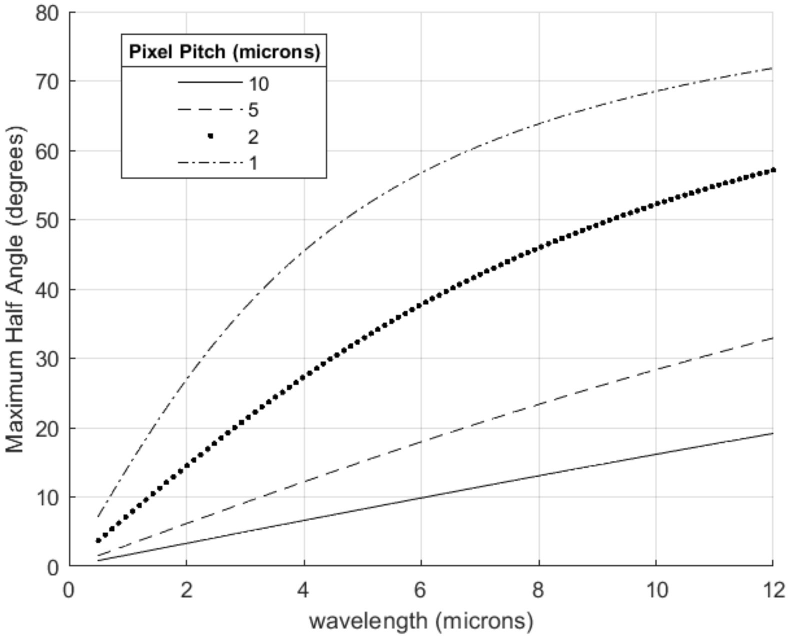

Figure 43: Maximum propagation angle versus wavelength for a 512 × 512 detector element observation plane, Nd_p, and a 32mm aperture width, L. Analysis of lambda scale FPA devices violates the conventional 10° limitation for Fresnel propagation.

4.2.3 Analytical ACF Computation

A numerical evaluation and comparison of speckle irradiance ACF functions computed with RS and Fresnel integrals was completed utilizing the Air Force Research Laboratory's High Performance Computing resources. High capability nodes featuring Intel Xeon Platinum 8168 cores with 384GB of memory and NVIDIA Tesla P100 GPUs were utilized to accelerate the calculations. Despite significant computational loads, a direct Huygens-Fresnel propagation [78] approach was chosen over alternative fast Fourier transform (FFT)-based propagation techniques to maximize accuracy.

To consider a realistic use case, a propagation geometry based on an actual speckle-MTF measurement testbed featuring a square diffracting aperture of length (L) 32.3 mm was simulated. The wavelength (λ) was set to 9.45μm to match an available quantum cascade laser (QCL). Propagation distances of interest ranged from 80mm to 200mm and were chosen to match specific detector active area widths, FPA ROIs and desired angular geometries. Since the ACF is spatially shift variant, on-axis observation plane ACFs were computed, along with off-axis observation plane ACFs ranging from $0.2L$ to $0.6L$ away from the on-axis location. The aperture and observation planes were sampled on a sub-λ grid to maximize ACF resolution. ACF computations via Eq. (51) involved selecting a central spatial coordinate pair, $\mathbf{q}_1$, then varying $\mathbf{q}_2$ to create a two-dimensional ACF. The typical run time for generation of a singular ACF was approximately three hours.

The ACF development in Section 4.2.1 was completed strictly with scalar diffraction theory, which decreases in accuracy when applied in off-axis geometries. Comparisons between scalar and vector diffraction theory [79, 80] demonstrate negligible differences between the two approaches with numerical apertures (NAs) less than or equal to 0.4. However, significant inaccuracies become apparent as scalar diffraction approaches are applied to scenarios where NA is equal to or greater than 0.5. The geometries analyzed here conform to scalar diffraction theory; other ACF development methods would need to be utilized if vector diffraction theory were required.

Shorter propagation distances were not considered due to the validity of Eq. (51) and Eq. (54). Specific to the ACF computed with the Fresnel integral, at propagation distances shorter than roughly two aperture widths, an empirically observed regime exists where speckle size is independent of diffracting aperture size [32]. In this region, the propagated speckle ACF becomes fixed in size, reaching a minimum size equivalent to the initial ACF function derived from the scattering surface's characteristics. Eq. (54) is no longer valid at these shorter propagation distances.

Additionally, the delta-correlated initial speckle field ACF assumption is invalid in both Eq. (51) and Eq. (54) at shorter propagation distances. The laser speckle ACF at the aperture is dependent on the surface characteristics used to generate it. The validity of a delta-correlated ACF assumption is dependent on the propagation geometry. An initial ACF function, representing laser speckle generated from an integrating sphere, was estimated using Infragold® profilometer data [81] and a simplified ACF model in Ref. 32,

$$\mu_a(\Delta\alpha, \Delta\beta) = \frac{exp[(-\sigma_\phi^2)(1-\mu_h(\Delta\alpha,\Delta\beta))] - exp(-\sigma_\phi^2)}{1-exp(-\sigma_\phi^2)}, \tag{56}$$

$$\sigma_\phi^2 = (\frac{4\pi}{\lambda})^2\sigma_h^2, \tag{57}$$

where σ_ϕ^2 is the phase shift variance, σ_h^2 is the surface height fluctuation variance and μ_h is the surface height ACF. The actual relationship between a surface microstructure and the statistics of its scattered wave is extremely complicated; it is influenced by surface slope and multiple scattering, among other variables. For the purposes of this analysis, this simplified model is utilized. A plot of this initial ACF function is shown in Fig. 44, demonstrating a width of approximately 10μm.

This estimate is in agreement with typical initial ACF observations [32]. The initial ACF is the speckle ACF at the aperture due to the IS and is fixed; propagated ACF widths vary with propagation distance from the aperture. Ref. 82's established a delta-correlated function assumption guideline for linear systems analysis, requiring a five times width difference between the output (propagated ACF) and input (initial ACF). For comparison, ACF computed at a propagation distance of 41mm was approximately 22μm wide; therefore the initial ACF in Figure 44 was deemed comparatively too wide for the delta-correlated assumption to hold. Similar comparisons were made at the propagation distances described above and presented in the forthcoming analysis. At these ranges, ACF function comparisons were in general agreement with Ref. 82's guideline. Therefore, the delta-correlated assumptions made in the following analysis were deemed valid and their associated error negligible.

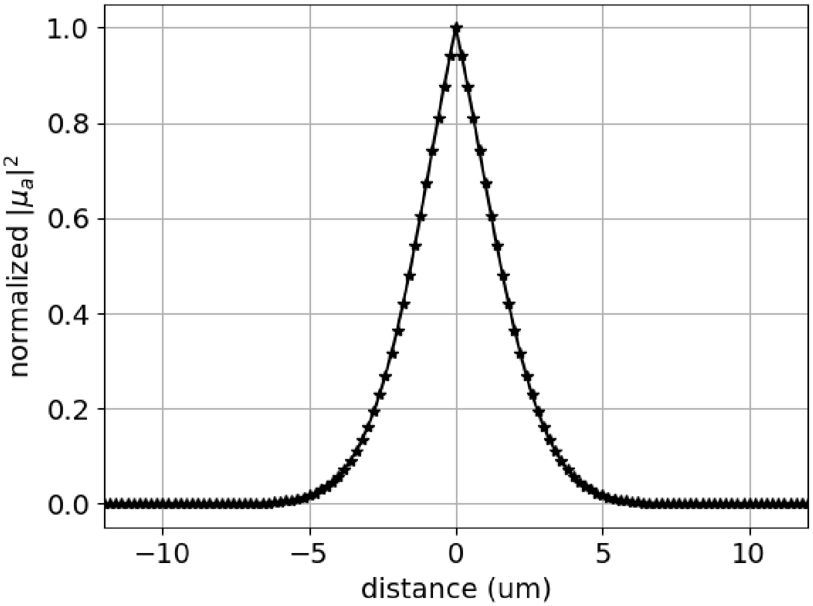

Figure 44: Simplified estimation of initial speckle field ACF width, demonstrating approximately a 10μm width. This initial ACF assumption is compared to propagated ACF computations to determine the delta-correlated assumption validity for the initial speckle field at various propagation distances.

4.3 Results

4.3.1 Validity of ACF Computation

The irradiance ACF computed via numerical evaluation of the Fresnel integral matches the analytical solution [32] of the Fresnel approximation to within 5×10^{-4} as displayed in Fig. 45(a). The ACF developed via numerical evaluation of the RS integral in Fig. 45(b) agrees to within 0.03 with the approximate Ref. 1 solution. Chu's approximate ACF solution is,

$$\Gamma_A \sim \frac{J_1(\alpha)}{\alpha}, \tag{58}$$

$$\alpha = kLcos(\theta)\frac{\Delta\theta}{2}, \tag{59}$$

where J_1 is the Bessel function of the first order, k is the wave number and θ is the angle between the observation plane's normal and the aperture plane center (θ in Fig. 19 on-axis). Chu demonstrates accuracy in comparison to similar speckle field ACF calculations in off-axis scenarios. Ward et al. [83] concluded that a straightforward analytical formulation for the off-axis ACF using the RS propagator cannot be derived. Comparison of Eq. (58) to the numerically evaluated ACF using the RS integral is shown in Fig. 45(b) to demonstrate the accuracy of the RS computation described in Sec. 4.2.3.

4.3.2 Fresnel-RS ACF Comparison

Two-dimensional ACFs generated from the numerical evaluation of the RS integral are shown in Figs. 46(a)-(d). Later results will be presented in one-dimension, specifically in the more informative off-axis direction, as it is easier for reader interpretation. These plots display the dependence of speckle size on $\lambda z/L$; the ACF

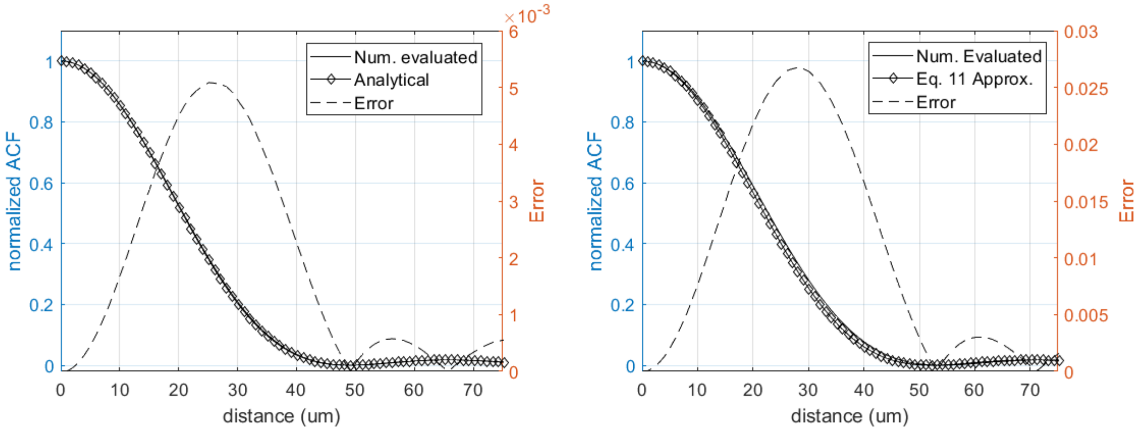

(a) (b)

Figure 45: Absolute error comparisons (a) analytical Fresnel ACF computation versus the numerical evaluation of the Fresnel integral, $\frac{L}{r} = 4$, on-axis. (b) Chu [1] approximation versus the numerical evaluation of the RS integral, $\frac{L}{r} = 4$, $MHA = 20°$. Numerically-evaluated results agree with analytical Fresnel ACF results and previously presented off-axis approximations.

width increases proportional to propagation distance.

One-dimensional ACFs at various propagation distances are presented in Figs. 47(a)-(d). Each plot features an on-axis ACF computed via evaluation of the Fresnel integral and a number of corresponding ACFs computed via evaluation of the RS integral, calculated at increasingly larger MHAs. Variation in on-axis and off-axis Fresnel ACFs are visibly negligible over the given geometries; only on-axis Fresnel results are plotted. Off-axis (y-direction) analysis distances were held constant per on-axis (z-direction) distance; variation in MHA is due to propagation geometry. Fresnel and RS ACF calculations converge at longer propagation distances, in geometries where small-angle approximations are commonly accepted as valid. More obvious ACF deviations are apparent at shorter propagation distances. For each graph, the first RS ACF plotted (for instance, the function labeled ”R-S/13.2°” in Figure 47(a)) corresponds to the on-axis calculation for the particular propagation distance. Variation between the on-axis RS and Fresnel ACFs at short propagation distances is primarily due to the non-paraxial wave propagation between the diffraction aperture outer

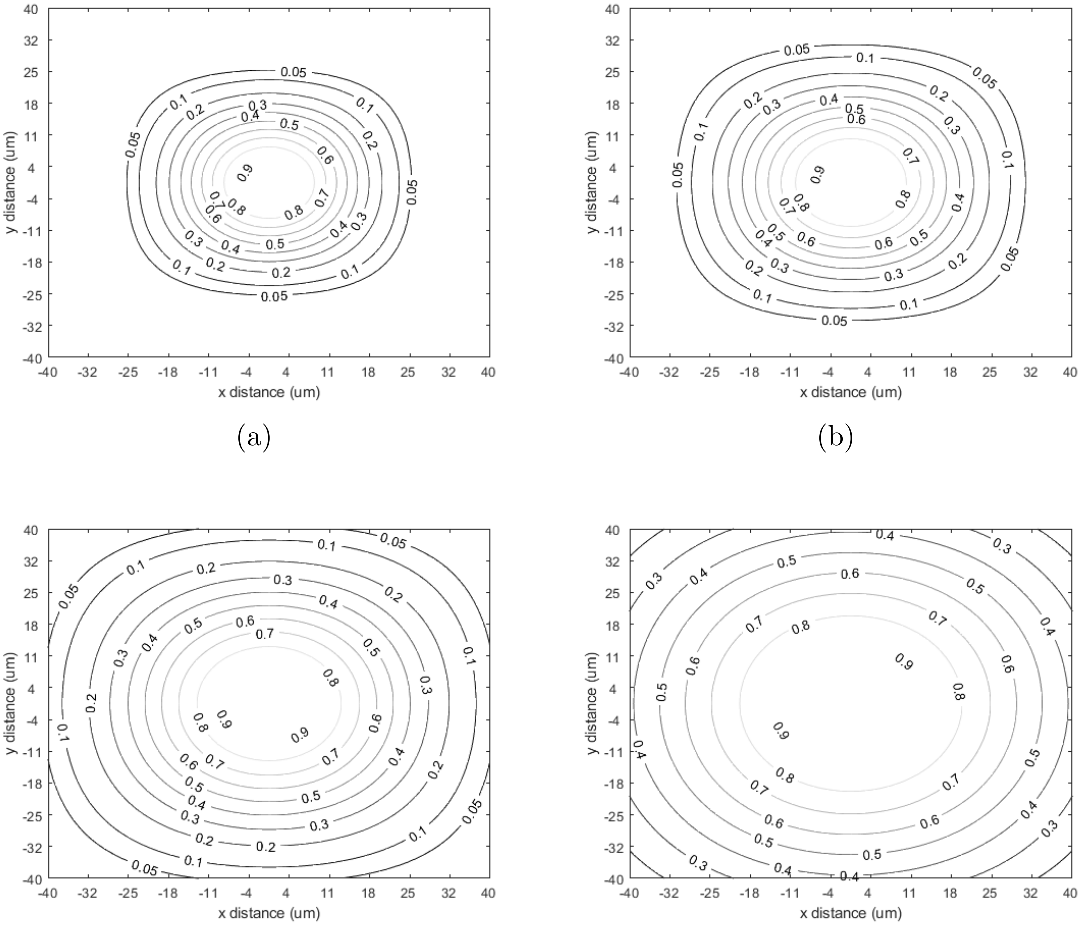

(a)

(b)

(c)

(d)

Figure 46: Two-dimensional ACFs developed via numerical evaluation of the Rayleigh-Sommerfeld integral (a)82mm, (b)100mm, (c)130mm, (d)200mm. These plots demonstrate the proportional relationship between the propagation distance and the ACF width.

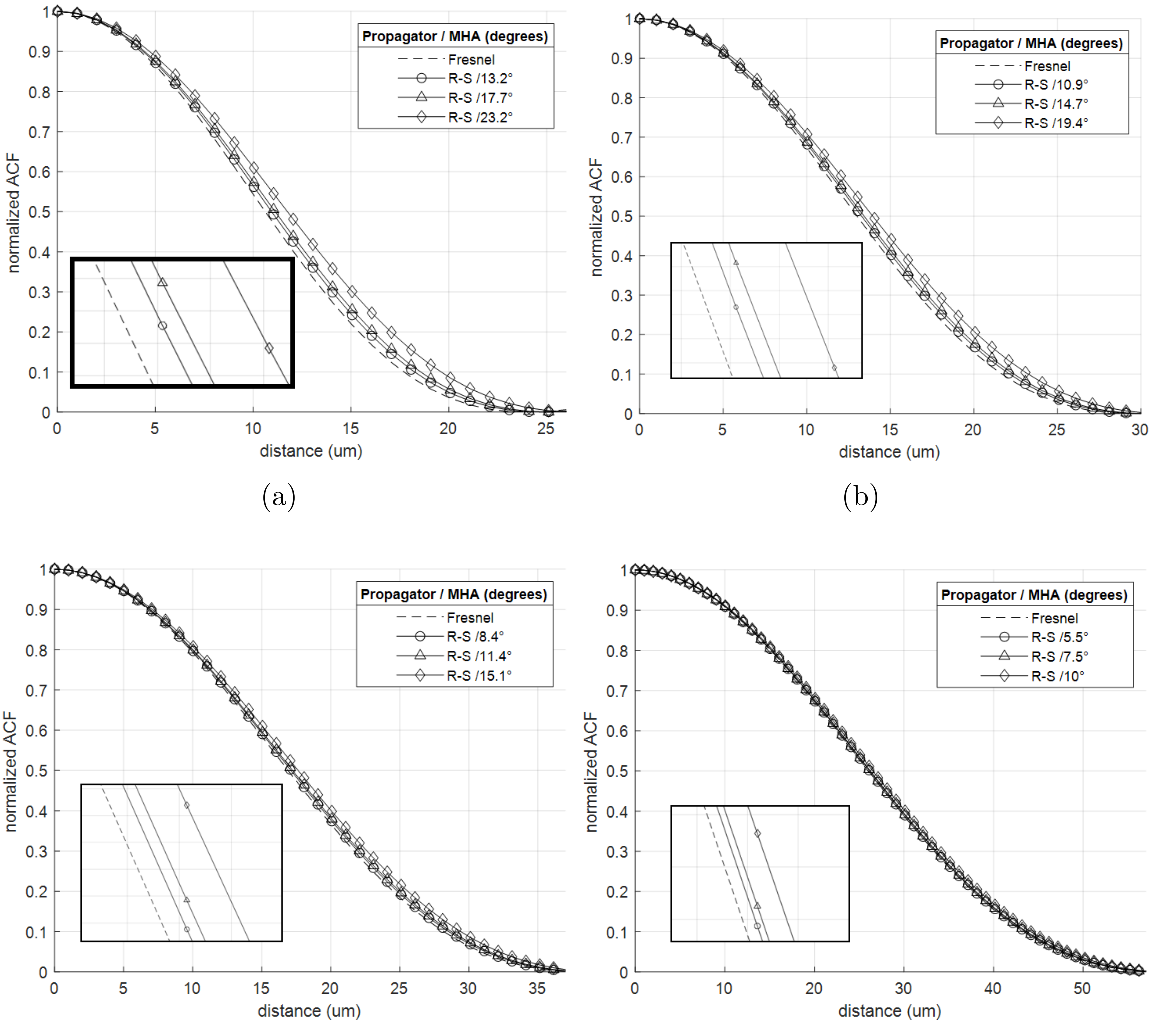

(a) (b)

(c) (d)

Figure 47: 1-D ACF plots at propagation distances (a)82mm, (b)100mm, (c)130mm, (d)200mm and maximum half angles of interest. These plots highlight the convergence of Fresnel and Rayleigh-Sommerfeld ACFs at larger distances and the divergence of the techniques closer to the aperture.

region and the observation plane center.

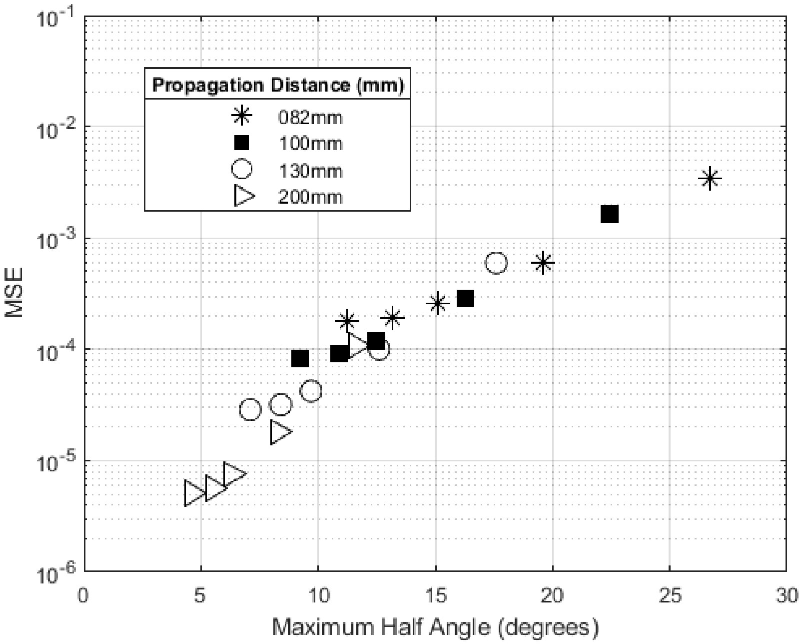

Figure 48: Mean square error between Fresnel and Rayleigh-Sommerfeld ACFs. No clear geometrical boundary delineates spatially shift variant from spatially shift invariant ACF data.

To quantify the difference between Fresnel and RS ACFs, a mean square error (MSE) was calculated at each off-axis location. The MSE versus the MHA is shown in Fig. 48, directly demonstrating the difference between the two propagation methods as a function of off-axis angle. As the MHA decreases, the deviation between the RS and Fresnel ACFs decreases as well. However, most significant takeaway from the comparison in Fig. 48 is there is no physical region, e.g., less than 10°, where a clear geometrical scenario boundary delineates spatially shift variant from spatially shift invariant ACF data or WSS conditions. This answer is dependent on the associated application's acceptable estimation error.

4.3.3 Spectral Estimation and Comparison

4.3.3.1 Methodology

As shown in the Section 4.3.2 ACF comparisons, some spatial variation exists at all propagation distances; therefore, any assumption of a true PSD will contain error. Random laser speckle cannot be considered WSS given this spatial shift variance; making such an approximation induces analysis error. To quantify this error, the Wigner spectrum [55, 56], W_S, which is the expected value of the WDF, is utilized to estimate the positional power spectrum [54] of the observation plane speckle irradiance. The Wigner spectrum [55, 56] provides a representation of the stochastic speckle irradiance in both space and spatial frequencies simultaneously,

$$W_S(\mathbf{q}, \mathbf{f}) = \int_{-\infty}^{\infty} \Gamma_I(\mathbf{q} + \frac{\mathbf{q}'}{2}, \mathbf{q} - \frac{\mathbf{q}'}{2}) exp[-j2\pi \mathbf{f}\mathbf{q}'] d\mathbf{q}', \tag{60}$$

where W_S is the Wigner spectrum, $\mathbf{f} = (\xi, \eta)$, and $\mathbf{q}'$ is a spatial coordinate pair and $\mathbf{q}$ is the central coordinate pair of interest. For the nonstationary speckle random process, the PSD is defined as the Fourier transform of the spatially averaged ACF [84,85]. The calculation of the PSD, $\overline{G}$, via the aforementioned relationship is shown,

$$\overline{G}(\mathbf{f}) = \int_{-\infty}^{\infty} \overline{\Gamma_I(\mathbf{q}')} exp[-j2\pi \mathbf{f}\mathbf{q}'] d\mathbf{q}', \tag{61}$$

where $\overline{\Gamma_I(\mathbf{q})}$ is the spatially-averaged ACF over the observation plane ROI. The maximum error induced by assuming $\overline{G}$ is from a WSS random process is quantified via comparison to the Wigner spectrum at the observation region limit, $\mathbf{q_{max}} = (x_{max}, y_{max})$. The Wigner spectrum computed at this spatial coordinate pair demonstrates the maximum possible spectral deviation from $\overline{G}$ throughout the ROI. Strict adherence to random process theory requires the input PSD to be from a WSS random process for the Eq. (15) linear system relationship to be valid. A relative PSD percentage error, $\epsilon_{WSS}(\mathbf{f})$, is computed to compare these functions,

$$\epsilon_{WSS}(\mathbf{f}) = \frac{|\overline{G}(\mathbf{f}) - W(\mathbf{q_{max}}, \mathbf{f})|}{\overline{G}(\mathbf{f})} * 100, \tag{62}$$

Note the equivalence of Eqs. 60 and 61 if the ACF centered about $\mathbf{q_{max}}$ is identical to the spatially averaged ACF, $\overline{\Gamma_I(\mathbf{q})}$. Both the WDF, W and the PSD computed via Fourier transform of the spatially-averaged ACF, $\overline{G}$, converge to a PSD from a WSS process when calculated using a spatially shift invariant ACF.

The PSD computation approach outlined here is a generalization of the previous closed-form input PSD solution based on the approximate analytical Fresnel calculation [11, 76]. As the propagation distance increases and the MHA decreases, both $\overline{G}$ and W converge towards the PSD computed via the approximated analytical Fresnel solution, i.e. a PSD of an WSS random process. Additionally, the proposed approach can be applied to any free-space laser speckle propagation scenario of interest to characterize the error associated with assuming $\overline{G}$ equivalent to a WSS-based PSD. An important outcome of this analysis is that even in paraxial conditions, there is always some deviation between $\overline{G}$ and the WSS-based PSD. This error is typically negligible in an experimental context as other errors, such as estimation error or windowing error, are more dominant.

4.3.3.2 Results

The methodology detailed in Section 4.3.3.1 was applied to ACF data computed at a propagation distance of 82mm. An observation region equivalent to a 512 × 512 ROI was utilized in this analysis. This scenario was chosen as it violates conventional paraxial approximation constraints and the laser speckle band pass cutoff spatial frequency approximately matches the Nyquist spatial frequency of available IR FPAs. To calculate Eq. (61), a sample of ACFs centered within the observation region was computed via discrete computation of Eq. (51). These ACFs were then averaged, generating $\overline{\Gamma_I(\mathbf{q})}$ for the observation region. The spatially-averaged ACF was then Fourier transformed to produce $\overline{G}$. Next, the WDF, $W(\mathbf{q_{max}})$, was calculated via the Fourier transform of the ACF centered on the observation region's furthest extent, (x_{max}, y_{max}). The PSD and WDF were compared via Eq. (62), producing the contour plot in Fig. 49. This error plot represents the maximum PSD deviation across the observation ROI. Excellent agreement between the computed WDF and PSD is visible; less than 3% on-axis deviation in spectral frequency is apparent across the observation ROI out to approximately 0.93 of the FPA Nyquist frequency. An on-axis percentage relative error slice, $\overline{G}$ and WDF centered about $\mathbf{q_{max}}$ are shown in Fig. 50. A critical analysis result is the application of $\overline{G}$ as G_{in} in the Eq. (15)'s linear systems analysis will have a minimal and quantifiable effect on the experimental outcome. Despite $\overline{G}$ being from a non-stationary random process, its utilization is not the dominant experimental error source, as results in Section 4.3.4 will demonstrate.

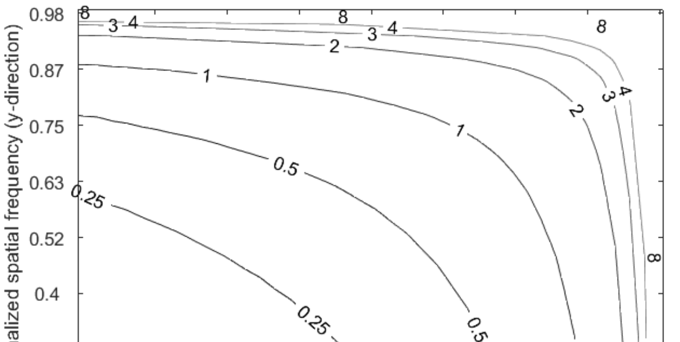

Figure 49: 2-D percentage relative error, $\epsilon_{WSS}(\mathbf{f})$, between the Wigner spectrum at the observation ROI edge and PSD computed via spatially averaged ACFs. Less than 3% on-axis deviation in spectral frequency is apparent across the observation ROI out to approximately 0.93 of the FPA Nyquist frequency.

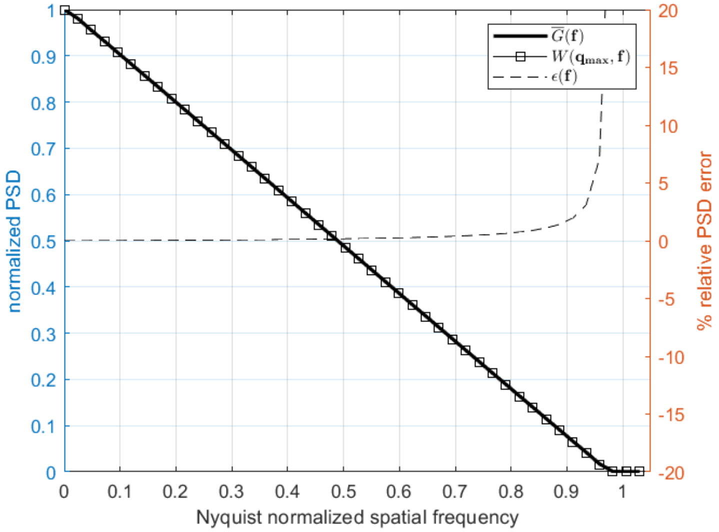

Figure 50: 1-D percentage relative error between the WDF at the observation ROI edge and PSD computed via spatially averaged ACFs. Less than a 3% relative error percentage between WDF at the observation ROI edge and the Eq. 61 PSD out to approximately 0.93 of the FPA Nyquist frequency, is displayed.

4.3.4 Experimental Analysis

The generalized methodology and theoretical calculations were experimentally demonstrated on an optical testbed. A more detailed description of the speckle testbed, data collection and processing procedures is included in Appendix A. This testbed featured an Adtech 9.45μm distributed feedback QCL source. The laser beam was input into a Labsphere 8" Infragold® integrating sphere (IS). The IS's rough surface generates the laser speckle and the IS's structure creates a uniform speckle irradiance distribution across its output port. A chemically etched, 32.3mm square diffracting aperture was placed at the IS's output port. The laser was mounted on a Thorlabs NRT-150 motorized lateral translation stage and a Zaber X-VSR20A motorized vertical translation stage. The motion provided by these stages was synchronized with the frame captures to generate independent speckle realizations required for accurate statistics. A long-wave linear polarizer was placed just past the diffracting aperture to generate the polarized speckle required for the experiment [32]. The FPA was mounted in a pour-filled dewar with a 1" diameter Spectragon narrow band (∼240nm full width half maximum) filter, centered at the laser wavelength, as the cold stop in an F/2 configuration. This specific filter was chosen to minimize experiment noise due to significant background radiation. The dewar was placed such that the propagation distance between the diffracting aperture and FPA was 87mm, allowing demonstration of the generalized methodology in a non-paraxial test geometry. Additionally, laser speckle data was collected at propagation distance of 110mm, creating a test geometry (10° MHA) where Fresnel assumptions are valid and the closed-form input PSD solution based on the approximate analytical Fresnel calculations can be utilized.

4.3.4.1 Output PSD Estimation and Input PSD Computation

PSD estimations using the generalized methodology described in Sec. 4.3.3.1 and the Fresnel approximation methodology [11] are shown in Figs. 51(a) and 51(b). 1-D output PSD slices in the x- and y-directions are shown for propagation distances of 110mm (Fig. 51(a)) and 87mm (Fig. 51(b)). The estimation of output PSDs consisted of collecting 16 independent speckle images. The central 512×512 pixel ROI of each image was utilized in calculations. Two dimensional PSD estimations were made via Welch's procedure [69], specifically utilizing a 50% overlap between adjacent realizations and a 31-element Hamming window to reduce the estimate variance. A block diagram of teh output PSD estimation procedure is presented in Fig. 66 Also shown in Fig. 51(a) is a 1-D slice of the PSD input into the FPA, determined by the appropriate approximate analytical Fresnel calculation based on the test geometry. A 1-D slice of $\overline{G}$, calculated following the process detailed in Section 4.3.3.1, is also demonstrated in Fig. 51(b). The cause for the output PSD residual noise floor at spatial frequencies greater than the input PSD cutoff is a combination of experimental noise sources (ROIC, dark current, system test electronics, etc.) which are not fully investigated in this effort. Notice the PSD cutoff differences between the two methodologies, with the Fresnel approximation method cutting off at 0.72 Nyquist and the generalized methodology cutting off at 0.9 Nyquist. These PSD cutoff differences are a primary cause of the spatial frequency range differences between the two MTF estimation methodologies.

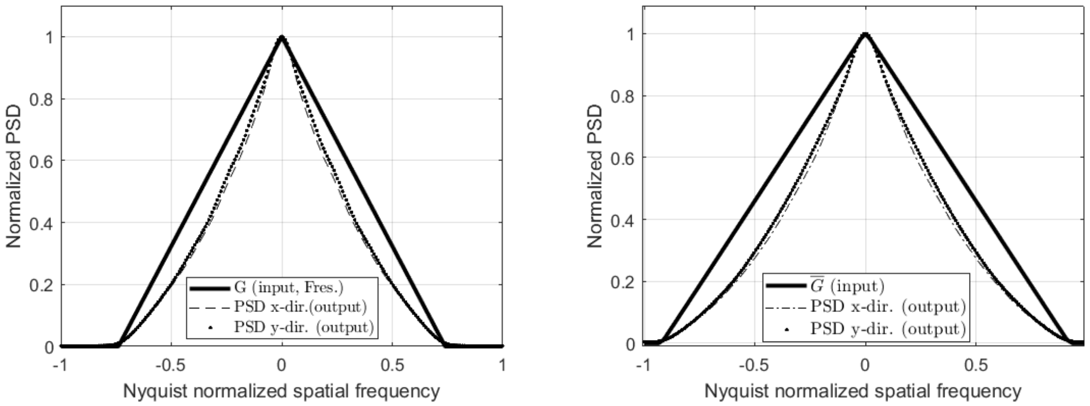

(a) (b)

Figure 51: (a) 1-D slices of estimated output PSDs and an input PSD calculated via closed form solution based on approximate analytical Fresnel solution, (b) 1-D slices of estimated output PSDs and an input PSD calculated via application of generalized PSD methodology described in Section 4.3.3.1

4.3.4.2 Output PSD Estimation Window Bias

As detailed in Section A.3.2, output PSDs are estimated using Welch's procedure. This estimation effort involves applying a Hamming window to each independent speckle image segment prior to periodogram estimation. The Hamming window enables a smooth output PSD estimate, but also induces an estimation bias. The impact of this bias on output PSD estimation was studied in [70], using a theoretical input PSD, ideal FPA MTF and a Hamming window. The MTF error due to the windowing bias was determined by calculating the relative error between the true ideal output

PSD, $G_{out-ideal}(\mathbf{f})$, which is calculated via application of Eq. (15) and the expected value of the biased PSD,

$$E[\hat{G}_{W-out}(\mathbf{f})] = \frac{1}{(2\pi)^2}\left|W_{Ham}(\mathbf{f})\right|^2 ** G_{out-ideal}(\mathbf{f}), \tag{63}$$

$$\epsilon_{window}(\mathbf{f}) = \frac{\left|\sqrt{\frac{1}{(2\pi)^2}\left|W_{Ham}(\mathbf{f})\right|^2 ** G_{out-ideal}(\mathbf{f})} - \sqrt{G_{out-ideal}(\mathbf{f})}\right|}{\sqrt{G_{out-ideal}(\mathbf{f})}}, \tag{64}$$

where E is the expected value operator, $\hat{G}_{W-out}(\mathbf{f})$ is the average windowed periodogram PSD estimate of the ensemble of windowed segments, $W_{Ham}(\mathbf{f})$ is the Hamming window in the frequency domain, $G_{out-ideal}(\mathbf{f})$ is the desired true PSD measured by the FPA and $\epsilon_{window}(\mathbf{f})$ is MTF error due to the window bias. A normalized frequency domain representation of the Hamming window is shown in Fig. 27. The Eq. (64) error is calculated in terms of the square root of both the truth and biased PSDs, allowing for error representation in terms of MTF. This error calculation was applied to both of the aforementioned test geometries, using the appropriate input PSDs computed for each scenario.

Figure 52 displays the percentage MTF error due to window bias for both the Fresnel and nonparaxial generalized geometeries as a function of spatial frequency. Additionally, a 3% MTF error threshold is plotted. This error threshold was determined via empirical measurements. Generally, MTF error threshold is application and scenario specific. For the purpose of this analysis, a 3% MTF error threshold was utilized. The difference in MTF errors between the Fresnel test geometry and nonparaxial test geometry attributed to the analytical PSD shapes displayed in Figs. 51(a)-51(b), especially the spatial frequency cutoff. This 3% error threhold due to the estimation window bias was computed and incorporated into the MTF estimation results displayed in Figs. 53(a)-53(b).

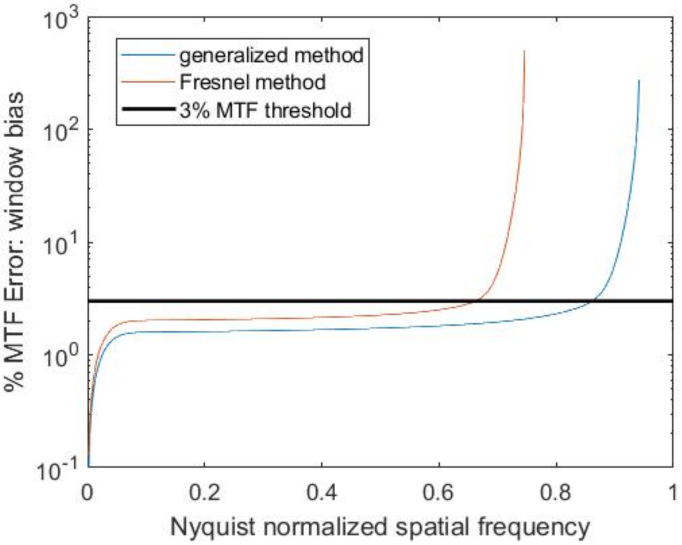

Figure 52: 1-D slice percentage relative error due to PSD output estimation window bias. A 3% MTF error threshold is reached at 0.67 Nyquist for the Fresnel analysis geometry and 0.85 Nyquist for the nonparaxial generalized analysis geometry. This 3% error threshold due to the estimation window bias is incorporated into the MTF estimation results displayed in Figs. 53(a)-53(b).

4.3.4.3 MTF Estimations with Experimental Errors

MTF estimations using the generalized methodology and the Fresnel approximation methodology are shown in Figs. 53(a) and 53(b). X-direction slices are shown in Fig.53(a) and y-direction slices are shown in Fig.53(b). Three MTF curves are shown in each figure. The solid line is an ideal sinc MTF for a 100% fill factor pixel with the same pitch as the device under test. The dash-dotted line is the MTF estimate using the generalized method, derived from the application of the input and output PSDs in Fig. 51(b) to the linear systems relationship in Eq. (15). The dotted line is the MTF estimation using the Fresnel approximation method, which is derived from the application of the input and output PSDs in Fig. 51(a) to the linear systems relationship in Eq. (15).

Additionally plotted in Figs. 53(a) and 53(b) is a series of vertical error lines, which serve as MTF estimation validity limits based off critical experiment details.

The line located at 0.67 Nyquist represents the 3% error threshold for the Fresnel approximation method based on the error induced via application of a Hamming window in the output PSD estimation process, as described in Section 4.3.4.2. The vertical line at 0.85 Nyquist represents the 3% error threshold for the generalized method also due to the aforementioned window error. The line at 0.9 Nyquist is the 3% MTF error threshold due to the WSS assumption of $\overline{G}$, specific to the generalized methodology. The WSS assumption error is calculated via the same process as Eq. (62), but using the square root of the PSD and the WDF, expressing the result in terms of an MTF error. Using the demonstrated 3% error lines as boundaries for MTF estimation validity, the results show a 27% (0.67 Nyquist to 0.85 Nyquist) improvement in MTF spatial frequency range between using the generalized and Fresnel approximation methodology for this test scenario.

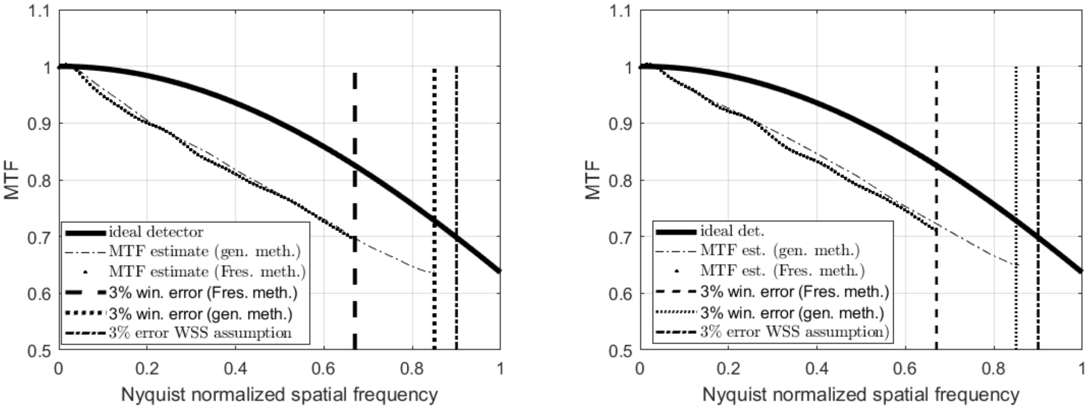

(a) (b)

Figure 53: (a) 1-D x-direction slices of estimated MTFs via the generalized method and the Fresnel approximation method, along with an ideal MTF of an FPA with 100% fill factor square detector elements and various vertical lines representing MTF estimation validity limits based off critical experiment details and (b) 1-D y-direction slices of estimated MTFs via the generalized method and the Fresnel approximation method, along with an ideal MTF of an FPA with 100% fill factor square detector elements and various vertical lines representing MTF estimation validity limits based off critical experiment details.

4.3.4.4 One-Factor Analysis of Variance (ANOVA) Random Model

A one-factor ANOVA model was developed to investigate the output PSD estimation variance. The Figure 66 diagram describes the PSD estimation process in detail. A matrix of the periodogram data used to estimate the output PSD is shown in Table 5, where I is the number of speckle images, J is the number of periodograms per speckle image and G_{IJ} is the J^{th} periodogram realization of the I^{th} image. All I periodograms per image are averaged, generating an image sample mean periodogram, $\hat{G}_{I\cdot}$. These image sample mean periodograms are then averaged together, generating $\hat{G}_{\cdot\cdot}$, a mean PSD estimate for the full speckle data set.

Table 5: Matrix of windowed periodogram data for a one-factor ANOVA analysis.

Speckle Image	Periodogram Observations	Averages
1	G_{11} G_{12} $\ldots$ G_{1J}	$\hat{G}_{1\cdot}$
2	G_{21} G_{22} $\ldots$ G_{2J}	$\hat{G}_{2\cdot}$
$\vdots$	$\vdots$ $\vdots$ $\ldots$ $\vdots$	$\vdots$
I	G_{I1} G_{I2} $\ldots$ G_{IJ}	$\hat{G}_{I\cdot}$
		$\hat{G}_{\cdot\cdot}$

The ANOVA approach validity requires three assumptions: (1) periodogram observation independence, (2) normally distributed periodogram observations, and (3) an equal standard deviation for all periodogram observations [86]. Reference [70] demonstrates the validity of these assumptions, which hold for the presented experimental scenario. Based on an ANOVA analysis, the confidence interval for the underlying true mean of the PSD can be found as,

$$LB = \hat{G}_{\cdot\cdot} - t(\frac{\alpha}{2})\frac{\sqrt{\sum_{i=0}^{I}(\hat{G}_{i\cdot} - \hat{G}_{\cdot\cdot})^2}}{\sqrt{I(I-1)}}, \tag{65}$$

$$UB = \hat{G}_{\cdot\cdot} + t(\frac{\alpha}{2})\frac{\sqrt{\sum_{i=0}^{I}(\hat{G}_{i\cdot} - \hat{G}_{\cdot\cdot})^2}}{\sqrt{I(I-1)}}, \tag{66}$$

where LB and UB are the lower and upper bounds for the output PSD estimation, and $t(\frac{\alpha}{2})$ is the student t-distribution for a $(1-\alpha)$ confidence level with $I-1$ degrees of freedom [87]. Assuming a confidence level of 0.95, the upper and lower bounds were computed for the generalized method's output PSD estimation. For the demonstrated scenario, the data set consisted of 16 independent speckle images and roughly 1000 periodograms where computed per image. The PSD bounds can be expressed as MTF bounds using the PSD-MTF relationship in Eq. (15). This ANOVA analysis generated generalized method MTF estimation confidence intervals with a maximum deviation of 1.7×10^{-3} from the estimated MTF within the estimation's valid spatial frequency range. This result indicates estimation variance had a negligible impact on the MTF estimation results; an adequate number of independent speckle realizations was utilized in the analysis. Differences between the MTF curves at valid spatial frequencies can be attributed to a variety of sources, including system noise and z-distance error. Differences between the x- and y-direction MTF estimations may be caused by the read-out electronics; these discrepancies are not investigated further in this research.

4.4 Regions of MTF Estimation Method Validity

A summary of the presented MTF estimation methods' validity regions is shown in Fig. 54. When possible, parameters are presented generically to allow for broader result application. In the figure, L is the aperture width, z is the propagation distance and x is the transverse distance. A 2-D figure of the $x-z$ plane is adequate to highlight the validity regions; a depiction of the $y-z$ plane would reveal identical results. Four regions are presented in the figure. Region 1 shows where the speckle irradiance ACFs in Eqs. (51) and (54) are invalid due to the delta-correlated assumption regarding the initial speckle field. The delta-correlated assumption analysis is detailed in Section 4.3.1. Region 2 denotes the angular limitations of scalar wave propagation, as investigated by [79, 80]. Determinations were made that with a NA of 0.4 (MHA of 24°, Eq. (55)), negligible differences were visible between the scalar and vector wave equations. Analysis of scenarios with an NA of 0.6 (MHA of 38°), differences on the order of 10% were experienced. Development and implementation of ACFs via vector field propagation methods are required for a more concrete understanding of this angular limitation. However, current understanding is adequate to realize region 2 is not a limiting factor for practical analysis of FPAs. None of the presented speckle-based MTF estimation methods are valid in regions 1 or 2.

Region 3 denotes the region of validity of both the generalized MTF estimation method and the impulse response estimation method introduced in Chapter V. Both of these methods are restricted solely by the limitations associated with regions 1 and 2. Finally, region 4 denotes the validity of the conventional speckle-based FPA MTF estimation approach [11, 76] demonstrated in Section 4.3.4. This limitation is due to the non-stationarity of the speckle field in nonparaxial scenarios. Implementation of the conventional approach requires a WSS speckle field in order for the input PSD to be valid. Although the analysis in Section 4.3.2 demonstrates that even in paraxial conditions, there is always some deviation in the speckle ACF, empirical analysis has demonstrated this error is negligible in an experimental context. Therefore, the conventional MTF estimation method utilizing Fresnel propagation is valid for $MHA \leq 10^\circ$. Note region 4 is included as a valid region for the estimation methodologies introduced in this research.

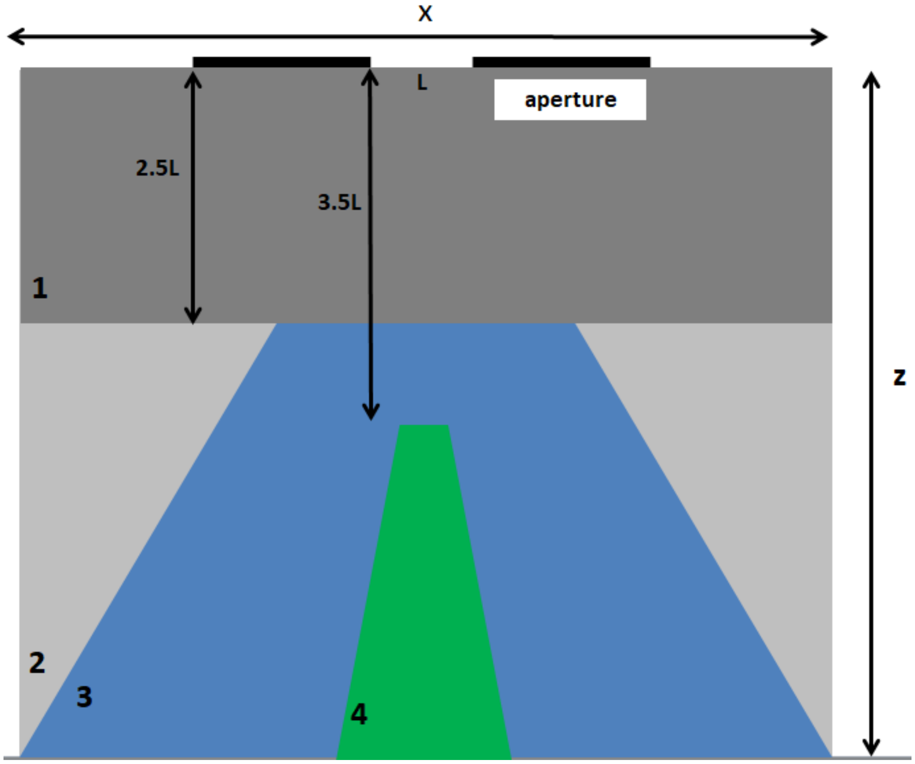

Figure 54: Depiction of validity regions for MTF estimation methodologies. The graphic represents an overview of the propagation scenario. The primary speckle propagation direction is z, through a aperture, L. The lateral direction, x, is also shown. Region 1 shows where the speckle irradiance autocorrelation functions Eqs. (51) and (54) are invalid due to the delta-correlated assumption regarding the initial speckle field. The angular limit beyond which scalar wave propagation is no longer accurate, as described by [79, 80], is shown as the boundary between Regions 2 and 3. The validity of both the generalized MTF estimation method and the impulse response estimation method, introduced in Chapter V, are demonstrated by Region 3. Region 4 shows the conventional speckle-based MTF estimation method limitations due to the validity of Fresnel electric field propagation.

4.5 Conclusion

This chapter addresses the challenge of estimating the MTF of FPAs using random laser speckle under conditions where the detector pitch and wavelength lead to test geometries where the Fresnel approximation is no longer valid. Advantages of developing the input PSD of speckle indirectly using numerical RS propagation to first compute the ACF are investigated. While the ACF is shown to be non-stationary, the error associated with making stationary assumptions and employing linear systems analysis is quantified for the first time and determined to be negligible relative to window bias error introduced through the previously established output PSD estimation process. An experimental application of the approach shows a 27% spatial frequency range increase relative to an estimation made assuming the closed-form solution of the input PSD based on the Fresnel assumption. Finally, a summary of the regions where the conventional and generalized MTF estimation techniques are theoretically valid is presented. These results demonstrate FPA MTF estimation can be extended to scenarios where paraxial approximations are invalid.

V. Iterative Maximum Likelihood Approach to Focal Plane Array Impulse Response Estimation Using Random Laser Speckle

This chapter introduces a novel methodology, alternative to Chapter IV's generalized method, for focal plane array (FPA) resolution estimation using random laser speckle in nonparaxial geometeries. The method introduced in Chapter V focuses on estimating the FPA's impulse response via use of the analytical and estimated laser speckle irradiance autocorrelation functions (ACFs). This chapter is based on an Society of Photo-Optical Instrumentation Engineers (SPIE) Defense and Commercial Sensing (DCS) proceedings paper which will be presented in April 2022. This effort outlines an iterative maximum likelihood function-based approach proposed for impulse response estimation, demonstrates the proposed technique's effectiveness via simulation and discusses the challenges associated with implementing the technique experimentally.

5.1 Introduction

Infrared (IR) FPAs are vital sub-components to military and civilian imaging systems. Increasingly challenging performance, size, weight and power (SWaP) requirements have spurred development of smaller pixel pitch devices [88]. It can be practically assumed in these small devices that lateral carrier diffusion challenges will increase [74] compared to larger pitch devices. Accurate and direct resolution performance analysis is vital for IR detectors, especially with regards to smaller devices.

Laser speckle-based MTF estimation techniques are well-established non-destructive methods for direct FPA resolution analysis that do not require the use of intervening optics [11, 12, 76]. Conventional technique implementation utilizes input power spectral densities (PSDs) reliant on Fresnel electric field propagation and its implied small angle approximations [32]. As the pixel pitch of FPAs decrease, the testbed diffracting aperture and FPA must be positioned at a distance equal to a few aperture lengths apart to generate sufficiently high spatial frequencies. Because of this, Fresnel propagation assumptions are violated due to the geometry which requires angles exceeding the paraxial limit. In addition, violation of the Fresnel assumption leads to non-wide sense stationary (WSS) random speckle impinging on the FPA, making the standard PSD methods utilizing the Wiener-Khintchine theorem [32] for directly evaluating the MTF invalid. Here, a novel approach is introduced where the FPA impulse response is estimated by exploiting the ACF input-output relationship of random processes to a linear system. This formulation does not require a WSS input process and the input ACF of the speckle irradiance is computed numerically using Rayleigh-Sommerfeld (RS) propagation, making it valid in geometries violating conventional Fresnel assumptions. An iterative maximum likelihood approach is presented for estimating the FPA impulse response based on the linear system relationship of the random speckle ACFs. The approach is then demonstrated in a realistic scenario using simulated random laser speckle

In the following sections, the maximum likelihood estimation (MLE) is formulated, beginning with a linear system development of the FPA assuming a random laser speckle input. An assumed estimation error resulting from estimating the output ACF from speckle images generated by the FPA allows the MLE for the FPA impulse response to be determined. Additional regularization terms are added to stabilize convergence and a conjugate gradient technique is implemented to iteratively solve for the impulse response. The impulse response estimation approach is demonstrated using data generated by simulating a large number of random laser speckle realizations impinging on a realistic, but notional FPA. Data is presented regarding the number of independent random speckle realizations required for convergence to an accurate impulse response. Finally, theoretical limitations and practical challenges are discussed.

5.2 Methodology

5.2.1 Development of a maximum likelihood estimator for the impulse response function

The standard linear systems approach for random speckle-based MTF FPA measurement leverages the Wiener-Khintchine theorem, which allows the problem to be framed in terms of a simple input-output PSD relationship for linear systems. For scenarios where the measurement dictates geometries that violate the Fresnel approximation, the random speckle cannot be considered WSS and the PSD approach is no longer valid. In nonparaxial geometries, an approach to evaluate the MTF indirectly can be derived alternatively by first estimating the impulse response of the FPA using the input-output ACF relationship for linear systems. The ACF relationship is not restricted by WSS requirements. Additionally, RS propagation can be utilized rather than Fresnel propagation to obtain a valid solution. Maximum likelihood estimation provides a suitable iterative approach for estimating the impulse response based on a large number of random speckle observations.

This methodology begins with a standard linear system convolution relationship [89],

$$Y[m,n] = h[m,n] * * X[m,n] + \eta[m,n], \tag{67}$$

where the random process, X, is input into a linear system, h. The resulting linear system output is Y, the noise term associated with the linear system is η, $[m,n]$ is a spatial coordinate pair and $**$ represents a two dimensional convolution. Development of this approach is completed in the discrete domain, as FPA imagery is discrete.

Additionally, the resulting negative log-likelihood estimator will be minimized via an iterative estimation process, which is better suited for the discrete domain. Development of this estimator in the continuous domain is straightforward, but not as applicable to this solution process. Rewriting this convolution in summation form,

$$\begin{aligned} Y[m_1, n_1] &= \sum_{i=0}^{N-1}\sum_{j=0}^{N-1} h[i,j]X[m_1 - i, n_1 - j] + \eta[m_1, n_1], \\ Y[m_2, n_2] &= \sum_{p=0}^{N-1}\sum_{q=0}^{N-1} h[p,q]X[m_2 - p, n_2 - q] + \eta[m_2, n_2], \end{aligned} \tag{68}$$

where the linear system outputs, Y, are annotated at specific coordinate pairs, $[m_1, n_1]$ and $[m_2, n_2]$. The ACF of the output Y, R_{YY}, is given in terms of an expected value, where $E[.]$ is the expected value operator. Expanding the expected value,

$$\begin{aligned} R_{YY}[m_1, n_1; m_2, n_2] &:= E[Y[m_1, n_1]Y[m_2, n_2]], \\ R_{YY}[m_1, n_1; m_2, n_2] &= E[(\sum_{i=0}^{N-1}\sum_{j=0}^{N-1} h[i,j]X[m_1 - i, n_1 - j] + \eta[m_1, n_1]) \\ &\quad (\sum_{p=0}^{N-1}\sum_{q=0}^{N-1} h[p,q]X[m_2 - p, n_2 - q] + \eta[m_2, n_2])], \end{aligned} \tag{69}$$

and simplifying by applying the ACF definition to the random process inputs results in the following linear system association,

$$\begin{aligned} R_{YY}[m_1, n_1; m_2, n_2] = \sum_{i=0}^{N-1}\sum_{j=0}^{N-1}\sum_{p=0}^{N-1}\sum_{q=0}^{N-1} h[i,j]h[p,q]R_{XX}[m_1 - i, n_1 - j; m_2 - p, n_2 - q] \\ + R\eta\eta[m_1, n_1; m_2, n_2]. \end{aligned} \tag{70}$$

This is the fundamental ACF input-output relationship for linear systems with a random input and does not require the random process to be WSS. The complete model describing the linear system for the output ACF is given in Eq. (71). An estimation error, v, associated with estimating the R_{YY} from the system output Y as an additive noise term is included,

$$R_{YY}[m_1, n_1; m_2, n_2] = \sum_{i=0}^{N-1}\sum_{j=0}^{N-1}\sum_{p=0}^{N-1}\sum_{q=0}^{N-1} h[i,j]h[p,q]R_{XX}[m_1{-}i, n_1{-}j; m_2{-}p, n_2{-}q]+$$

$$R\eta\eta[m_1, n_1; m_2, n_2] + v[m_1, n_1; m_2, n_2]. \quad (71)$$

The estimation error, v, is a zero mean, normally distributed error associated with estimating R_{YY}, described by $N(0, \sigma_v^2)$, where the random variable at each location is independent and identically distributed. The joint probability density function (pdf) of v can be written as,

$$f_v(\mathbf{v}) = \frac{1}{(2\pi)^{\frac{M^4}{2}}\sigma_v^{M^4}} exp\left[\frac{-1}{2\sigma_v^2}\sum_{m_1=0}^{M-1}\sum_{n_1=0}^{M-1}\sum_{m_2=0}^{M-1}\sum_{n_2=0}^{M-1} v[m_1, n_1; m_2, n_2]^2\right], \quad (72)$$

where $\mathbf{v}$ represents the vector notation. M is the length of the observation region of interest (ROI). The likelihood function of R_{YY}, L, with respect to the unknown, but deterministic parameter $\mathbf{h}$ can be found by computing the conditional joint pdf of R_{YY} using a transformation of random variables such that,

$$L(R_{YY}; \mathbf{h}) = f_{R_{YY}}(R_{YY}|\mathbf{h}) = f_v(\mathbf{v} = T), \quad (73)$$

where $\mathbf{h}$ represents vector notation and T is defined as,

$$T[m_1,n_1;m_2,n_2] = (R_{YY}[m_1,n_1;m_2,n_2] - \sum_{i=0}^{N-1}\sum_{j=0}^{N-1}\sum_{p=0}^{N-1}\sum_{q=0}^{N-1} h[i,j]h[p,q]R_{XX}[m_1-i,n_1-j;m_2-p,n_2-q] + R_{\eta\eta}[m_1,n_1;m_2,n_2])^2. \tag{74}$$

Using Eq. (73), the likelihood function can now be written as,

$$L(R_{YY};\mathbf{h}) = \frac{1}{(2\pi)^{\frac{N^4}{2}}\sigma_v^{N^4}} exp\left[\frac{-1}{2\sigma_v^2}\sum_{m_1=0}^{M-1}\sum_{n_1=0}^{M-1}\sum_{m_2=0}^{M-1}\sum_{n_2=0}^{M-1} T[m_1,n_1;m_2,n_2]\right]. \tag{75}$$

Taking the log of the impulse response pdf, removing the constant terms and negative sign produces a negative log-likelihood function for impulse response estimation,

$$L_L(R_{YY};\mathbf{h}) = \frac{1}{2\sigma_v^2}\sum_{m_1=0}^{M-1}\sum_{n_1=0}^{M-1}\sum_{m_2=0}^{M-1}\sum_{n_2=0}^{M-1}(R_{YY}[m_1,n_1;m_2,n_2] - \sum_{i=0}^{N-1}\sum_{j=0}^{N-1}\sum_{p=0}^{N-1}\sum_{q=0}^{N-1} h[i,j]h[p,q]R_{XX}[m_1-i,n_1-j;m_2-p,n_2-q] + R_{\eta\eta}[m_1,n_1;m_2,n_2])^2. \tag{76}$$

The maximum likelihood estimator of **h** is the value of **h** that maximizes the log-likelihood function or minimizes the negative log-likelihood function in Eq. (76), which indicates the impulse response that achieves a minimum error in the linear system model in Eq. (71). However, direct minimization of Eq. (76) can lead to excessive noise due to conventional challenges involved with solving inverse problems.

To mitigate these issues, a ridge regression regularization operator is added to the negative log-likelihood function, enforcing a smooth impulse response estimate. The updated negative log-likelihood function is,

$$L_T(R_{YY};\mathbf{h}) = \frac{1}{2\sigma_v^2}\sum_{m_1=0}^{M-1}\sum_{n_1=0}^{M-1}\sum_{m_2=0}^{M-1}\sum_{n_2=0}^{M-1}(R_{YY}[m_1,n_1;m_2,n_2]-$$
$$\sum_{i=0}^{N-1}\sum_{j=0}^{N-1}\sum_{p=0}^{N-1}\sum_{q=0}^{N-1} h[i,j]h[p,q]R_{XX}[m_1-i,n_1-j;m_2-p,n_2-q]+R_{\eta\eta}[m_1,n_1;m_2,n_2])^2$$
$$+\frac{1}{2\gamma}||\mathbf{h}||_2^2, \quad (77)$$

where $||.||_2$ is the L_2 norm and γ scales the regularization term's contribution. A Laplacian regularization kernel [90] was considered, but due to the impulse response's finite support, edge smearing and ringing effects were experienced. The weight of the regularization term, γ, needs to be on the order of the effective linear weighting term, σ_v^2, to counter the relative size difference between the ACFs (45×45) and the impulse response (9×9) [91]. Table 6 describes the linear systems parameters corresponding to an FPA impulse response measurement.

Given the log-likelihood function is quadratic; an iterative gradient descent approach is used to minimize the negative log-likelihood function to estimate the impulse response. In order to determine the gradients, the coordinate pair (m_1, n_2) is first fixed to constant values (c_1, c_2). Without a WSS assumption, the ACF is spatially shift variant and the functional form of the ACF can vary as a function of position, as it depends on two coordinate pairs. By fixing one coordinate pair, the location of the center ACF is fixed, which allows the negative log-likelihood function to be evaluated at one position at a time,

Table 6: Linear systems parameters corresponding to an FPA impulse response measurement.

Parameter	Physical Descr.	Mathematical Descr.
h	FPA impulse response	unknown, deterministic
N, M	length of observation ROI	deterministic
X	speckle irradiance data input onto FPA	random process
R_{XX}	ACF of speckle irradiance input	deterministic
Y	speckle irradiance data output	random process
R_{YY}	ACF of speckle irradiance output	random
ν	R_{YY} estimation error	random, $N(0, \sigma_\nu^2)$
η	FPA system noise	random, $N(0, \sigma_\eta^2)$
$R_{\eta\eta}$	ACF of FPA system noise	deterministic

$$L_T(R_{YY}; \mathbf{h}) = \frac{1}{2\sigma_v^2} \sum_{m_2=0}^{M-1} \sum_{n_2=0}^{M-1} (R_{YY}[c_1, c_2; m_2, n_2] -$$
$$\sum_{i=0}^{N-1} \sum_{j=0}^{N-1} \sum_{p=0}^{N-1} \sum_{q=0}^{N-1} h[i,j]h[p,q]R_{XX}[c_1 - i, c_2 - j; m_2 - p, n_2 - q] + R_{\eta\eta}[c_1, c_2; m_2, n_2])^2$$
$$+ \frac{1}{2\gamma} ||h[i,j]||_2^2. \tag{78}$$

Next, in order to make the problem more tractable, the impulse response is assumed to be separable. Since typical FPA MTF measurements are evaluated in orthogonal directions aligned with the detector axes, this is a reasonable assumption. Further efforts could investigate removing this assumption. Imposing the separability constraint, the gradient of the negative log-likelihood function is calculated with respect to **h** separately for each location in the x-direction and y-direction of the impulse response,

$$
\begin{aligned}
g_k(\mathbf{h}_x) = \frac{\partial L_T(R_{YY};\mathbf{h})}{\partial h_x[k]} &= \frac{-1}{\sigma_v^2} \sum_{m_2=0}^{M-1} \sum_{n_2=0}^{M-1} \\
&\Big(\sum_{j=0}^{N-1} \sum_{p=0}^{N-1} \sum_{q=0}^{N-1} h_y[j] h_x[p] h_y[q] R_{XX}[c_1-k, c_2-j; m_2-p, n_2-q] + \\
&\sum_{i=0}^{N-1} \sum_{j=0}^{N-1} \sum_{q=0}^{N-1} h_x[i] h_y[j] h_y[q] R_{XX}[c_1-i, c_2-j; m_2-k, n_2-q]\Big) \\
\Big(R_{YY}[c_1,c_2;m_2,n_2] - &\sum_{i=0}^{N-1} \sum_{j=0}^{N-1} \sum_{p=0}^{N-1} \sum_{q=0}^{N-1} h_x[i] h_y[j] h_x[p] h_y[q] R_{XX}[c_1-i, c_2-j; m_2-p, n_2-q] \\
&+ R_{\eta\eta}[c_1,c_2;m_2,n_2]\Big) + \frac{1}{\gamma} \sum_{i=0}^{N-1} \sum_{j=0}^{N-1} h_x[i] h_y[j]^2, \quad (79)
\end{aligned}
$$

$$
\begin{aligned}
g_k(\mathbf{h}_y) = \frac{\partial L_T(R_{YY};\mathbf{h})}{\partial h_y[k]} &= \frac{-1}{\sigma_v^2} \sum_{m_2=0}^{M-1} \sum_{n_2=0}^{M-1} \\
&\Big(\sum_{i=0}^{N-1} \sum_{p=0}^{N-1} \sum_{q=0}^{N-1} h_x[i] h_x[p] h_y[q] R_{XX}[c_1-i, c_2-k; m_2-p, n_2-q] + \\
&\sum_{i=0}^{N-1} \sum_{j=0}^{N-1} \sum_{p=0}^{N-1} h_x[i] h_y[j] h_x[p] R_{XX}[c_1-i, c_2-j; m_2-p, n_2-k]\Big) \\
\Big(R_{YY}[c_1,c_2;m_2,n_2] - &\sum_{i=0}^{N-1} \sum_{j=0}^{N-1} \sum_{p=0}^{N-1} \sum_{q=0}^{N-1} h_x[i] h_y[j] h_x[p] h_y[q] R_{XX}[c_1-i, c_2-j; m_2-p, n_2-q] \\
&+ R_{\eta\eta}[c_1,c_2;m_2,n_2]\Big) + \frac{1}{\gamma} \sum_{i=0}^{N-1} \sum_{j=0}^{N-1} h_y[j] h_x[i]^2. \quad (80)
\end{aligned}
$$

5.2.2 Rayleigh-Sommerfeld speckle autocorrelation function development

The speckle irradiance ACF input to the FPA is derived via a scalar wave-based development of the free space propagation geometry under analysis. The scenario of interest is shown in Fig. 19, where a diffracting aperture is located in the (α, β) plane and the speckle field is propagated to the (x, y), or observation plane. The analytical observation plane speckle field correlation function was developed in Section 2.3 and the speckle irradiance correlation function is described in Section 4.2.1. Discrete implementation and computation of Eq. (51) produces R_{XX} for use in impulse response estimation process outlined in Section 5.2.1.

5.2.3 Conjugate Gradient Algorithm

The process of determining the impulse response through MLE involves first estimating R_{YY} located at the coordinates (c_1, c_2) from the image data acquired by the FPA using a large number of speckle sample function realizations. In theory, more sample functions could be obtained by varying the observation location of R_{YY}, (c_1, c_2), throughout the FPA ROI. However, the small variation observed in R_{YY} throughout the observation plane in typical measurement geometries was insufficient to generate independent observations and led to a poor, inaccurate estimate of R_{YY}. The variation in R_{YY} produced by using many speckle sample functions was sufficient to generate a likelihood function having enough curvature to allow a maximum solution through an iterative gradient descent approach. Once an estimate of R_{YY} is computed, a conjugate gradient algorithm can be implemented to iteratively determine the impulse response.

A block diagram of the implemented conjugate gradient algorithm is shown in Fig. 55. The first step is parameter initialization, which includes making an initial informed guess for the impulse response, h_o, and an initial step size estimation, α_o. The relative magnitudes of the estimation error variance associated with R_{YY} and regularization term weighting factor are adjusted to provide reasonable estimated impulse response convergence. Choosing an appropriate initial impulse response nar-

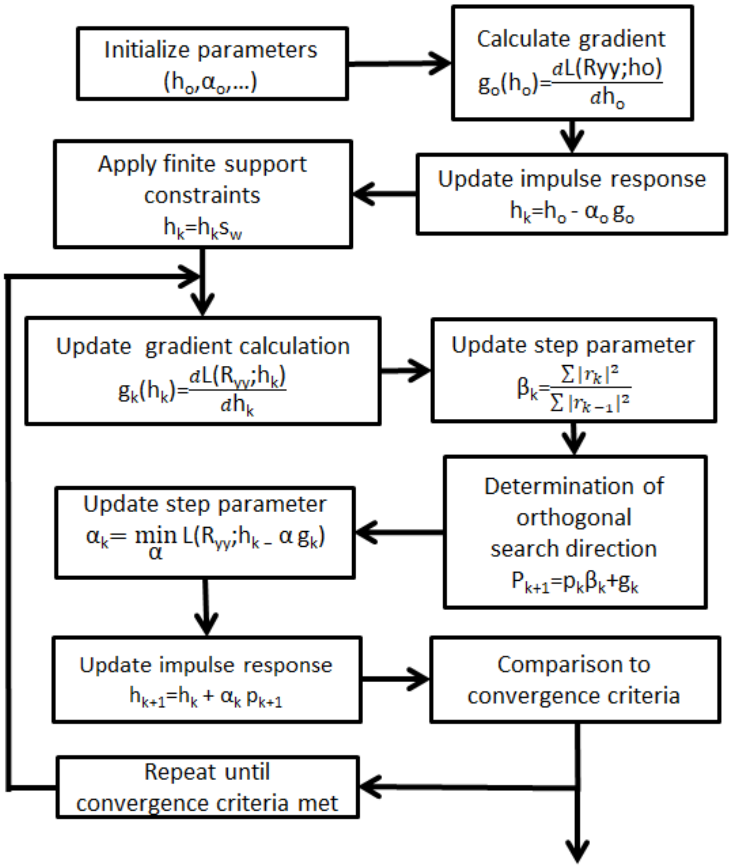

Figure 55: Block diagram describing conjugate gradient algorithm used to estimate focal plane array impulse response.

rows the iterative optimizer solution space. Next, the gradient, g_o, of the negative log-likelihood function is computed and an impulse response estimate, h_k, is made. Then, an appropriate support constraint mask, s_w, is applied to the impulse response estimate. After these initial steps, the iterative portion of the optimizer commences, beginning with a computation of the negative log-likelihood function's gradient, g_k, using the latest impulse response estimate. Then, the step size, β_k, is updated via the Polak-Ribiere method [92], where r_k is the negative gradient of the k^{th} log-likelihood function iteration. A new orthogonal search direction, p_{k+1}, is then determined using the previous search direction, the latest step size and computed gradient. Next, the step parameter, a_k, is selected via a line search effort based on the minimization of the negative log-likelihood function. Then, another impulse response estimate is made and the resulting estimate parameters are compared to the established convergence criteria. The convergence criteria includes: number of iterations, gradient tolerance, step size tolerance and likelihood function tolerance. The algorithm continues to iterate until one of the convergence criteria is met.

5.3 Results

5.3.1 Speckle Simulation

Simulation of speckle irradiance generation, propagation, and collection by a focal plane was accomplished by using the idealized linear systems approach [65] described in Section 3.2.1. When the process outlined in Fig. 20 is applied to the delta-correlated input speckle, the outcome is the generation of laser speckle image realizations, Y, with the appropriate statistics for the simulated speckle testbed. In this particular scenario, the free space propagation transfer function development involved calculating a PSD for the speckle irradiance impinging on the FPA. The PSD is computed via exploiting the Fourier transform relationship between the spatially averaged ACF and PSD. The spatially averaged ACF is computed via numerical evaluation of Eq. (51) centered at multiple coordinate locations distributed within the observation region of interest (ROI). These ACFs were then averaged, resulting in the spatially averaged ACF for the ROI. This spatially averaged ACF was Fourier transformed, generating the appropriate PSD of interest for the given test geometery. With this PSD, the appropriate propagation transfer function is developed. When this transfer function is applied to the simulation's ideal random speckle input, speckle irradiance data, X, is generated with the proper PSD at the aperture. Note that the speckle irradiance at the FPA will be WSS when generated using this method. This technique allows for a more streamlined approach than applying computationally complex field propagation integrals to generate non-WSS speckle. The PSD of the speckle data generated from this approach is representative of non-WSS random speckle, but the actual speckle irradiance is not. However, the input-output PSD relationship utilizing a modeled FPA MTF, or impulse response, is used to generate R_{YY} for the simulation, which is not strictly valid. Despite these limitations, the simulation does demonstrate the various requirements and challenges for estimating the FPA impulse response using ACF-based methods.

The numerical evaluation of Eq. (51) was performed on the Air Force Research Laboratory's High Performance Computer system. Simulation propagation geometry was chosen to mirror the testbed geometry detailed in Appendix A. A 32.3mm propagation aperture (L) was simulated. The wavelength, λ, was set to 9.45μm to match an available quantum cascade laser (QCL). The chosen propagation distance was $82mm$. An on-axis ACF was computed. The aperture and observation planes were sampled on sub-λ grid to maximize ACF resolution. A conservative testbed simulation SNR of 90 was chosen using the process outlined in Section 3.6.1. The typical run time for generation of a singular ACF was approximately three hours.

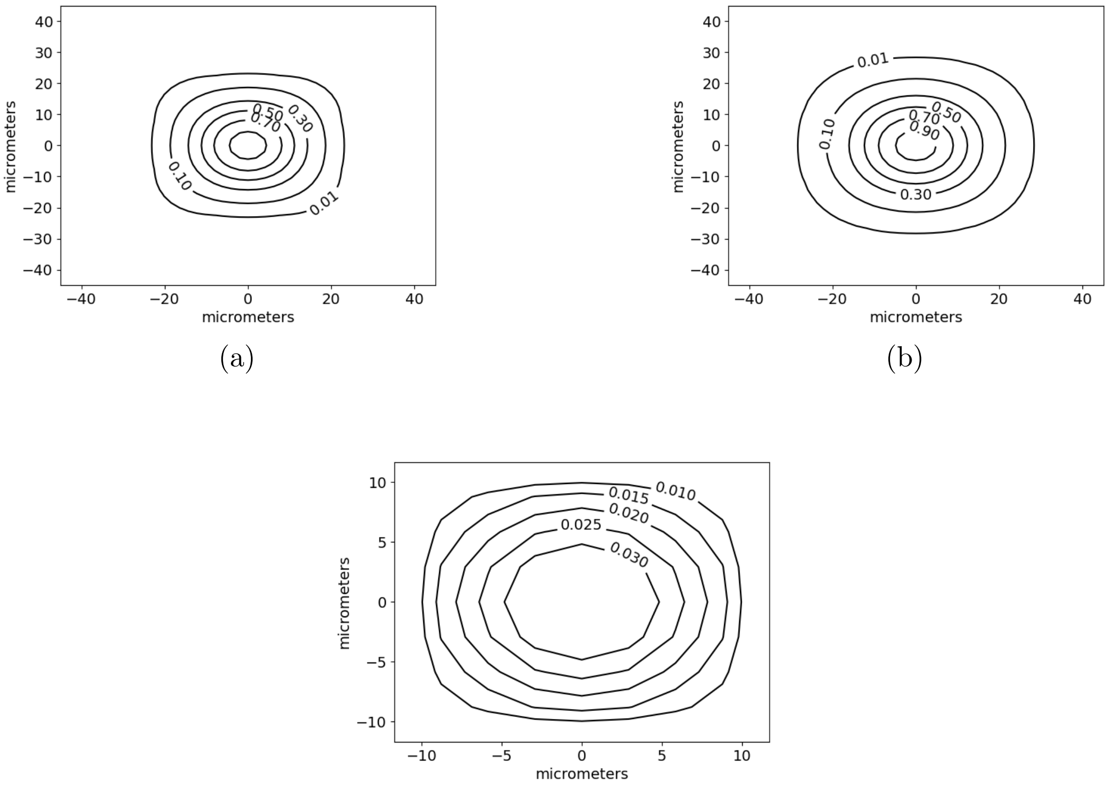

(a) (b)

(c)

Figure 56: Notable autocorrelation function and impulse response functions related to the laser speckle simulation. (a) 2-D spatially-averaged autocorrelation function of speckle irradiance input into focal plane array, (b) 2-D autocorrelation function of speckle imagery post-focal plane array (c) 2-D focal plane array impulse response.

Figs. 56(a)-(c) are contour plots of the analytical ACFs and modeled impulse response from the speckle simulation. Fig. 56(a) demonstrates the spatially averaged ACF of the laser speckle impinging on the FPA surface. R_{YY} in Fig. 56(b) is the analytical convolution between the impulse response in Fig. 56(c) and the ACF in Fig. 56(a) as demonstrated in Ref. 93. The representative FPA impulse response is shown in Fig. 56(c). This modeled impulse response adheres to established optical impulse response criteria: its elements sum to 1; it is a monotonically decreasing function; and it contains only non-negative components. Future analytical and simulation results will be presented in 1-D for ease of understanding.

5.3.2 Number of Speckle Realizations

The goal of this analysis is to determine the number of independent speckle realizations required to accurate estimate the impulse response of the simulated FPA under test. R_{YY} accuracy is critical to impulse response estimation. Increasing the independent speckle realizations directly leads to increased R_{YY} accuracy. There are challenges with generating independent speckle realizations as outlined in Chapter III Ref. 65 and described in further detail in Section 5.4. For comparison, three sets of speckle realizations containing 10000, 5000 and 1000 images were generated; the associated ACFs were estimated from the image sets. In this section, R_{YY} estimations were generated to match computed R_{XX} sampling, simulating the effect of applying microscan super-resolution techniques and negating any interpolation impacts on R_{YY} estimation accuracy. Figs. 57(a)-(c) demonstrate the comparison between the analytical R_{YY} in Fig. 56(b) and the estimated R_{YY} using the simulated images. The calculated MSE between the analytical and estimated ACFs is shown in each figure. The figures demonstrate that increased independent speckle image realizations lead to increased ACF estimation accuracy.

5.3.2.1 Conjugate gradient implementation: 10000 realizations

To explore the effect of R_{YY} accuracy on impulse response estimation accuracy, the estimated ACFs, along with the corresponding analytical R_{XX}, were input into the conjugate gradient MLE process outlined in Section 5.2.3. The results of the model impulse response estimation using the R_{YY} generated with 10000 independent speckle realizations are shown in Figs. 58(a)-(c). For this scenario, $\gamma = 3\sigma_{\nu}^2$ due to the relatively low estimation error between the analytical and estimated R_{YY}. A 1-D plot of the estimated impulse response, the actual modeled system impulse response and the initial impulse response estimate for the analysis, are shown in Fig. 58(a).

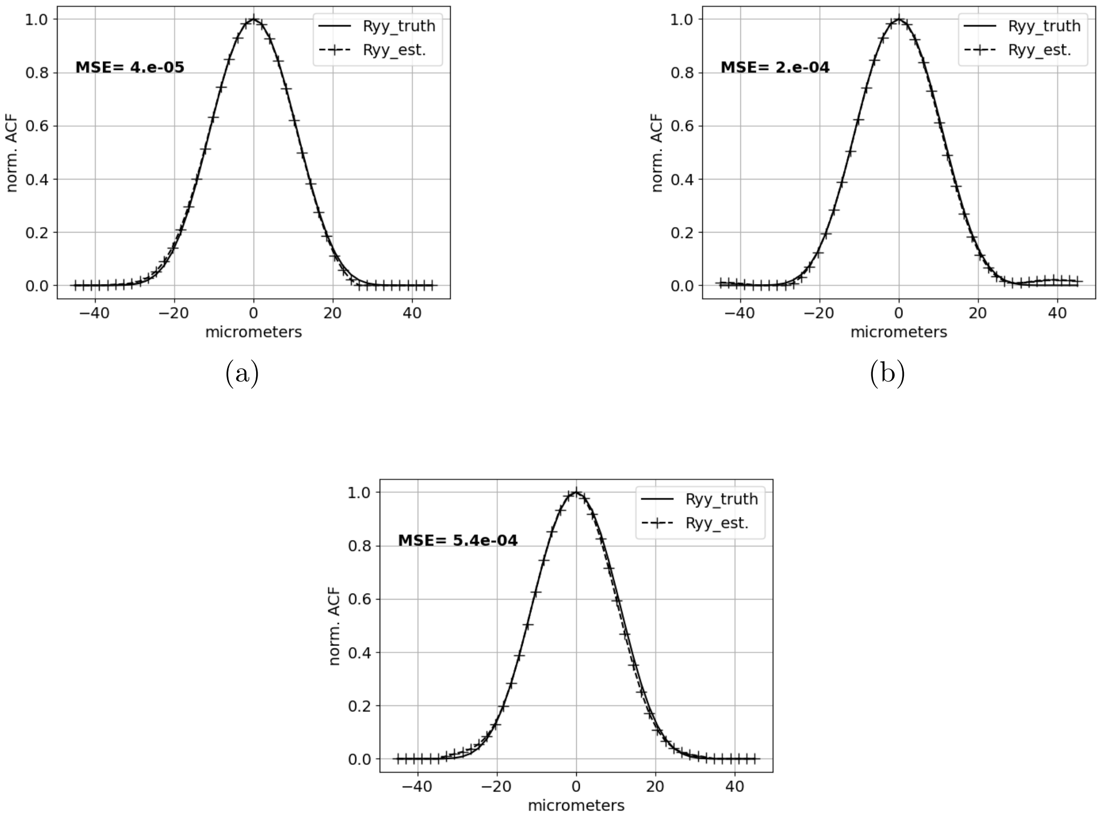

(a) (b)

(c)

Figure 57: One-dimensional R_{YY} ACF estimation and analytical comparison using (a) 10000 independent speckle image realizations, (b) 5000 independent speckle image realizations, (c) 1000 independent speckle image realizations. The R_{YY} accuracy increases as the number of realizations increase.

For this scenario, an established convergence criterion was met after 192 iterations. Fig. 58(b) demonstrates the negative log-likelihood function value at each algorithm iteration. The general trend is the negative log-likelihood function decreases with each iteration, as expected. Initial inspection of the negative log-likelihood function plot may lead to a convergence criteria tolerance reduction recommendation due to diminishing negative log-likelihood function returns. Despite the relatively minimum negative log-likelihood function reduction after the 175^{th} iteration, the impulse response mean square error (MSE), shown in Figure 58(c), continues to decline significantly until roughly iteration 190, demonstrating the importance of continuing the

MLE iterations.

Since FPA resolution analysis is conventionally performed in the spatial frequency domain via analysis of MTF curves, these impulse response estimates are Fourier-transformed to their spatial frequency counterparts for further comparison. Fig. 58(d) shows the derived MTF error between the truth MTF and the estimated MTF after the final algorithm iteration. Ref. 70 established a criterion for acceptable MTF estimation, 2% or less error between the true MTF and estimated MTF on a per spatial frequency basis, which was utilized as a threshold for this analysis. In Fig. 58(d), the MTF error reaches its maximum of 1.2% at the FPA Nyquist sampling frequency, showing excellent impulse response estimation, and therefore MTF estimation, with 10000 independent speckle image realizations.

5.3.2.2 Conjugate gradient implementation: 5000 realizations

The number of required speckle realizations analysis was continued using an R_{YY} estimation generated from 5000 speckle images. The results are shown in Figs. 59(a)-(c). For this scenario, $\gamma = \sigma_\nu^2$ due to the increased relative estimation error between the analytical and estimated R_{YY} compared to the previous analysis. A 1-D plot of the final estimated impulse response, the actual modeled system impulse response and the initial impulse response estimation are shown in Fig. 59(a). In this analysis, an established convergence criterion was met after 95 iterations. Fig. 59(b) shows the negative log-likelihood function value at each algorithm iteration. The MSE between the truth impulse response and the final iteration impulse response estimation is shown in Fig. 59(c); an MSE of 8×10^{-6} occurs at the 95^{th} iteration. Fig. 59(d) shows the derived MTF error between the truth MTF and the estimated MTF after the final iteration. The MTF error reaches its maximum of 1.25% at 0.9 of the FPA Nyquist sampling frequency, showing good agreement between MTF estimation and

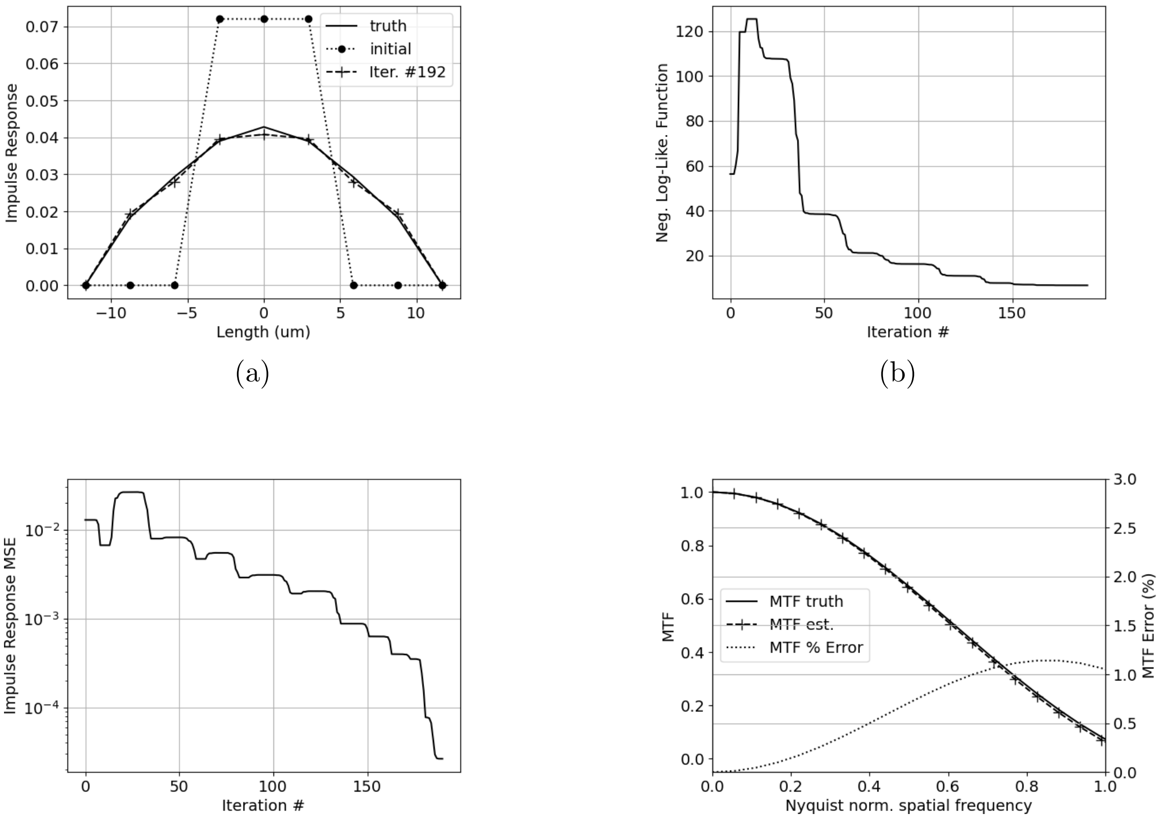

(a) (b)

(c) (d)

Figure 58: Iterative maximum likelihood estimation results with R_{YY} estimations generated with 10000 independent speckle image realizations, (a) truth, initial and final estimated focal plane array impulse responses (b) negative log-likelihood function calculations, (c) impulse response mean square error and (d) modulation transfer function estimation and relative percentage error. Convergence to a impulse response estimation with an associated modulation transfer function error that meets the established 2% accuracy threshold was achieved after 192 iterations.

truth when using 5000 independent speckle image realizations.

5.3.2.3 Conjugate gradient implementation: 1000 realizations

The number of required realizations analysis was continued using the R_{YY} estimation generated from 1000 independent speckle images. The results are shown in Figs. 60(a)-(c). For this scenario, $\gamma = \sigma_\nu^2/4$, increasing the regularization term weight due to the increased estimation error between the analytical and estimated R_{YY} com-

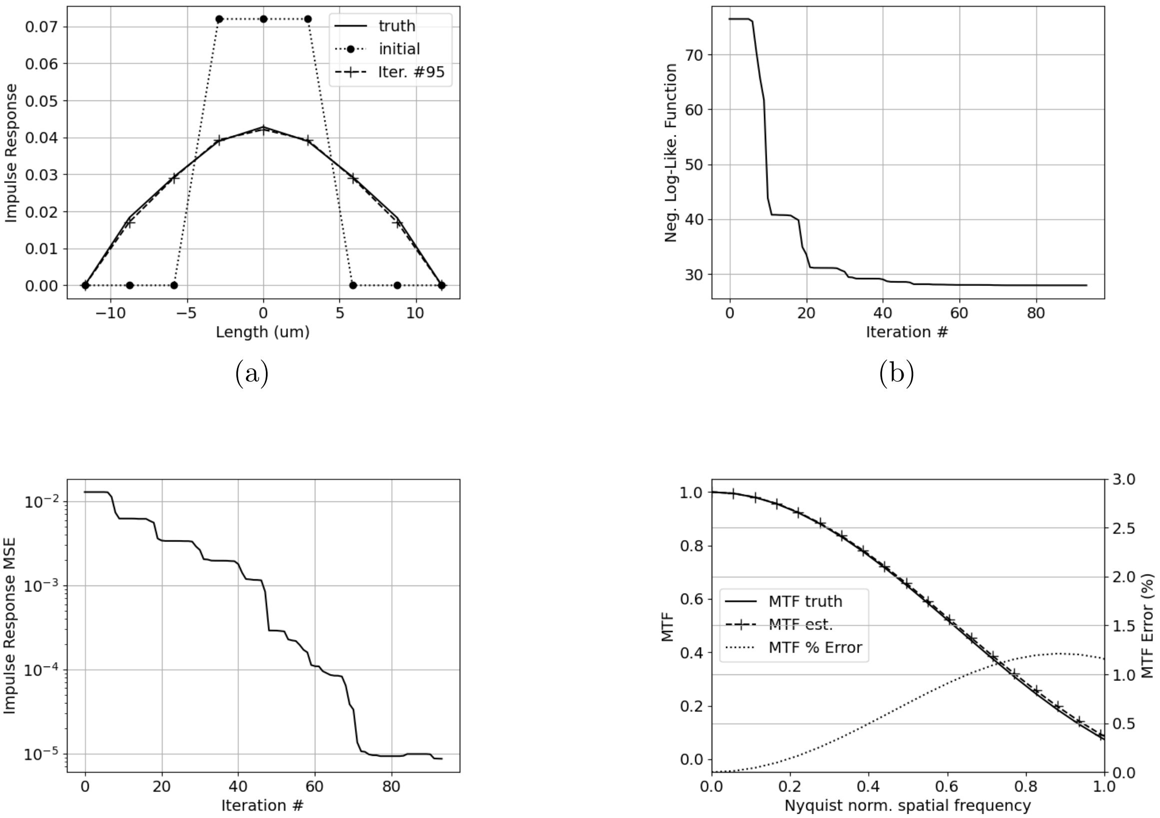

(a) (b)

(c) (d)

Figure 59: Iterative maximum likelihood estimation results with R_{YY} estimations generated with 5000 independent speckle image realizations, (a) truth, initial and final estimated focal plane array impulse responses (b) negative log-likelihood function calculations, (c) impulse response mean square error and (d) modulation transfer function estimation and relative percentage error. Convergence to a impulse response estimation with an associated modulation transfer function error that meets the established 2% accuracy threshold was achieved after 95 iterations.

pared to the previous analysis. A 1-D plot of the final impulse response estimation, the analytical impulse response and the initial impulse response estimation are shown in Fig. 60(a). The implemented scenario converges after 55 iterations. The increased regularization weight caused a convergence to be met at a lower iteration number than in the previous analysis. Estimation attempts were made with lower regularization weights, but these efforts resulted in impulse response estimations with significantly greater error.

The negative log-likelihood function value at each iteration is shown in Fig. 60(b). The negative log-likelihood function decreases as the number of iterations increases, as experienced in the previous analysis. The MSE between the truth impulse response and the current iteration impulse response is shown in Fig. 60(c); an MSE of 2×10^{-4} occurs at the 55^{th} iteration. Fig. 60(d) shows the derived MTF error between the truth MTF and the estimated MTF after the final iteration. The MTF error reaches its maximum of 11% at 0.9 of the FPA Nyquist sampling frequency, showing the 2% MTF error threshold is violated over a majority of the estimated MTF curve. This analysis demonstrates that 1000 independent speckle realizations are not adequate to accurately estimate the system under test's MTF based off of previously established success criterion.

5.3.3 R_{YY} Spatial Sampling

A critical aspect of the impulse response estimation approach is related to the spatial sampling of the R_{YY} estimate. If R_{YY} is not properly sampled, aliasing will occur and estimation of the impulse response will not be possible. Fig. 56(b) demonstrates the width of the analytical R_{YY} function from the speckle simulation, which is roughly 60 microns wide. The FPA samples the propagated speckle irradiance via finite width detector elements, which impacts the spatial sampling at which R_{YY} may be estimated. R_{XX} is computed analytically; its spatial sampling can be arbitrarily chosen to prevent aliasing and is not limited by the FPA detector sampling. Since R_{YY} will be aliased, microscan super-resolution techniques [94] can be implemented to match or exceed the spatial sampling of R_{XX} in order to allow the likelihood estimator of the impulse response to produce a valid solution. The impact of aliasing can be demonstrated by simulating microscan super-resolution and comparing those results with upsampling via interpolation. Interpolation will induce additional R_{YY}

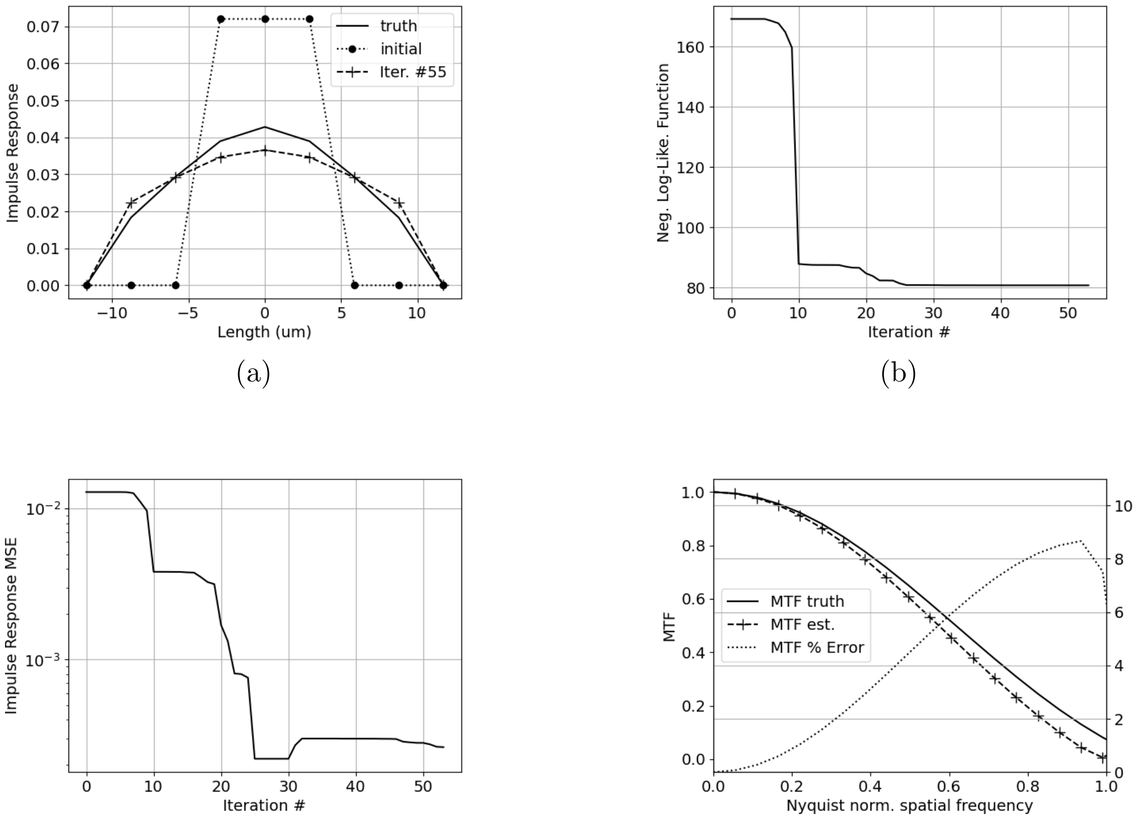

(a) (b)

(c) (d)

Figure 60: Iterative maximum likelihood estimation results with R_{YY} estimations generated with 1000 independent speckle image realizations, (a) truth, initial and final estimated focal plane array impulse responses (b) negative log-likelihood function calculations, (c) impulse response mean square error and (d) modulation transfer function estimation and relative percentage error. Due to estimation error associated with R_{YY}, the impulse response estimation, specifically the associated modulation transfer function error does not meet the established 2% accuracy threshold.

error to the estimation error discussed in Section 5.3.2.

To explore the impact R_{YY} sampling has on impulse response estimation, three analysis scenarios were considered. For each scenario, 5000 independent speckle realizations were utilized in the impulse response estimation process, as this number was demonstrated as sufficient to accurately estimate the model impulse response in Section 5.3.2.2. Then R_{YY} estimations were generated assuming 6× microscanning of the FPA under test (R_{YY} sampling will match computed R_{XX} sampling, so no interpolation is required), 2× microscanning and no microscanning. R_{YY} estimations for the 2× and no microscanning cases were upsampled to match the input R_{XX} sampling. The resulting R_{YY} estimations and their comparisons to the analytical R_{YY} are demonstrated in Figs. 61(a)-(c). There does not appear to be a visible MSE difference between the 6× and 2× cases; closer inspection of the actual data reveals a negligible difference. A minor R_{YY} estimation difference is visible between the 2× and 1× cases, specifically at the ACF edges. The impulse response estimation results for the 6× microscanning scenario were previously demonstrated as part of the Section 5.3.2.2 study; this analysis demonstrated excellent impulse response and MTF estimation accuracy.

5.3.3.1 R_{YY} 2× Sampling Rate Increase

The analysis continues with the application of the 2× microscan R_{YY} estimate to the analysis approach. The impulse response estimation results via application of this R_{YY} estimate are shown in Figs. 62(a)-(c). A regularization weight of $\gamma = \sigma_{\nu}^{2}$ was chosen for this scenario. A 1-D plot of the final estimated impulse response, the analytical system impulse response and the initial impulse response estimate are shown in Fig. 62(a). An established convergence criterion was met after 93 iterations for this scenario. Fig. 62(b) demonstrates the negative log-likelihood function value at each iteration of the iterative impulse response estimation process. As expected, the negative log-likelihood function decreases with each iteration. The MSE between the truth impulse response and the current iteration impulse response is shown in Fig. 62(c); an MSE of 9.5×10^{-6} occurs at the 93^{th} iteration. Fig. 62(d) shows the derived MTF error between the truth MTF and the estimated MTF after the final iteration. The MTF error reaches its maximum of 1% at FPA Nyquist sampling frequency, showing the 2% MTF error threshold is met throughout the entire MTF

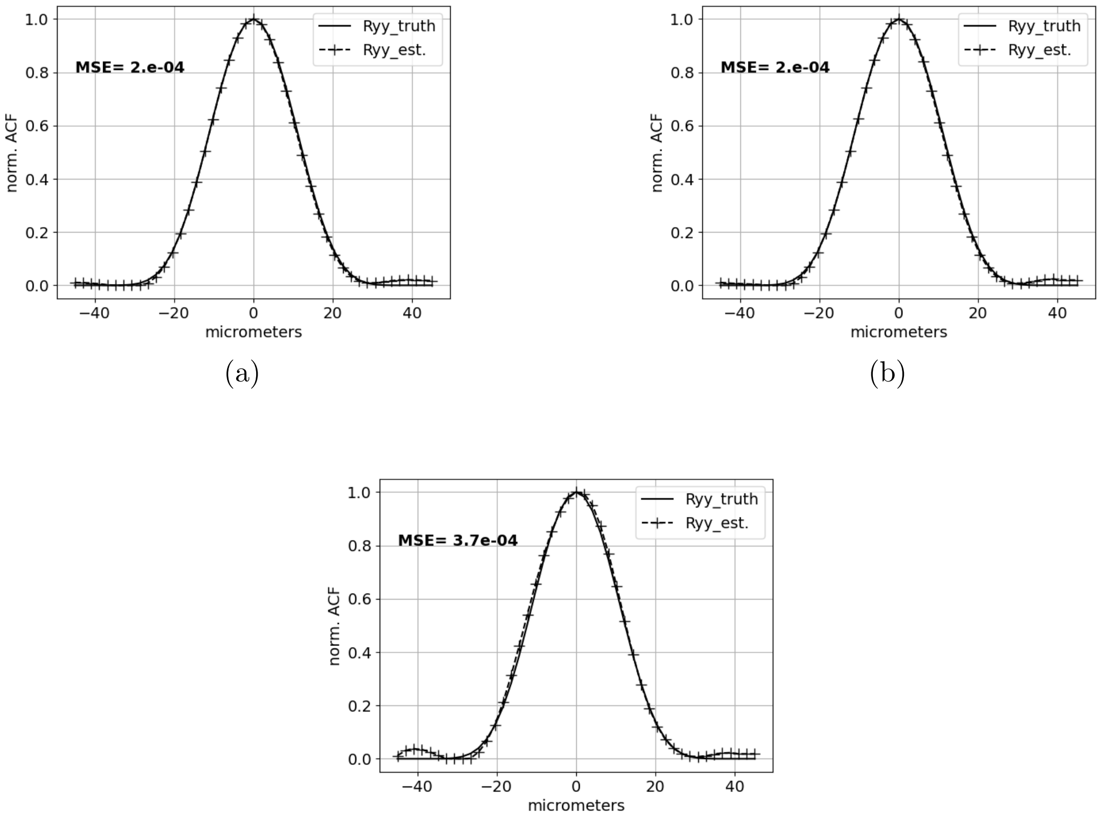

(a) (b)

(c)

Figure 61: One-dimensional R_{YY} ACF estimation and analytical comparison using 5000 independent speckle realizations and (a) 6× FPA R_{YY} sampling enhancement, (b) 2× FPA R_{YY} sampling enhancement, (c) 1× FPA R_{YY} sampling. The R_{YY} accuracy increases slightly as the estimation's spatial sampling rate increases.

curve. Completion of this analysis shows that a 2× FPA microscan is adequate to accurately estimate the system under test's MTF based off the previously established criterion.

5.3.3.2 R_{YY} Native 1× Sampling Rate

Finally, the analysis was completed using the R_{YY} estimation generated from 5000 independent speckle images and no FPA microscanning. The results are shown in Figs. 63(a)-(c). For this scenario, $\gamma = \sigma_\nu^2/2$, increasing the regularization term weight due to the increased estimation error compared to the previous analysis. A

1-D plot of the final estimated impulse response, the actual modeled system impulse response and the initial impulse response estimate are shown in Fig. 63(a). For this analysis, an established convergence criterion was met after 65 iterations. Fig. 63(b) shows the negative log-likelihood function value at each iteration. The general trend is the negative log-likelihood function decreases as the number of iterations increases, as experienced in the previous tests. The MSE between the truth impulse response and the current iteration impulse response is shown in Fig. 63(c); an MSE of 2×10^{-4} occurs at the 65^{th} iteration. Fig. 63(d) shows the derived MTF error between the truth MTF and the estimated MTF after the final iteration. The MTF error reaches its maximum of 9.5% at 0.92 of the FPA Nyquist sampling frequency. The 2% MTF error threshold is violated throughout at all spatial frequencies past 0.3 Nyquist. Completion of this analysis shows that at least 2× microscanning is required to accurately estimate the system under test's MTF based off the accuracy criterion established in Ref. 70.

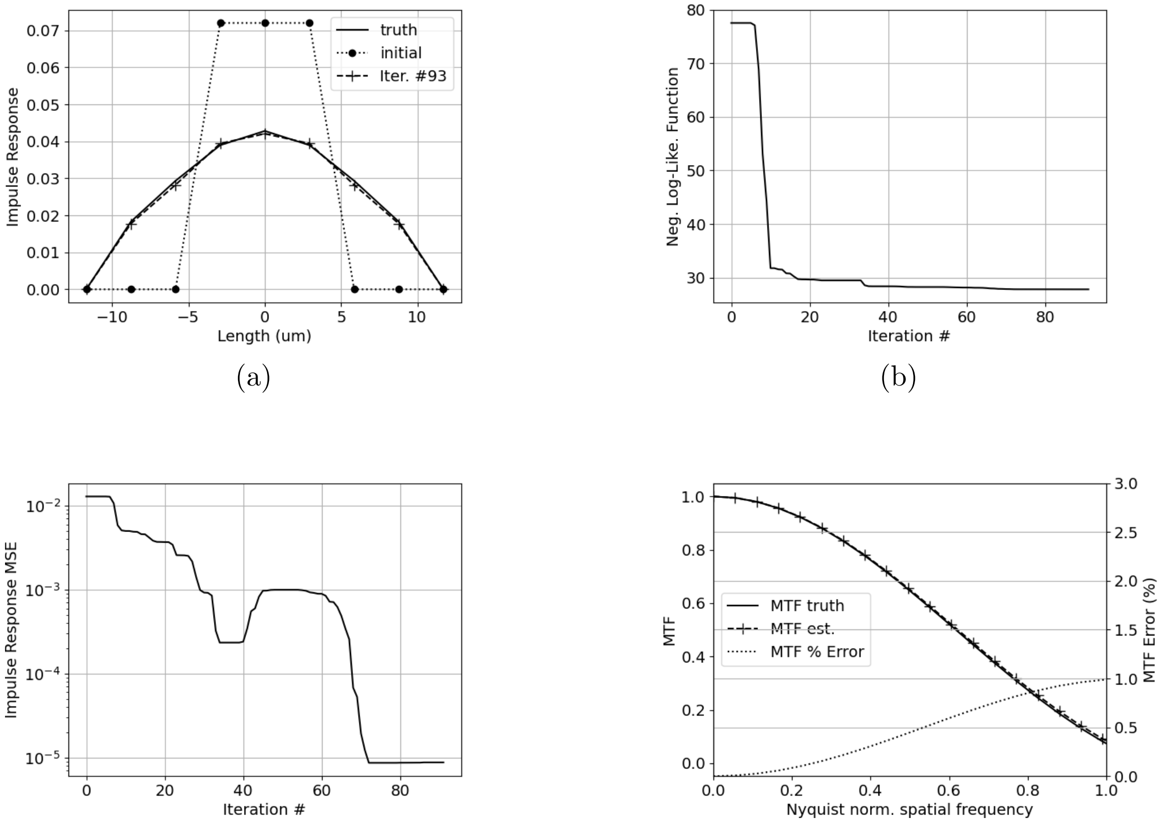

(a) (b)

(c) (d)

Figure 62: Iterative maximum likelihood estimation results with R_{YY} estimations generated with 5000 independent speckle image realizations and 2× FPA microscanning resolution. (a) truth, initial and final estimated focal plane array impulse responses (b) negative log-likelihood function calculations, (c) impulse response mean square error and (d) modulation transfer function estimation and relative percentage error. Convergence to a impulse response estimation with an associated modulation transfer function error that meets the established 2% accuracy threshold was achieved after 93 iterations.

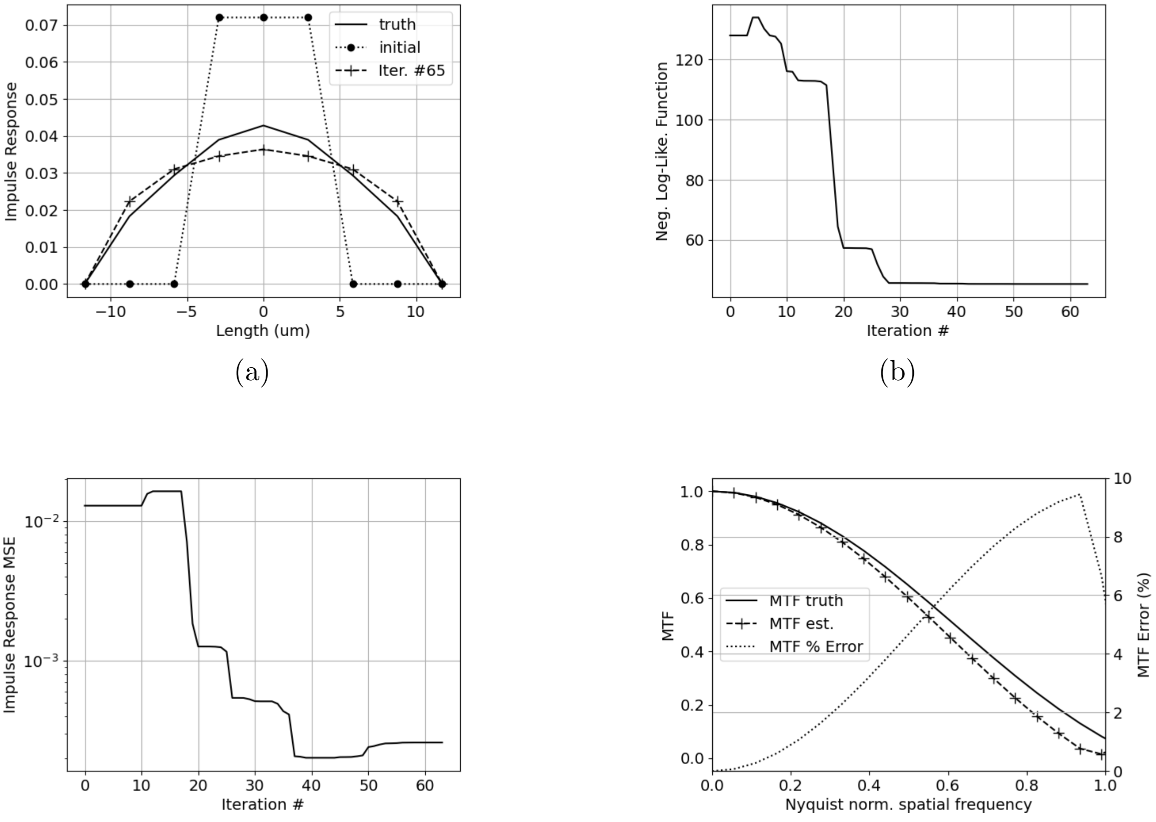

(a) (b)

(c) (d)

Figure 63: Iterative maximum likelihood estimation results with R_{YY} estimations generated with 5000 independent speckle image realizations and no microscanning. (a) truth, initial and final estimated focal plane array impulse responses (b) negative log-likelihood function calculations, (c) impulse response mean square error (d) modulation transfer function estimation and relative percentage error. Due to estimation error associated with R_{YY}, the impulse response estimation, specifically the associated modulation transfer function error does not meet the established 2% accuracy threshold.

5.4 Implementation Challenges

5.4.1 Theoretical Limitation: Delta-Correlated Speckle Assumption Validity

At shorter propagation distances than were explored in this analysis, the propagated RS ACF in Eq. (51) violates the delta-correlated initial speckle field ACF assumption [32], which is dependent on the surface characteristics used to generate it and the experiment's propagation geometry. Section 4.2.3 details the theoretical limitations of the delta-correlated initial speckle field ACF assumption.

5.4.2 Practical Experimental Challenges

Due to the ACF variation across the observation ROI, only a single realization is generated per speckle image. As shown in the Section 5.3.2, a minimum of 5000 independent speckle images is required to accurately estimate the ACF, R_{YY}, which is challenging to generate practically. Attempts have been made in the speckle MTF testbed to generate independent realizations using piezoelectric transducer-driven scanning mirrors [11] and microscanning stages. However, limited access to the Infragold® integrating sphere inner surface via the entrance port limits the potential for creating new images. Additionally, careful attention must be paid to the resulting effect on output speckle uniformity as well as the location of primary and secondary laser reflections within the integrating sphere. Due to the WSS assumption and quantification of the associated error, the Chapter IV generalized MTF estimation method is able to utilize multiple realizations (on the order of 100-1000 per image, depending on speckle image and window size choice) per image, significantly minimizing the estimation variance experienced when practically applying the impulse response estimation method. The Hamming window application in the generalized method's output PSD estimation process also significantly contributes to the estimation error minimization.

Section 5.3.3 demonstrated at least a 2× microscan is required to produce accurate R_{YY} estimations. This requirement not only increases the number of required recorded frames to 20,000, but also incorporates the additional experimental challenge of implementing accurate microscan super-resolution techniques. Current testbed challenges regarding aforementioned implementations include microscanning stage inaccuracies, laser stability and room vibrations. Techniques have been developed previously to correct for scanning inaccuracies [95] and uncontrolled vibrations [96]; however, such challenges increase experimental complexity. Assuming collection of the necessary number of independent speckle realizations and implementation of accurate super-resolution techniques is possible, collection of the required analysis data is taxing with regards to time and memory resources. A number of challenging, but surmountable, implementation hurdles are required to accurately experimentally implement the impulse response method. Overall estimated MTF spatial frequency range will be limited by validity of Eq. (51) with respect to propagation distance and system spatial frequency input.

5.5 Conclusion

This effort introduces a novel MLE approach to solving for the impulse response of an FPA. The advantage of this technique over conventional speckle-based FPA resolution techniques is its validity beyond conventional paraxial constraints of Fresnel propagation and its applicability to non-WSS random processes. The technique theory is developed and tested experimentally with simulated laser speckle images. Experimental tests demonstrate at least 5000 independent speckle realizations are required to accurately estimate the output speckle ACF, and subsequently the FPA impulse response. Additionally, the sampling rate at the FPA must be at least 2×

the native FPA to accurately estimate the speckle output ACF, and therefore the FPA's impulse response. In addition, the theoretical limitation of the validity for the delta-correlated input ACF with respect to the propagated speckle ACF is discussed. Finally, the practical experimental challenges associated with generation of large numbers of independent speckle image realizations and the difficulties associated with implementing the required microscanning super-resolution of the speckle images were investigated.

VI. Conclusions

As introduced in Chapter I, the primary research problem is to extend the capability of infrared (IR) speckle-based focal plane array (FPA) modulation transfer function (MTF) estimation beyond the paraxial limitations of currently established estimation methods, with the goal of estimating the MTF of lambda-scale FPA devices, where the detector pixel pitch is approximately equal to the desired detection wavelength, at higher spatial frequencies. This chapter begins with a summary and associated results of the major efforts undertaken to improve the resolution estimation capability of state-of-the-art IR FPAs. Next, the major technical contributions of the research to the field of IR FPA evaluation are explicitly identified. Finally, suggestions for future work are discussed.

6.1 Summary of Key Results

Critical factors impacting speckle imagery power spectral density (PSD) estimation were investigated in Chapter III, including number of independent realizations, window type, window size and aperture shape. The importance of maximizing independent realizations when attempting to accurately estimate second-order statistics of laser speckle was demonstrated, emphasizing the inverse relationship between number of independent realizations and PSD estimation variance. Furthermore, practical challenges associated with collecting independent realizations are discussed, including piezo-electric transducer (PZT) travel range limitations and the impact on sequentially collected speckle image correlation, laser stabilization and the effect on available collection time and dewar window shielding and the impact on useable analysis pixels. Additionally, the PSD estimation variance versus resolution trade-off was fully investigated, ultimately demonstrating that specific to the speckle testbed scenario, sacrificing spatial frequency resolution in order to increase speckle realizations and improve robustness to image non-uniformities is logical due to the slowly varying and generally smooth nature of MTF curves. Investigation of signal-independent noise in Section 3.6 showed larger area apertures lead to increased FPA signal, generating higher signal-to-noise (SNR) measurements and increased PSD estimation accuracy. Application of output PSD estimations to resultant MTF estimations in Section 3.6.2 demonstrated high MTF variance from brute-force periodogram estimation methods and inaccurate MTF estimations from the combination of input PSDs with sharp features and smooth output PSD estimates. Ultimately, the most accurate MTF estimations where produced from the combination of large area propagation apertures and Welch's spectral estimation technique.

A generalized MTF estimation technique was developed in Chapter IV, designed to address the challenge of lambda-scale FPA MTF estimation in nonparaxial test geometries. This nonparaxial test geometry is created via matching the lambda-scale detector's Nyquist sampling frequency with the laser speckle cutoff frequency. This technique utilized numerical Rayleigh-Sommerfeld (RS) propagation to compute speckle autocorrelation functions (ACFs), then indirectly developed speckle PSDs input upon the FPA. Despite the speckle process being non-wide-sense-stationary (WSS), the error associated with making stationary assumptions and employing linear systems analysis was quantified and determined negligible relative to window bias error introduced through Welch's spectral estimation technique utilized to estimate the output PSD from the speckle imagery. Experimental demonstration of this estimation approach in Figs. 53(a)-(b), showed a 27% spatial frequency range increase relative to an estimation made via the conventional closed-form input PSD solution reliant on Fresnel propagation assumptions.

Chapter V introduced an iterative maximum likelihood estimation (MLE) approach for FPA impulse response estimation valid beyond conventional paraxial constraints of Fresnel propagation and applicable to non-WSS random processes. Determination of method feasibility using simulated speckle images is demonstrated in Section 5.3; these efforts determined at least 5000 independent speckle realizations are required to accurately estimate the output speckle irradiance ACF, and therefore the FPA impulse response and MTF. Additionally, to accurately estimate the output speckle irradiance ACF, a sampling rate of at least 2× the rate associated with the native detector pixel pitch was required. After that, practical limitations associated with independent speckle image realization generation, such as limited integrating sphere surface accessibility were explained. Finally, speckle image microscanning super-resolution implementation challenges, like scanning stage inaccuracies, laser stability and room vibrations were described in Section 5.4.

6.2 Summary of Key Contributions

An original FPA resolution evaluation technique, coined the generalized FPA MTF estimation method, is established in Chapter IV. The experimentally-demonstrated spatial frequency range improvement of MTF estimations made via the generalized method compared to state-of-the-practice estimation procedures reliant on Fresnel propagation approximations is the key technical contribution provided by this research effort. Additionally, determining the error impact of random process WSS assumptions via utilization of the WDF and indirect determination of the speckle irradiance PSD via spatial averaging of applicable ACFs uncovered previously unexamined errors in conventional Fresnel regime speckle-based MTF estimation techniques.

The maximum likelihood approach to FPA impulse response estimation, introduced in Chapter V, is also a novel approach to IR detector resolution analysis. This technique is unique with respect to other detector analysis methods reliant on linear system theory as it is performed in the spatial domain and applicable to non-WSS random processes. Simulation results show the technique's potential for evaluating FPAs in geometries where Fresnel approximations are invalid.

The extensive output PSD estimation exploration in Chapter III, which was beneficial for FPA MTF estimation procedure optimization, is also an original comprehensive reference for any effort involving PSD estimation. Exploration of individual parameter impacts on PSD estimation is not unique, but the compilation of all analyzed factors and optimization for this specific measurement is novel.

6.3 Future Work

One area of future work involves developing the required experimental processes to generate a large number of independent speckle realizations, which will lead to the reduction of of estimation variance and windowing error bias. A general concept would involve incorporation of a smaller Infragold® integrating sphere (IS) at the primary IS entrance post, which would assist in generation of a uniform speckle field. Additionally, a combination of PZT-driven scanning mirrors and microscanning stages could be coupled to generate a large number of independent realizations.

Accurately implementing speckle image microscan super-resolution is another area of future effort. This would allow for experimental validation of the impulse response estimation technique and extension of MTF spatial frequency range estimation, assuming adequate independent speckle realization generation and window bias reduction. Current impediments to microscan super-resolution efforts include building vibrations and microscanning inaccuracies, which need to be quantified, minimized and/or mitigated. A functional interleaving interpolation technique [15, 95] has been identified and initially experimented with.

Although results compare favorably to expected detector resolution performance, verification of MTF results via comparison to other analysis techniques, such as FPA modeling programs [97], would provide robustness to the estimation technique and is another future area of research. Initial exploration of the presented technique certainly demonstrates the capability to effectively compare the resolution performance of several FPAs, investigating vital IR industry challenges such as determining the minimum device reticulation and passivization needed to achieve optimal device resolution performance.

Conducting a Design of Experiments (DoE) analysis of MTF estimation testbed would be another beneficial future effort, supporting further understanding and control of system errors. There are many factors involved in the process of estimating the MTF of an IR FPA using random laser speckle; having a better understanding of how these significant contributors affect output PSD estimations would increase the testbed robustness. Significant testbed error contributors include speckle field uniformity, propagation distance mismatch and experiment SNR. A DoE study may include completing a full factorial experiment of these components and performing an analysis of variance (ANOVA) on output PSD estimations. The effort may conclude with a regression analysis being performed on all significant variance factors to understand their impact on output PSD estimations.

Investigation of extending both the generalized and impulse response estimation techniques to geometries valid beyond the delta correlated initial speckle field ACF assumption limitations is a final area of potential future work. This would involve a more robust development of the initial speckle field ACF than has been previously investigated in the literature. This effort would most likely require vector wave propagation techniques and potentially the development of a detailed IS model, increasing the computational complexity of the estimation effort.

Appendix A. Speckle Testbed, Data Collection and Processing Description

The purpose of this appendix is to provide a more complete description of the speckle-based focal plane array (FPA) modulation transfer function (MTF) estimation testbed and analysis process for reader reference.

A.1 Testbed Description

The following is a detailed description of the speckle testbed and its components as specifically constructed for the experimental effort in Section 4.3.4. Figs. 64(a)-(b) identify important testbed sub-components. The light source is an Adtech Optics quantum cascade laser. The laser is operated at at 9.45 μm (15C) with a maximum output power of 48mW. The laser is temperature stabilized via utilization of a Peltier thermoelectric cooler, heat sink and air cooling. An 8-inch diameter Labsphere Infragold®-coated integrating sphere (IS) is used to generate the speckle field. A chemically etched, 32.3mm square diffracting aperture was placed at the IS's output port. A long-wave infrared (LWIR) linear polarizer with an extinction ratio of approximately 300:1 was placed just past the diffracting aperture to generate the polarized speckle required for the experiment [32]. The FPA was mounted in a pour-filled dewar with a 1" diameter Spectragon narrow band (∼240nm full width half maximum) filter, centered at the laser wavelength, as the cold stop in an F/2 configuration. This specific filter was chosen to minimize experiment noise due to significant background radiation. The laser was mounted on a Thorlabs NRT-150 motorized lateral translation stage and a Zaber X-VSR20A motorized vertical translation stage. The motion provided by these stages was synchronized with the frame captures to generate independent speckle realizations required for accurate statistics.

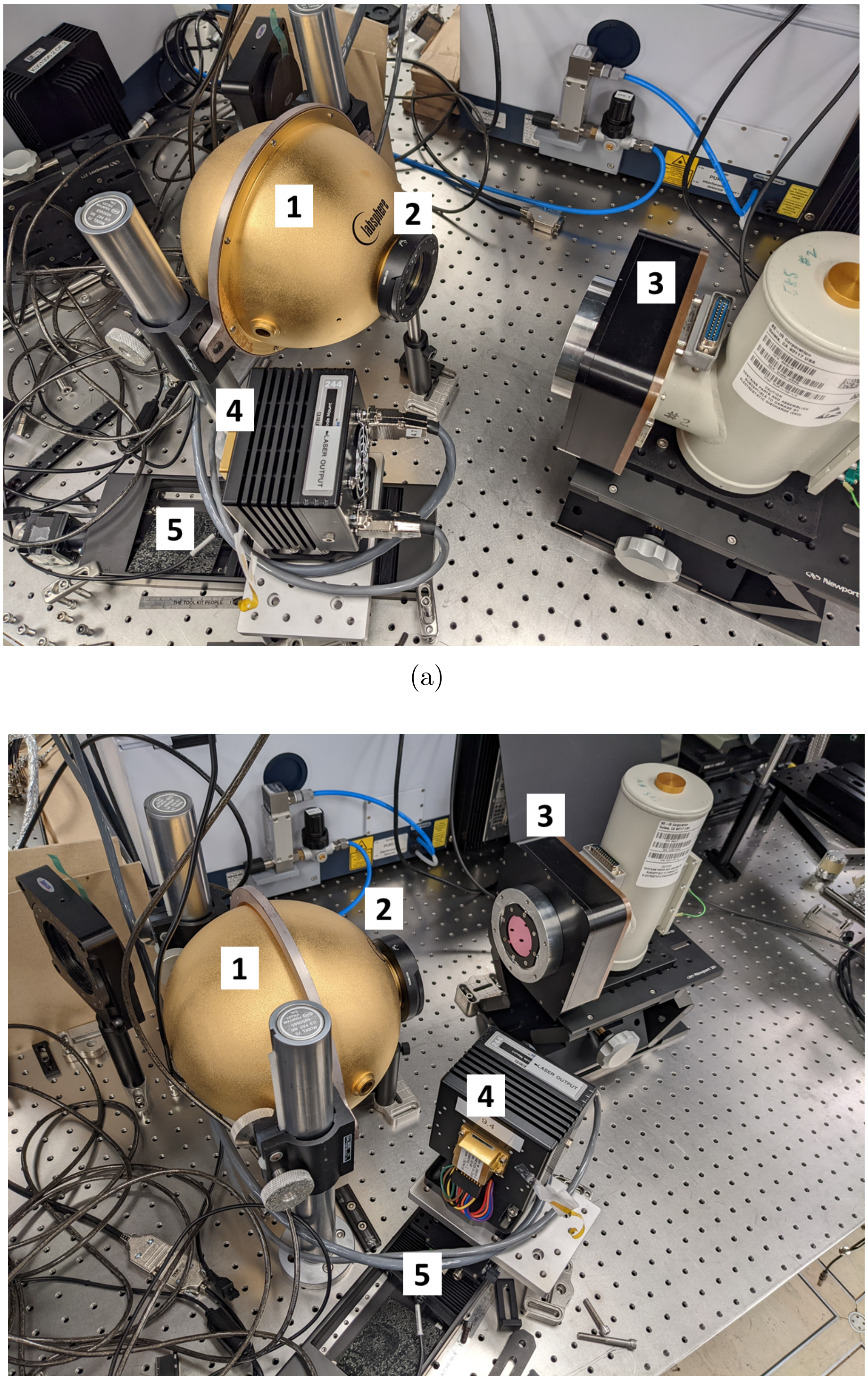

(a)

(b)

Figure 64: (a)Image of the speckle FPA MTF measurement setup. (b)Image of speckle FPA MTF measurement setup, alternative angle. Testbed components are numbered: 1) integrating sphere 2) mount holding diffracting aperture and wire-grid polarizer 3) pour-filled dewer containing narrowband cold filter and test FPA 4) LWIR quantum cascade laser 5) scanning stages.

A.2 Data Collection

A.2.1 Speckle Uniformity

A requirement for numerical evaluation and implementation of the speckle irradiance autocorrelation functions in Eqs. 51 and 54 is that the speckle irradiance at the IS output port must be uniform. Speckle uniformity is defined as $NU = \hat{\sigma}/\hat{\mu}$, the ratio between the speckle estimated standard deviation, $\hat{\sigma}$, and its mean, $\hat{\mu}$. A FLIR T1020 mircobolometer camera with a 36mm focal length lens was utilized to image the speckle at the output port. Fig. 65(a) shows an IS output port speckle image. A speckle image after low-pass filtering is shown in Fig. 65(b), highlighting any nonuniformity. Figure 65(c) shows a cross section of the low pass filtered speckle image in Fig. 65(b), demonstrating the speckle uniformity.

Using the data in Fig.65(a), the speckle nonuniformity was estimated to be 2.2%. Empirical demonstration of accurate FPA estimation with speckle nonuniformity of 2.4% was shown using prior speckle testbed iterations [11]. A testbed structure update focused on improving speckle uniformity would include incorporation of a second smaller IS at the primary IS input port. This implementation would require use of higher power laser sources.

A.2.2 Data Collection Process

Frame integration is synchronized with stage movements, with the goal of each collected frame being an independent laser speckle realization. Correction of speckle data is accomplished via application of piecewise linear nonuniformity correction using 100 blackbody frames per temperature collected over an appropriate blackbody range determined by inspection of speckle irradiance range.

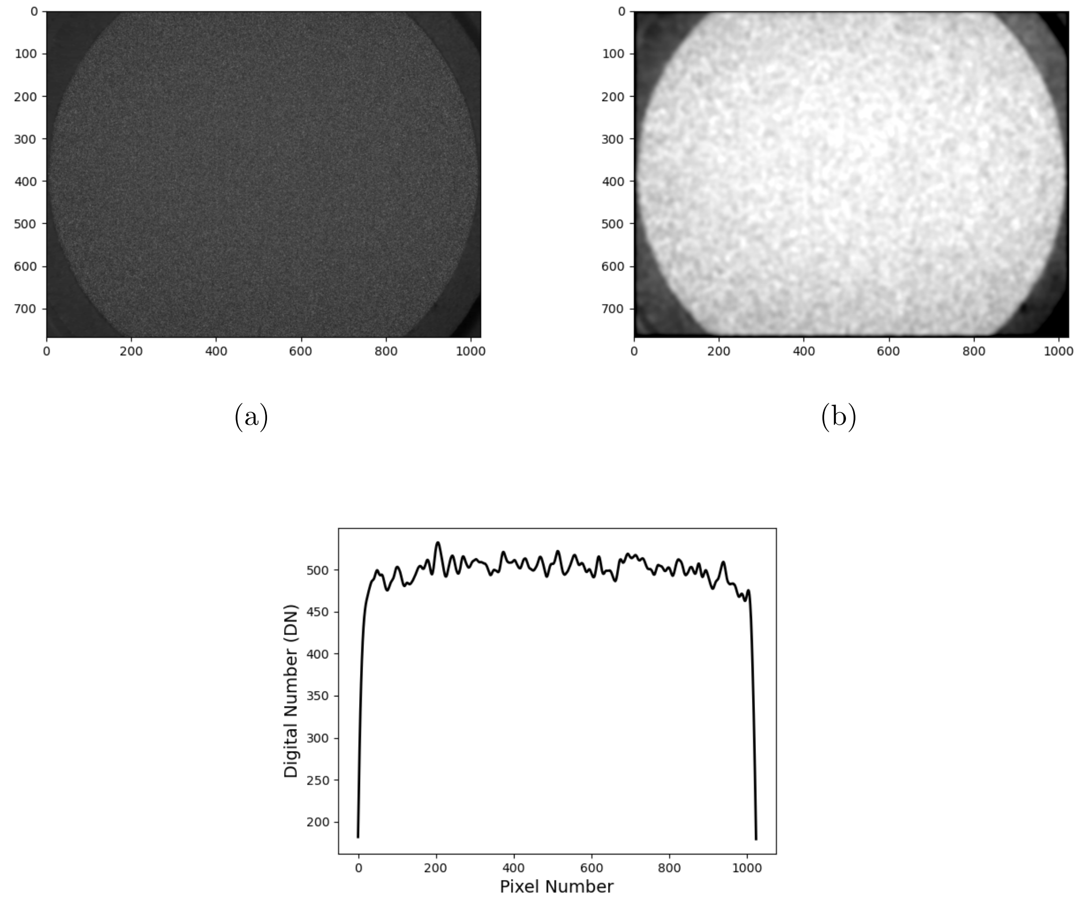

(a) (b)

(c)

Figure 65: (a) Unpolarized speckle image at integrating sphere output. (b) Unpolarized speckle image at integrating sphere output after low pass filtering to accentuate any nonuniformity. (c) Low pass filtered speckle image cross section in Fig. 65(b) showing the speckle uniformity.

A.3 Data Processing

A.3.1 Input PSD Determination

Computation of the input power spectral density (PSD) for the generalized FPA MTF estimation process is detailed in Section 4.3.3.1. For the conventional speckle-based method [76] that utilizes Fresnel electric field propagation equations, the input PSD upon the FPA is equivalent to the scaled autocorrelation function (ACF) of the diffraction aperture [32].

A.3.2 Output PSD Estimation

The output PSD estimation process utilized in the Section 4.3.3.2 is shown in Figure 66. First, a central region of interest (ROI) was utilized from each speckle image to minimize the impact of vignetting due to the infrared dewar configuration. Next, each image is demeaned to remove DC bias in the PSD estimation. Then, a segment is selected from each image and multiplied by a Hamming window, smoothing the PSD estimate. The trade-off between segment size, window bias and speckle image nonnuniformity is explored in Section 3.4. For this analysis, 31×31 image segments and Hamming windows were utilized. After that, a 2-D fast Fourier transform (FFT) is applied to each image segment and the magnitude squared of the segment FFT is computed, providing a periodogram for the PSD estimation. This process is repeated for entirety of the current image ROI and available image stack. The resulting periodograms are averaged and normalized, resulting in an output PSD estimation for the given test. This output PSD estimation along with the appropriate input PSD are then utilized in Eq. (44) to estimate the system MTF.

This output PSD estimation process was optimized via the analysis conducted in Chapter III. For the analysis in Section 4.3.3.2, the combination of a 512×512 image ROI, 50% window overlap and 16 speckle images provided adequate realizations to minimize the impact of estimation variance on the output PSD estimation effort, per the realization analysis conducted in Section 3.2.1.

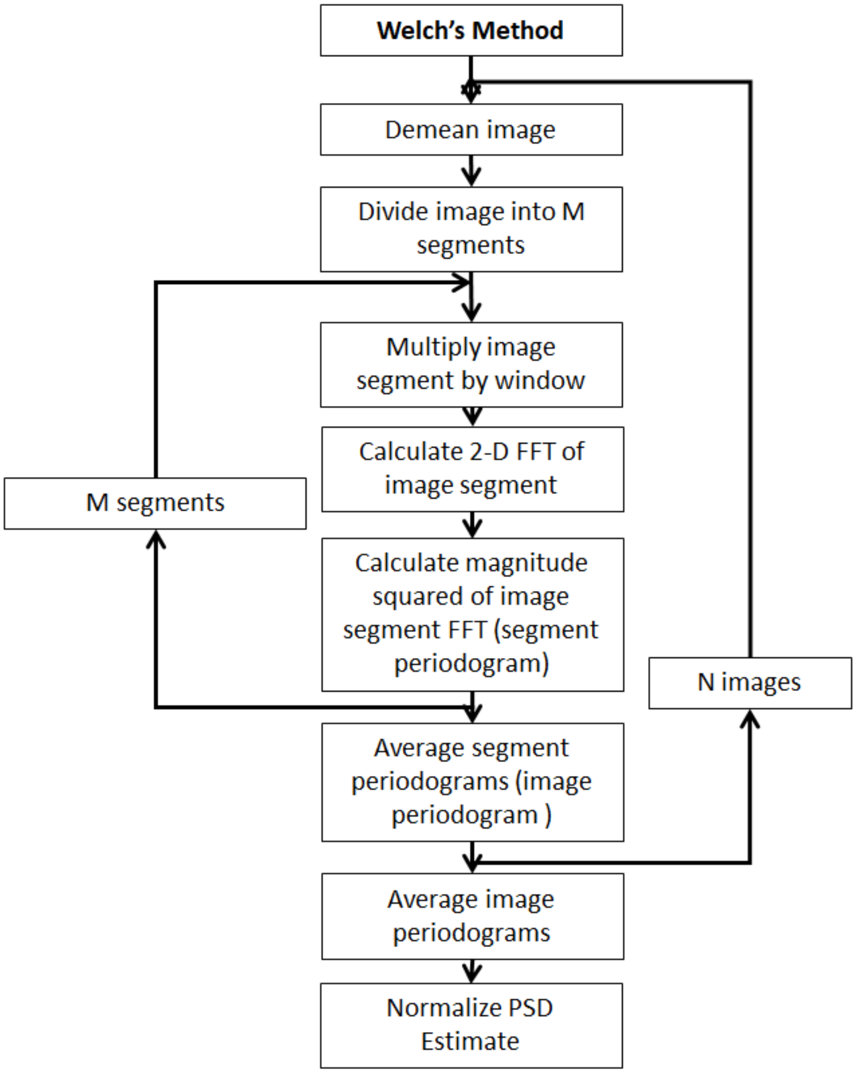

Figure 66: Block diagram of Welch's procedure, which is applied to non-uniformity corrected speckle imagery to generate output PSD estimations.

Appendix B. Detector Physics

There are several different architectures used to develop infrared (IR) detectors. Two prominent structures, p-n photodiodes and nBn strained-layer-superlattice (SLS) devices are investigated here. Basic device similarities and differences are addressed.

B.1 Bulk p-n Photodiodes

The bulk p-n photodiode is the most popular IR photodetector architecture currently utilized. This section gives a basic description of its typical band structure and introduces a device cross-section to facilitate understanding of basic detector operation.

B.1.1 Band Structure

A basic band diagram of a homogeneous p-n junction photodiode is shown in Fig. 67. In the IR, this structure is typically made out of homogeneous compound material, such as HgCdTe or InSb. One side of the device is an electron donor (n-type) and the other side of the device is an electron acceptor (p-type), where holes are the majority carriers. Due to free-carrier concentration gradient, the diffusion of electrons from the n-type region to the p-type region and the diffusion of holes from the p-type region to the n-type region develops a built-in potential across the junction. The inter-diffusion of electrons and holes between the n and p regions across the junction results in a region with no free carriers, called the depletion region. When a reverse bias is applied to the p-n junction, it expands the size of the depletion region and increases the potential. This is labeled the “space-charge” region in Fig. 67. Photons absorbed in the depletion region create electron-hole pairs, which are separated by the potential and contribute to the signal.

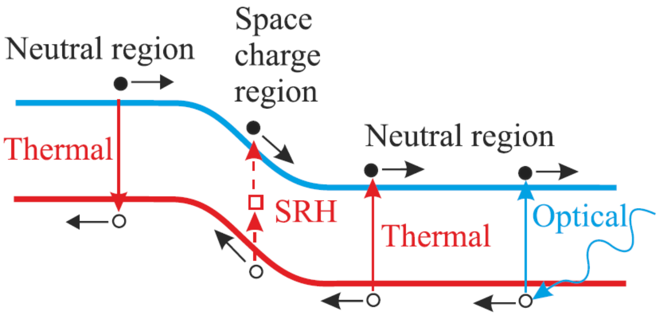

Figure 67: Diagram of conventional reverse-biased p-n photodiode. Image taken from source with permission [98].

B.1.2 Physical Diagram

The cross-section of a conventional p-n junction photodiode array is shown in Fig. 68. Notice the large n-type absorber region is the majority of the detector device. The p-type portion of the InSb device is used to define the pixels. Indium bumps are utilized to join the Si read-out integrated circuit (ROIC) device and InSb detector. Designing and developing the FPA and ROIC separately is a necessity in order to individually optimize each component.

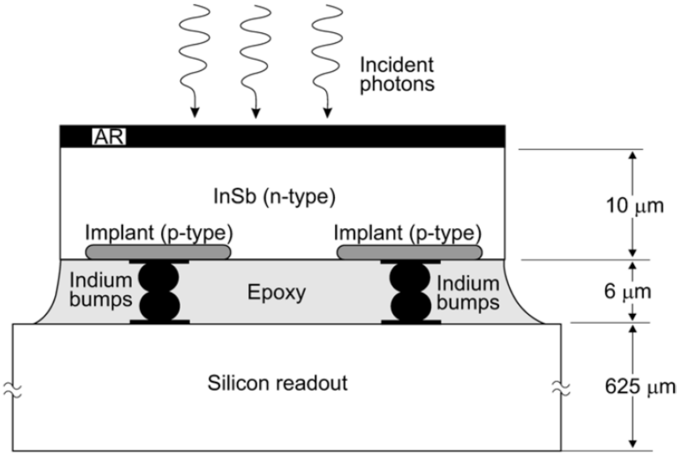

Figure 68: Conventional reverse-biased p-n photodiode. Image taken from source with permission [99].

B.2 SLS nBn III-V Detectors

SLS nBn (a barrier layer between two n-type semiconductors) III-V detectors are promising IR detector architectures, theoretically capable of high sensitivity performance at a low cost relative to conventional IR photodetectors [98,100]. A description of its basic band structure is presented below, along with a device cross-section to assist with explanation of typical detector operation.

B.2.1 Band Structure

The band diagram in Fig. 69 shows a typical nBn SLS stucture. This device consists of a photon-absorbing layer with a thickness on the order of the device's diffusion length; an n-type contact layer and a majority carrier barrier. The barrier is located near the minority carrier contact and away from the region of optical absorption. This barrier arrangement allows photogenerated holes to flow to the contact while surface current and the bulk of the majority carrier dark current are blocked. Homogenous doping type across all layers is key to maintaining low, diffusion-limited dark current [98].

B.2.2 Physical Diagram

The typical physical cross-section, as seen in Fig. 70, features a thick GaSb or GaAs substrate upon which the detector material is deposited on, an n-type absorber layer, an electron-blocking barrier layer and an n-type contact layer, reticulated to define each individual pixel. Indium bumps are once again utilized, physically bonding the SLS nBn detector and Si ROIC. Notice how each pixel is semi-reticulated to only the device barrier, in an attempt to maintain low dark current and overall device structural integrity.

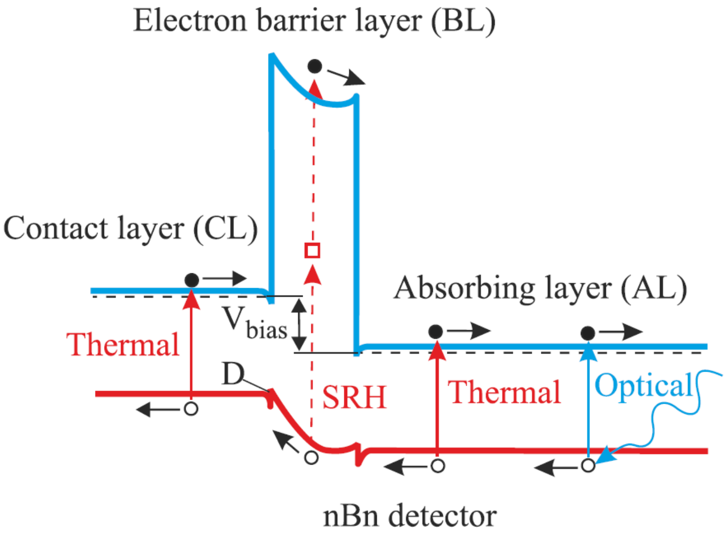

Figure 69: Diagram of reverse-biased nBn detector. Image taken from source with permission [98].

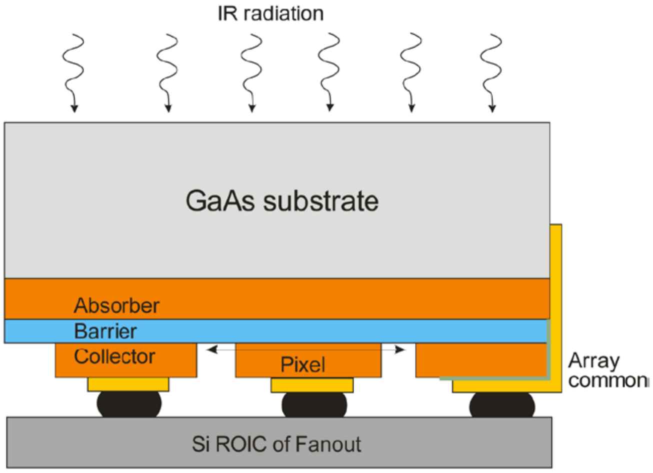

Figure 70: Example nBn detector array architecture. Image taken from source with permission [74].

B.2.3 Theoretical Device Performance Considerations

The theoretical noise advantage nBn SLS devices have over standard photodiodes is shown in Fig. 71. The red line represents diffusion dominated dark current; the blue slope depicts generation-recombination (GR) dominated dark current, caused by Shockley-Read-Hall traps in the depletion region. Since there is no depletion region in an nBn device, the GR noise contribution to the dark current is greatly suppressed. At temperatures below T_c, the cross-over temperature between diffusion current and GR current, an nBn device will have lower dark current than a p-n junction photodetector. As shown in Fig. 71, an nBn device can be run at the same temperature as a p-n device and receive a boost in noise performance. Alternatively, an nBn SLS device can be run at higher operating temperatures and have the same noise performance as a colder p-n device [98, 101].

Although this theoretical performance capability has yet to be achieved due to manufacturing challenges, this information points to the obvious reasons for investing in nBn SLS IR detector technology.

B.2.4 Absorption Coefficient

Absorption coefficient describes a detector material's ability to absorb incoming photons. Due to the unique design of a type-II SLS device structure, portions of the absorber are unable to collect electrons or holes. In Fig. 72, Ariyawansa [102] shows typical electron and hole accumulation regions within the periodic SLS structure. Notice the electron-hole overlap only occurs in the hole wells, which are a relatively small fraction of the entire device thickness. A bulk IR device, such as HgCdTe, is able to use its entire absorption region to store carriers, giving it a higher overall absorption coefficient. Therefore, SLS devices have generally lower absorption coefficients then bulk IR materials such as HgCdTe, as shown in Fig. 73. SLS devices with very

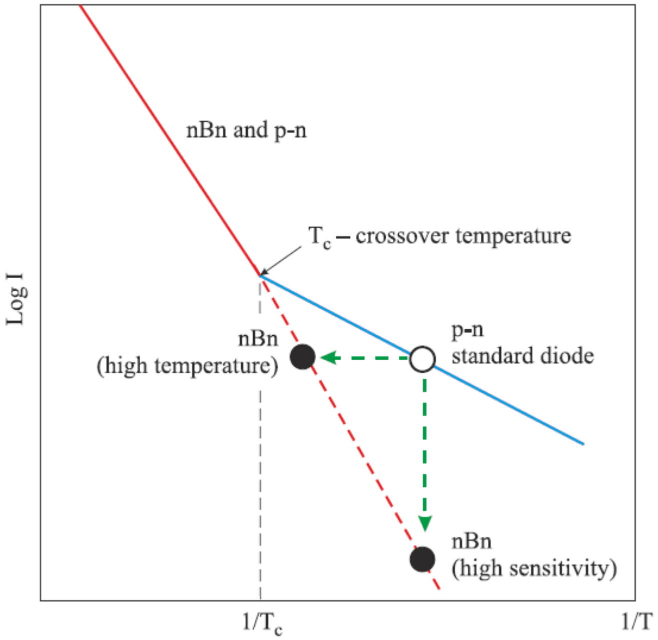

Figure 71: Arrhenius plot of dark current versus T^{-1} in a standard p-n detector and an nBn detector. Image taken from source with permission [98].

small periods, such as the 11/12 Å metamorphic device (pink curve), show similar absorption coefficient performance to bulk IR devices, such as HgCdTe (green curve) or InAsSb (purple curve), but they are challenging to produce. In order to match the quantum efficiency (QE) of a bulk IR device, typical SLS absorbers must be grown thicker, which increases the opportunity from crosstalk between pixels.

B.2.5 Effective Hole Mass and Diffusion Length

The effective hole mass is roughly an order of magnitude larger in SLS devices than in bulk IR detector materials [75, 98]. These large hole effective masses help to decrease current tunneling, but also lead to low hole mobility along the growth direction [75]. Minority carrier lifetimes are also typically smaller in SLS devices than bulk devices; however, their effect on diffusion length is smaller than the mobility effects. Effective hole mass $m*$, carrier lifetime τ_r and collision time τ_c are related to lateral diffusion length,

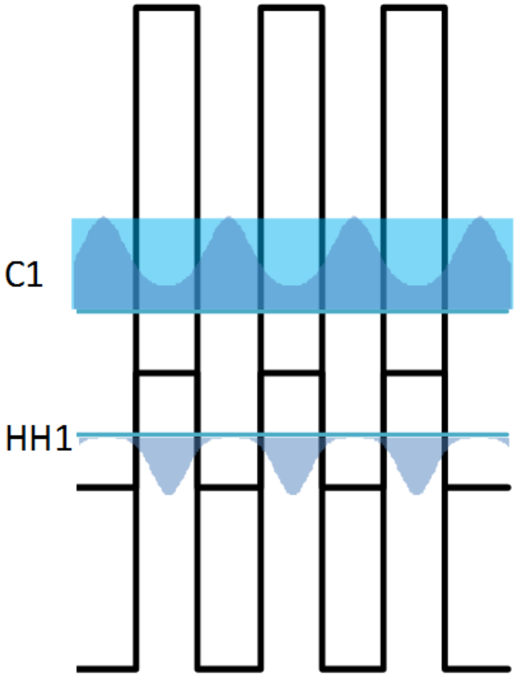

Figure 72: Example nBn SLS band diagram. Notice the carriers gathering in only specific areas of the absorber. Image taken from source with permission [102].

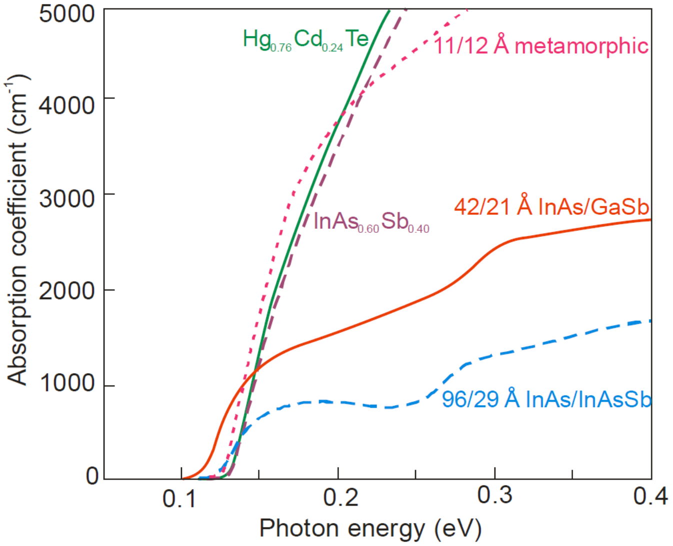

Figure 73: Calculated interband absorption coefficients as a function of photon energy at 80 K for bulk $InAs_{0.60}Sb_{0.4}$ and $Hg_{0.76}Cd_{0.24}Te$, and type-II superlattices: $42\text{Å}InAs/21\text{Å}GaSb$, $96\text{Å}InAs/29\text{Å}InAs_{0.61}Sb_{0.39}$ and $11\text{Å}InAs_{0.66}Sb_{0.34}/12\text{Å}InAs_{0.36}Sb_{0.64}$ metamorphic. Image taken from source with permission [103].

$$L_d = \sqrt{\frac{kT}{m*}\tau_r\tau_c} = \sqrt{D\tau_c}. \tag{81}$$

Terms in the carrier diffusion equation can also be simplified down to a diffusivity term, D, represented in units of $\frac{m^2}{s}$. Too short of a diffusion length will lead to a low QE; however, too long of a diffusion length, particularly in the lateral direction, can negatively affect modulation transfer function (MTF) performance. This is typically a larger issue in small pixel pitch devices [74].

B.2.6 Mobility Anisotropy

Mobility anisotropy refers to the ratio between vertical carrier mobility and lateral carrier mobility in a photodetector. Bulk p-n junction devices are typically isotropic, meaning their vertical and lateral mobility are equal. SLS nBn devices typically exhibit lateral carrier mobilities significantly greater than typical vertical carrier mobilities in these devices [75]. The superlattice designs, as shown in Fig. 72, decrease vertical mobility without affecting lateral carrier mobility. Relatively higher lateral carrier mobility leads to higher crosstalk between pixels.

Appendix C. Experimental Detector Architecture and Device Performance Trade-offs: Detailed Information

C.1 Front-side Illuminated, Fully Reticulated Detector

Greiner and Davis [16, 57] investigated the relationship between pixel reticulation and resolution performance. Point spread function (PSF) and MTF data measured from FPAs with two significantly different InSb detector architectures are represented in Figs. 76 and 75. The first design is a back-side illuminated array featuring a continuous bulk absorbing layer covering all the pixels. This is an unreticulated isotropic device, where carrier diffusion between pixels is as probable laterally as the desired vertical carrier diffusion. This particular device has a 100% fill factor. The second device, shown in Fig. 74, is a front-side illuminated, fully reticulated detector construction unique to L-3 Cincinnati Electronics [104, 105]. The basic FPA fabrication process starts with growing an InSb detector on an InSb substrate. This composite wafer is then bonded to optical silicon. The substrate is removed and the detectors are fully reticulated. Afterwards, the detector surface is passivated with dielectric material. A silicon ROIC is indium bump-bonded to the detector. This construction results in a thermally matched device. Having the detector sandwiched by two larger slabs of silicon reduces thermal stresses due to matching thermal coefficients of expansion.

Due to the full reticulation, lateral carrier diffusion is not possible, leading to a high resolution device, as shown in Fig. 75. Red lines indicate device MTF up to the FPA's Nyquist spatial frequency; Green lines indicate the aliased portion of the MTF recovered via microscanning. The FPA with the reticulated detector elements has a much higher overall MTF than the FPA with the unreticulated elements; the reticulated device has an MTF of 0.5 at 27 cycles/mm, whereas the unreticulated device has an MTF of 0.5 at 15 cycles/mm. The front-side illuminated device's capability to achieve an ideal sinc MTF can be seen in Fig. 76. Notice how the reticulated device has a square impulse response PSF, the FFT of which is a sinc function. The unreticulated device PSF has a Gaussian shape; this is due to the lateral carrier diffusion between the adjacent pixels. A large difference between these two devices is the active area of each pixel. The reticulated device has had 50% of its typical width and length etched away, leading to a 25% fill factor. In comparison, the unreticulated device has a 100% fill factor, making it a more sensitive device. These results show the importance of full pixel reticulation for peak device resolution performance.

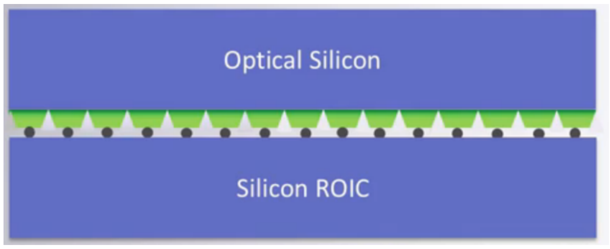

Figure 74: L3 detector basic cross section. Image taken from source with permission [58].

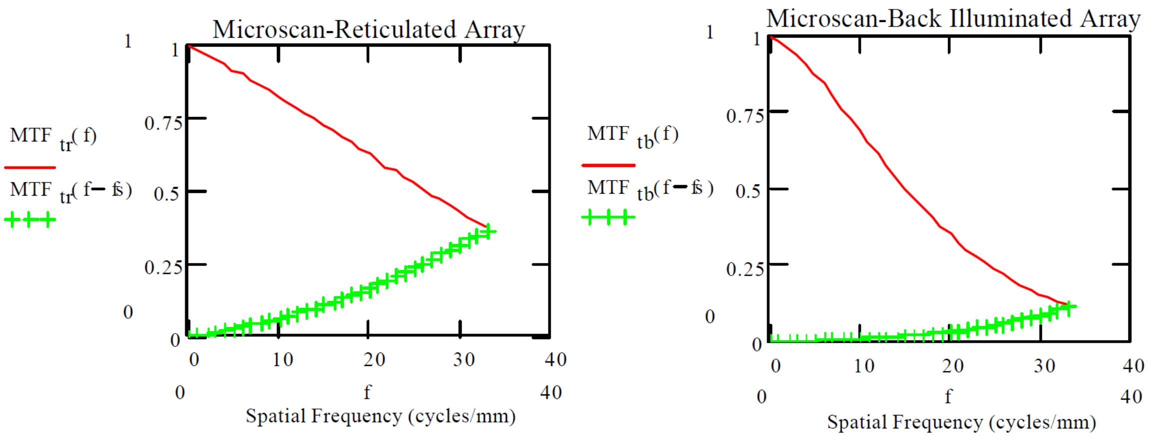

Figure 75: Modulation transfer function comparison between InSb detectors. Images taken from source with permission [57].

Through Vital Infrared Sensor Technology Acceleration (VISTA) program direction, this detector design technique has been expanded to high operating temperature

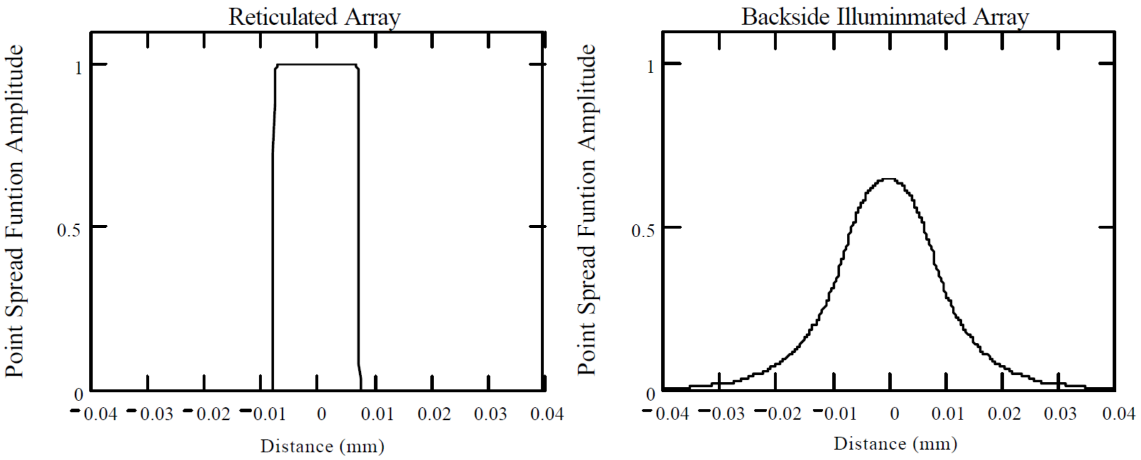

Figure 76: Point spread function comparison between InSb detectors. Images taken from source with permission [57].

MWIR type-II nBn SLS devices. Forrai [58] presented device results showing comparable performance in bulk InSb devices with regards to operability and turn-on voltage. Thinner type-two superlattice structures require less etch depth then conventional InSb structures, leading to higher device fill factor, which should help to increase the sensitivity of a reticulated design. Resolution performance results have not been published.

C.2 HDVIP Architecture

Diagnostic/Retrieval Systems, Inc. (DRS) extended their unique detector design [59, 60], shown in Fig. 77, to a $5\mu m$ pitch format. The high-density vertically integrated photodiode (HDVIP) pixel structure consists of a metal via interconnect passing through a HgCdTe film, down to the bonded ROIC. A cylindrical n-type region is formed around the via by type-converting the surrounding p-type HgCdTe, resulting in a n+/n/p diode.

Despite the small pitch, detector modeling suggests lateral carrier diffusion's effect on device MTF will be minor, as shown by Monte Carlo simulations in Fig. 78. Expected MTF results are less than an FPA with ideal $5\mu m$ square detector elements, but match the MTF performance of an FPA with ideal 6μm square detector elements. Further carrier diffusion tests shown in Fig. 79, including a point source test using a square single pixel mask, revealed electrical crosstalk may be a larger issue in this particular design then originally anticipated. Notice how adjacent pixels receive as much as 9% of the generated photocarriers. Results from this particular device architecture point to the need for full pixel reticulation to achieve ideal FPA resolution performance.

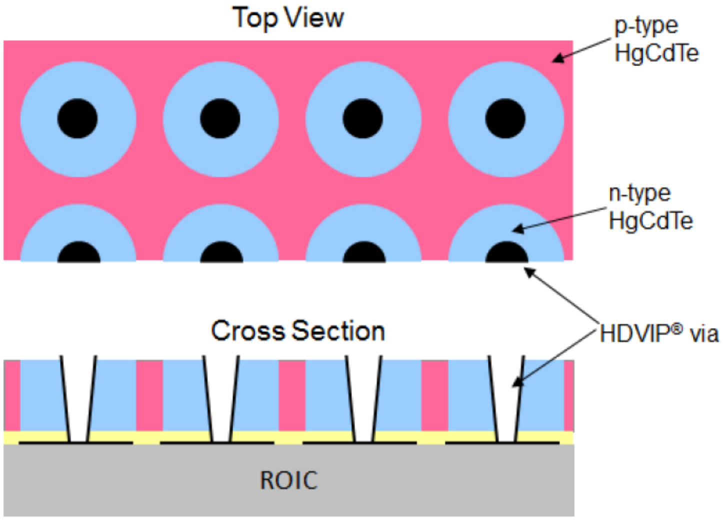

Figure 77: HDVIP top view and cross section. Images taken from source with permission [59].

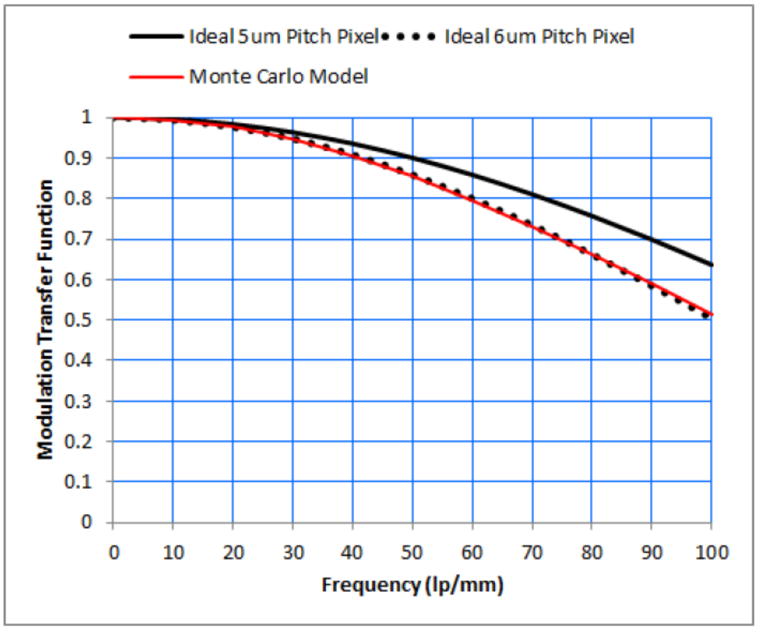

Figure 78: HDVIP MTF modeling versus theoretical comparison. Image taken from source with permission [59].

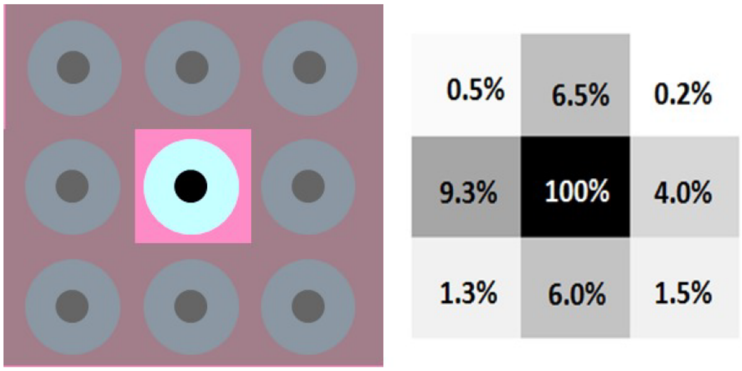

0.5%	6.5%	0.2%
9.3%	100%	4.0%
1.3%	6.0%	1.5%

Figure 79: HDVIP lateral carrier test diffusion results. Images taken from source with permission [59].

C.3 Full Dry-Etch and Dielectric Passivation Technique

HRL researchers have recently published results showing greater than 90% of an ideal sinc MTF, introduced in Eq. (11), and relatively low dark current noise for nBn SLS devices [61, 62]. HRL's devices are constructed using a refined deep dry etch process; it features high aspect angles of greater than 80%, as seen in Fig. 80, leading to devices with fill factors above 75%. This high fill factor helps to increase device QE. HRL's devices also feature a dielectric-based passivation technique, significantly suppressing leakage current and lowering dark current. Dark current values of roughly an order of magnitude greater than Tennant's "Rule 07" [2] have been reported for MWIR devices with $5.11\mu m$ cutoff wavelengths operating at 150K. These devices show operability and reliability numbers on par with their bulk InSb counterparts.

Estimated device MTFs were also presented for the dual-band versions of these devices [61]. MTF was measured using a technique very similar to Estribeau's method mentioned in Sec. 2.2.2.2, where patterned metal, shown in Fig. 81, is deposited on the detector array surface. A typical knife edge calculation, described in Sec. 2.2.1.2, is performed, resulting in MTF estimations for both device bands. MTF plots in Fig. 82 show detector MTF estimations greater than 90% of an ideal detector for both bands, with the long-wave infrared (LWIR) band performing slightly better most likely due to the full reticulation of its elements. The MWIR detectors were only reticulated halfway to help maintain the structural stability of the device. These results point to the potential of a high resolution nBn SLS detector with decent sensitivity, if individually etched pixels are properly passivated with adequate dielectric materials.

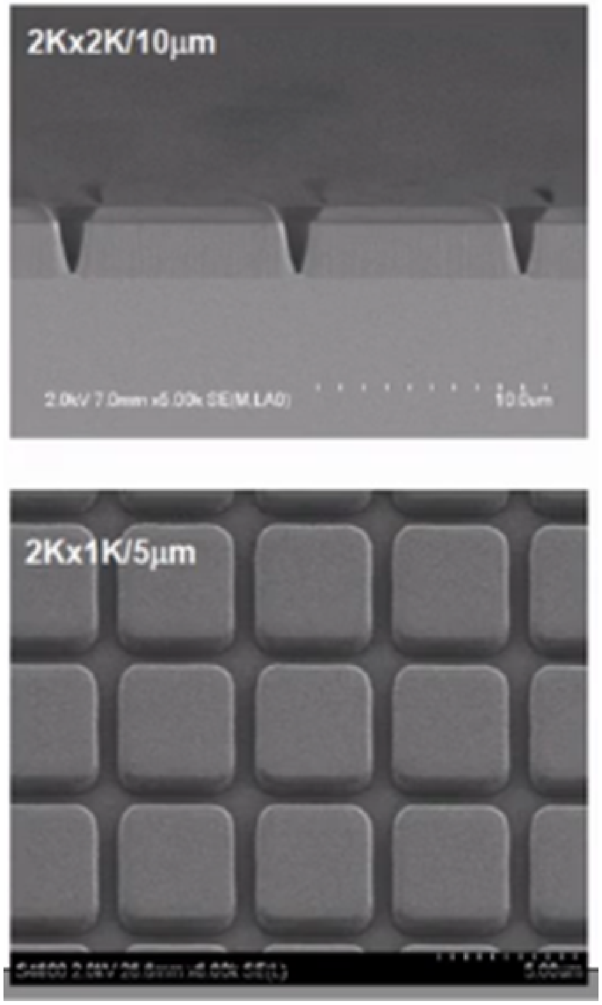

Figure 80: Scanning electron microscope images of high aspect angle pixel etches. Images taken from source with permission [61].

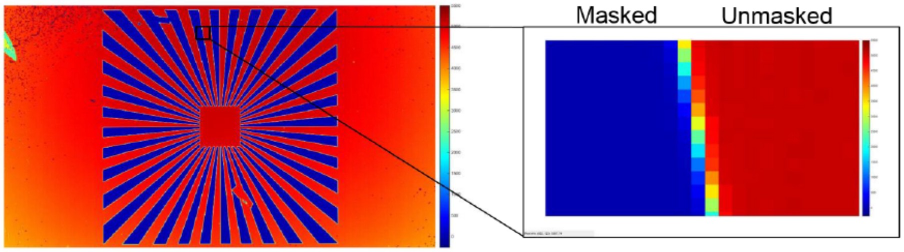

Figure 81: Masking for direct estimate of MTF. Images taken from source with permission [61].

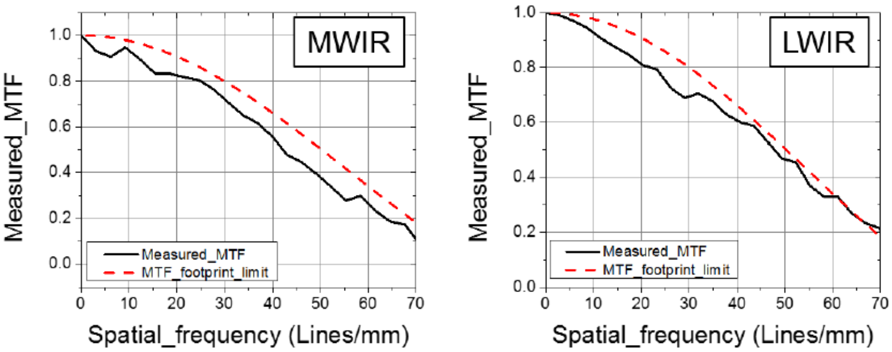

Figure 82: HRL's nBn SLS dual-band measured results. Images taken from source with permission [61].

C.4 Detector Architecture and Sensitivity Trade-offs

This section shows how detector pixel reticulation impacts device sensitivity. Research from multiple detector fabricators is presented, showing how full pixel reticulation can lead to dramatic increase in device dark current.

University of New Mexico's Professor Krishna and students investigated the effect pixel reticulation has on nBn SLS device dark current [63]. The device structure under consideration, shown in Fig. 83, consists of a $0.36\mu m$ thick n-type bottom contact layer made of SLS InAs:Si (8 monolayers [MLs]) / GaSb (8 MLs), followed by an non-intentionally doped (residually n-doped) $1.4\mu m$ thick absorbing layer consisting of SLS InAs (8 MLs) / GaSb (8 MLs), followed by a $100nm$ thick $Al_{0.2}Ga_{0.8}Sb$ barrier layer and a $0.09\mu m$ n-type top contact layer made of the same SLS as the bottom contact layer. The doping concentration in silicon-doped InAs layers was set to $4 \times 10^{18} cm^{-3}$ to ensure good ohmic contacts.

Two separate devices of this structure were tested. One was deep-etched past the absorbing layer, down to the bottom contact layer, shown in Fig. 83.b. The other was a baseline device, etched in a classical manner, only down to the device barrier, as shown in Fig. 83.a.

Dark current was measured for both devices as a function of temperature, shown in Fig. 84. Results from the deep-etched device are shown by the black dots; results for the baseline shallow-etched device are shown with the red dots. Dark current differences between the devices is an order of magnitude at 77K. The shallow-etched device has half the dark current as the deep-etched device at 150K. This is most likely caused by the increased surface leakage in the device due to the creation of large etched mesas.

Nolde completed a similar test using a LWIR p-type SLS device [106], showing two orders of magnitude dark current increase in the deep-etched device 80K operating temperature and bias. These examples highlight the important trade-off between resolution and sensitivity in nBn SLS IR detectors. In an attempt to improve resolution via pixel reticulation, device sensitivity was degraded.

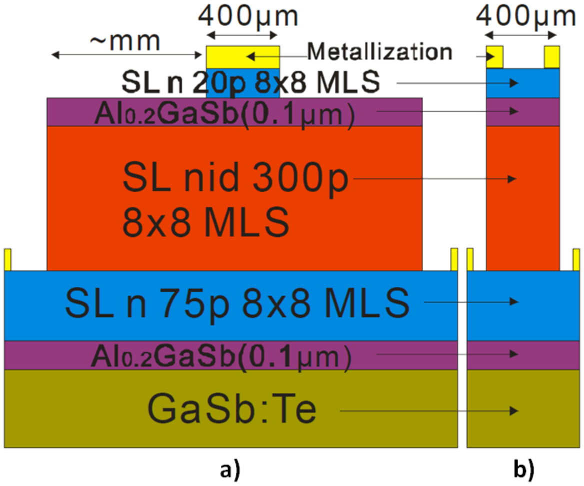

Figure 83: Schematic of nBn detector with (a shallow wet etching and b) deep etching. Image taken from source with permission [63] ©[2007] IEEE.

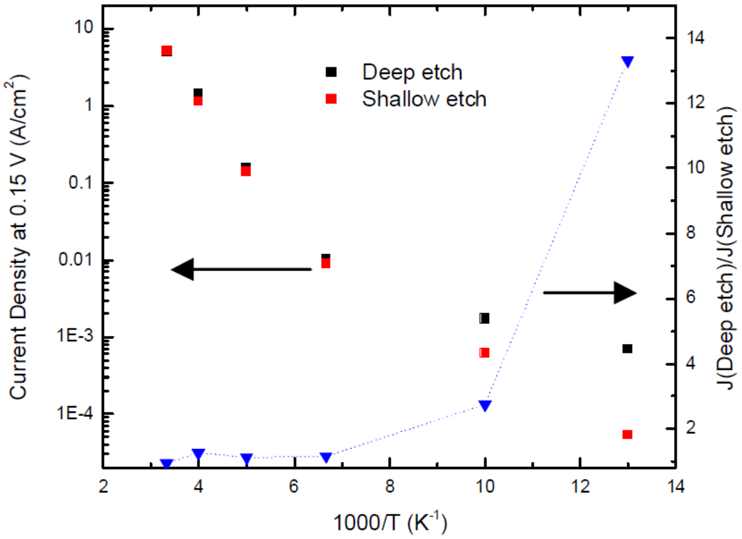

Figure 84: Dark current density comparison of two nBn detectors depending on temperature. Image taken from source with permission [63] ©[2007] IEEE.

Bibliography

1. Kaiqin Chu and Nicholas George. Correlation function for speckle size in the right-half-space. *Optics communications*, 276(1):1–7, 2007.

2. WE Tennant, Donald Lee, Majid Zandian, Eric Piquette, and Michael Carmody. Mbe hgcdte technology: a very general solution to ir detection, described by “rule 07”, a very convenient heuristic. *Journal of Electronic Materials*, 37(9):1406–1410, 2008.

3. Glenn D. Boreman. *Modulation Transfer Function on Optical and Electro-Optical Systems.* SPIE Press, first edition, 2001.

4. Photography– Electronic still picture imaging - Resolution and spatial frequency responses. Standard, International Organization for Standardization, Geneva, CH, January 2017.

5. Richard Barakat. Determination of the optical transfer function directly from the edge spread function. *JOSA*, 55(10):1217–1221, 1965.

6. Glenn D Boreman and Sidney Yang. Modulation transfer function measurement using three-and four-bar targets. *Applied optics*, 34(34):8050–8052, 1995.

7. Peter D Burns. Slanted-edge mtf for digital camera and scanner analysis.

8. Peter D Burns and Don Williams. Refined slanted-edge measurement for practical camera and scanner testing. In *IS AND TS PICS CONFERENCE*, pages 191–195. SOCIETY FOR IMAGING SCIENCE & TECHNOLOGY, 2002.

9. John W Coltman. The specification of imaging properties by response to a sine wave input. *JOSA*, 44(6):468–471, 1954.

10. Glenn David Boreman. Measurements of modulation transfer function and spatial noise in infrared ccd's (speckle, information theory, optics). 1984.

11. Kenneth J Barnard, Igor Anisimov, and John E Scheihing. Random laser speckle based modulation transfer function measurement of midwave infrared focal plane arrays. *Optical Engineering*, 51(8):083601–1, 2012.

12. Alfred D Ducharme and Sarah P Temple. Improved aperture for modulation transfer function measurement of detector arrays beyond the nyquist frequency. *Optical Engineering*, 47(9):093601–093601, 2008.

13. Edward Kamen and Bonnie S Heck. *Fundamentals of Signals and Systems Using the Web and MatLab: AND Mathworks, MATLAB Sim SV 07.* Prentice Hall Press, 2007.

14. Kenneth J Barnard and Glenn D Boreman. Modulation transfer function of hexagonal staring focal plane arrays. *Optical Engineering*, 30(12):1915–1919, 1991.

15. Jack D Gaskill. Linear systems, fourier transforms, and optics. *Linear Systems, Fourier Transforms, and Optics by Jack D. Gaskill New York, NY: John Wiley and Sons, 1978*, 1978.

16. Mike Davis, Mark Greiner, John Sanders, and Jim Wimmers. Resolution issues in insb focal plane array system design. In *Proc. SPIE*, volume 3379, pages 288–299, 1998.

17. L Karp, Charles A Musca, John M Dell, and Lorenzo Faraone. Characterization of crosstalk in hgcdte n-on-p photovoltaic infrared arrays. In *Microelectronics: Design, Technology, and Packaging*, volume 5274, pages 183–194. International Society for Optics and Photonics, 2004.

18. David S Smith and James T Wimmers. Crosstalk in closely-spaced indium antimonide detectors. In *Infrared technology XIV*, volume 972, pages 2–9. International Society for Optics and Photonics, 1988.

19. David N Sitter, James S Goddard, and Regina K Ferrell. Method for the measurement of the modulation transfer function of sampled imaging systems from bar-target patterns. *Applied optics*, 34(4):746–751, 1995.

20. W.J. Smith. *Modern Optical Engineering, 4th Ed.* McGraw Hill professional. McGraw-Hill Education, 2007.

21. Don Williams and Peter D Burns. Low-frequency mtf estimation for digital imaging devices using slanted-edge analysis. In *Image Quality and System Performance*, volume 5294, pages 93–102. International Society for Optics and Photonics, 2003.

22. Jackson KM Roland. A study of slanted-edge mtf stability and repeatability. In *SPIE/IS&T Electronic Imaging*, pages 93960L–93960L. International Society for Optics and Photonics, 2015.

23. Bing Chen, Yunsheng Qian, Benkang Chang, and Yi Cai. Measurement method of the modulation transfer function of focal plane arrays. *Multispectral and Hyperspectral Image Acquisition and Processing: 22-24 [October] 2001, Wuhan, China*, page 363, 2001.

24. Quiesup Kim, Guang Yang, C Wrigley, T Cunningham, and Bedabrata Pain. Modulation transfer function of active pixel focal plane arrays. 2000.

25. Dongming Lu, Qian Chen, and Guohua Gu. Research on the analysis and measurement of mtf of staring imaging system. In *Proceedings of SPIE*, volume 6059, pages 331–339, 2006.

26. Alfred D Ducharme and Eyal Sapir. Random transparency targets for modulation transfer function measurement in the visible and infrared regions. *Optical Engineering*, 34(3):860–868, 1995.

27. G Boreman and EL Dereniak. Method for measuring modulation transfer function of ccd's using laser speckle. In *PROCEEDINGS OF THE SOCIETY OF PHOTO-OPTICAL INSTRUMENTATION ENGINEERS*, volume 501, pages 174–178. SOC PHOTO-OPTICAL INSTRUMENTATION ENGINEERS PO BOX 10, BELLINGHAM, WA 98227-0010, 1984.

28. EL Dereniak. Method for measuring modulation transfer function of charge-coupled devices using laser speckle. *Optical Engineering*, 25(1):148–150, 1986.

29. Edward W Kamen. *Introduction to signals and systems.* Macmillan Pub Co, 1987.

30. JC Dainty. I the statistics of speckle patterns. *Progress in optics*, 14:1–46, 1977.

31. JC Dainty and AH Greenaway. Estimation of spatial power spectra in speckle interferometry. *JOSA*, 69(5):786–790, 1979.

32. Joseph W Goodman. *Speckle phenomena in optics: theory and applications.* Roberts and Company Publishers, 2007.

33. Yuankun Sun and Anthony B James. Generation of laser speckle with an integrating sphere. *Optical Engineering*, 29(4):339–342, 1990.

34. Martin Sensiper, Glenn D Boreman, Alfred D Ducharme, and Donald R Snyder. Modulation transfer function testing of detector arrays using narrow-band laser speckle. *Optical Engineering*, 32(2):395–400, 1993.

35. Antonio Manuel Pozo and Manuel Rubiño. Comparative analysis of techniques for measuring the modulation transfer functions of charge-coupled devices based on the generation of laser speckle. *Applied optics*, 44(9):1543–1547, 2005.

36. Alfred D Ducharme. Recent advances in the modulation transfer function testing of detector arrays. In *Proceedings of SPIE, the International Society for Optical Engineering*, pages 70600U–1. Society of Photo-Optical Instrumentation Engineers, 2008.

37. Xi Chen, Nicholas George, Gennadiy Agranov, Changmeng Liu, and Bob Gravelle. Sensor modulation transfer function measurement using band-limited laser speckle. *Optics express*, 16(24):20047–20059, 2008.

38. William S Astar. New power-efficient optical filter for detector array modulation transfer function measurement by laser speckle. *Optical Engineering*, 35(9):2761–2765, 1996.

39. Alfred D Ducharme and Glenn D Boreman. Holographic elements for modulation transfer function testing of detector arrays. *Optical Engineering*, 34, 1995.

40. Alfred D Ducharme. Microlens diffusers for efficient laser speckle generation. *Optics express*, 15(22):14573–14579, 2007.

41. Cheng-ping Ying, Bin Wu, Heng-fei Wang, Xue-shun Shi, and Hong-yuan Liu. Mtf measurement of irfpa based on double-knife edge scanning method. In *ISPDI 2013-Fifth International Symposium on Photoelectronic Detection and Imaging*, pages 890746–890746. International Society for Optics and Photonics, 2013.

42. Magali Estribeau and Pierre Magnan. Pixel crosstalk and correlation with modulation transfer function of cmos image sensor. 2005.

43. Kenneth J Barnard, Glenn D Boreman, Allen E Plogstedt, and Barry K Anderson. Sine wave measurements of sprite detector mtf. *Infrared imaging systems: Design, analysis, modeling, and testing II*, pages 426–431, 1991.

44. Kenneth J Barnard, Glenn D Boreman, Allen E Plogstedt, and Barry K Anderson. Modulation-transfer function measurement of sprite detectors: sine-wave response. *Applied optics*, 31(1):144–147, 1992.

45. SONG Min‘LI Yefang and SUN Yi HU Jiasheng. Acquiring sine grating pattern of dynamic varying frequency for measuring mtf of ccd. *Detectors, focal plane arrays, and imaging devices II: 18-19 September, 1998, Beijing, China*, 3553:217, 1998.

46. John E Greivenkamp and Andrew E Lowman. Modulation transfer function measurement of sparse-array sensors using a self-calibrating fringe pattern. *Applied optics*, 33(22):5029–5036, 1994.

47. Zhao Liefeng, Feng Huajun, and Xu Zhihai. Modulation transfer function measurement of charge-coupled devices using frequency-variable fringe patterns. In *SPIE*, volume 6834, pages 68342F1–9, 2007.

48. Mike Marchywka and Dennis G Socker. Modulation transfer function measurement technique for small-pixel detectors. *Applied optics*, 31(34):7198–7213, 1992.

49. PZ Takacs, I Kotov, J Frank, P O'Connor, V Radeka, and DM Lawrence. Psf and mtf measurement methods for thick ccd sensor characterization. In *High Energy, Optical, and Infrared Detectors for Astronomy IV*, volume 7742, page 774207. International Society for Optics and Photonics, 2010.

50. Gerald C Holst. *Electro-Optical imaging system performance.* JCD Pub., first edition, 1995.

51. Michael Theodore Eismann. Hyperspectral remote sensing. SPIE Bellingham, 2012.

52. Ronald G Driggers, Richard Vollmerhausen, Joesph P Reynolds, Jonathan Fanning, and Gerald C Holst. Method for measuring modulation transfer function of charge-coupled devices using laser speckle. *Optical Engineering*, 51(6):063202, 2012.

53. Martin J Bastiaans. Application of the wigner distribution function in optics. *The Wigner Distribution—Theory and Applications in Signal Processing*, 375:426, 1997.

54. Martin J Bastiaans. Application of the wigner distribution function to partially coherent light. *JOSA A*, 3(8):1227–1238, 1986.

55. Maria Sandsten. Time-frequency analysis of non-stationary processes. *An Introduction, Lund University, Centre for Mathematical Sciences*, 2013.

56. Lorenzo Galleani, Leon Cohen, S Marshall, and G Sicuranza. Nonstationary stochastic differential equations. *Advances in Nonlinear Signal and Image Processing*, pages 1–14, 2006.

57. Mark E Greiner, Mike Davis, and John G Sanders. Resolution performance improvements in staring imaging systems using micro-scanning and a reticulated, selectable fill factor insb fpa. Technical report, CINCINNATI ELECTRONICS CORP MASON OH, 1999.

58. Dave Forrai. Implementing vista technology in a iii-v detector foundry (conference presentation). In *SPIE Defense+ Security*, pages 101770X–101770X. International Society for Optics and Photonics, 2017.

59. JM Armstrong, MR Skokan, MA Kinch, and JD Luttmer. Hdvip five-micron pitch hgcdte focal plane arrays. In *Infrared Technology and Applications XL*, volume 9070, page 907033. International Society for Optics and Photonics, 2014.

60. Michael A Kinch. Separate absorption and detection diode, March 17 2009. US Patent 7,504,672.

61. Pierre-Yves Delaunay, Brett Z Nosho, Alexander R Gurga, Sevag Terterian, and Rajesh D Rajavel. Advances in iii-v based dual-band mwir/lwir fpas at hrl. In *Infrared Technology and Applications XLIII*, volume 10177, page 101770T. International Society for Optics and Photonics, 2017.

62. H Sharifi, M Roebuck, S Terterian, J Jenkins, B Tu, W Strong, TJ De Lyon, RD Rajavel, J Caulfield, Brett Z Nosho, et al. Advances in iii-v bulk and superlattice-based high operating temperature mwir detector technology. In *Infrared Technology and Applications XLIII*, volume 10177, page 101770U. International Society for Optics and Photonics, 2017.

63. HS Kim, GD Bishop, JB Rodriguez, YD Sharma, E Plis, LR Dawson, and S Krishna. Suppressed surface leakage current using nbn infrared detector based on type ii inas/gasb strain layer superlattices. In *Lasers and Electro-Optics Society, 2007. LEOS 2007. The 20th Annual Meeting of the IEEE*, pages 648–649. IEEE, 2007.

64. Philip J Plummer, Kenneth J Barnard, and Michael A Marciniak. Parameter exploration for spectral estimation of speckle imagery. In *Infrared Imaging*

Systems: Design, Analysis, Modeling, and Testing XXX, volume 11001, page 110010T. International Society for Optics and Photonics, 2019.

65. Philip J Plummer, Kenneth J Barnard, and Michael A Marciniak. Investigation of speckle imagery spectral estimation challenges for modulation transfer function measurements. *Optical Engineering*, 58(7):077106, 2019.

66. Glenn D Boreman. Measurement of modulation transfer function of focal plane arrays and imaging systems. Technical report, UNIVERSITY OF CENTRAL FLORIDA ORLANDO CENTER FOR RESEARCH IN ELECTRO-OPTICS AND LASERS, 1994.

67. Martin Sensiper, Glenn D Boreman, Alfred D Ducharme, and Donald R Snyder. Use of narrowband laser speckle for mtf characterization of ccds. In *Aerospace Sensing*, pages 144–151. International Society for Optics and Photonics, 1992.

68. Steven Kay. *Intuitive probability and random processes using MATLAB®*. 2006.

69. Peter Welch. The use of fast fourier transform for the estimation of power spectra: a method based on time averaging over short, modified periodograms. *IEEE Transactions on audio and electroacoustics*, 15(2):70–73, 1967.

70. Kenneth J Barnard, Eddie L Jacobs, and Philip J Plummer. Accuracy and uncertainty in random speckle modulation transfer function measurement of infrared focal plane arrays. *Optical Engineering*, 55(12):121729–121729, 2016.

71. Charles W Therrien. *Discrete random signals and statistical signal processing.* Prentice Hall PTR, 1992.

72. JW Goodman, Yiping Feng, and Robert Aymeric. Speckle contrast measurement with low light levels and imperfect laser illumination. In *22nd Congress for the*

International Commission for Optics: Light for the Development of the World, volume 8011, page 801165. International Society for Optics and Photonics, 2011.

73. RE Ziemer and WH Tranter. Principles of communications 2nd. ed. *Hou-ghton Mifflin Co*, pages 37–111, 1985.

74. A Rogalski, P Martyniuk, and M Kopytko. Challenges of small-pixel infrared detectors: a review. *Reports on Progress in Physics*, 79(4):046501, 2016.

75. David Z Ting, Alexander Soibel, and Sarath D Gunapala. Hole effective masses and subband splitting in type-ii superlattice infrared detectors. *Applied Physics Letters*, 108(18):183504, 2016.

76. Glenn D Boreman, Yuankun Sun, and Anthony B James. Generation of laser speckle with an integrating sphere. *Optical Engineering*, 29(4):339–342, 1990.

77. A Gatti, D Magatti, and F Ferri. Three-dimensional coherence of light speckles: theory. *Physical Review A*, 78(6):063806, 2008.

78. Joseph W Goodman. *Introduction to Fourier optics*. Roberts and Company Publishers, 2005.

79. Daniel C Cole, Eytan Barouch, Uwe Hollerbach, and Steven A Orszag. Derivation and simulation of higher numerical aperture scalar aerial images. *Japanese journal of applied physics*, 31(12S):4110, 1992.

80. Bruce W Smith, Donis G Flagello, Joseph R Summa, and Lynn F Fuller. Comparison of scalar and vector diffraction modeling for deep-uv lithography. In *Optical/Laser Microlithography*, volume 1927, pages 847–857. International Society for Optics and Photonics, 1993.

81. Santasri Basu, Milo W Hyde IV, Salvatore J Cusumano, Michael A Marciniak, and Steven T Fiorino. Examining the validity of using a gaussian schell-model source to model the scattering of a fully coherent gaussian beam from a rough impedance surface. *Optical Engineering*, 52(3):038001, 2013.

82. Terrence S Lomheim and Linda S Kalman. Analytical modeling and digital simulation of scanning charge-coupled device imaging systems. In *Electro-Optical Displays*, pages 513–584. CRC Press, 2020.

83. Jennifer E Ward, Damien P Kelly, and John T Sheridan. Three-dimensional speckle size in generalized optical systems with limiting apertures. *JOSA A*, 26(8):1855–1864, 2009.

84. Peyton Z Peebles Jr. *Probability, random variables, and random signal principles*. McGraw-Hill, 2001.

85. Wei Lu and Namrata Vaswani. The wiener-khinchin theorem for non-wide sense stationary random processes. *arXiv preprint arXiv:0904.0602*, 2009.

86. Neil A Weiss. *Introductory statistics*. Number BOOK. Pearson Education, Inc, 2005.

87. Richard K Burdick, Connie M Borror, and Douglas C Montgomery. *Design and analysis of gauge R&R studies: making decisions with confidence intervals in random and mixed ANOVA models*. SIAM, 2005.

88. Anatoli Rogalski. Recent progress in infrared detector technologies. *Infrared Physics & Technology*, 54(3):136–154, 2011.

89. K Sam Shanmugan and Arthur M Breipohl. *Random signals: detection, estimation and data analysis*. Wiley, 1988.

90. Russell C Hardie, Kenneth J Barnard, and Ernest E Armstrong. Joint map registration and high-resolution image estimation using a sequence of undersampled images. *IEEE transactions on Image Processing*, 6(12):1621–1633, 1997.

91. Yu-Li You and Mostafa Kaveh. A regularization approach to joint blur identification and image restoration. *IEEE Transactions on Image Processing*, 5(3):416–428, 1996.

92. Elijah Polak and Gerard Ribiere. Note sur la convergence de méthodes de directions conjuguées. *ESAIM: Mathematical Modelling and Numerical Analysis-Modélisation Mathématique et Analyse Numérique*, 3(R1):35–43, 1969.

93. William A Gardner. Introduction to random processes with applications to signals and systems((book)). *New York, MacMillan Co., 1986, 447*, 1986.

94. Sung Cheol Park, Min Kyu Park, and Moon Gi Kang. Super-resolution image reconstruction: a technical overview. *IEEE signal processing magazine*, 20(3):21–36, 2003.

95. Kenneth J Barnard, Edward A Watson, and Paul F McManamon. Nonmechanical microscanning using optical space-fed phased arrays. *Optical Engineering*, 33(9):3063–3071, 1994.

96. Adrian Stern, Elad Kempner, Avi Shukrun, and Norman S Kopeika. Restoration and resolution enhancement of a single image from a vibration-distorted image sequence. *Optical engineering*, 39(9):2451–2457, 2000.

97. Jonathan Schuster, Benjamin Pinkie, Steve Tobin, Craig Keasler, Danilo D'Orsogna, and Enrico Bellotti. Numerical simulation of third-generation hgcdte detector pixel arrays. *IEEE Journal of Selected Topics in Quantum Electronics*, 19(5):1–15, 2013.

98. P Martyniuk, M Kopytko, and A Rogalski. Barrier infrared detectors. *Opto-Electronics Review*, 22(2):127–146, 2014.

99. Antony Rogalski. Hgcdte infrared detector material: history, status and outlook. *Reports on Progress in Physics*, 68(10):2267, 2005.

100. CH Grein, H Cruz, ME Flatte, and H Ehrenreich. Theoretical performance of very long wavelength inas/in x ga1-x sb superlattice based infrared detectors. *Applied Physics Letters*, 65(20):2530–2532, 1994.

101. S Maimon and GW Wicks. n b n detector, an infrared detector with reduced dark current and higher operating temperature. *Applied Physics Letters*, 89(15):151109, 2006.

102. G Ariyawansa, JM Duran, CJ Reyner, EH Steenbergen, N Yoon, D Wasserman, and JE Scheihing. Growth and characterization of in 1-x ga x as/inas 0.65 sb 0.35 strained layer superlattice infrared detectors. In *Infrared Technology and Applications XLIII*, volume 10177, page 1017712. International Society for Optics and Photonics, 2017.

103. A Rogalski. Inas/gasb type-ii superlattices versus hgcdte ternary alloys: future prospect. In *Electro-Optical and Infrared Systems: Technology and Applications XIV*, volume 10433, page 104330U. International Society for Optics and Photonics, 2017.

104. Harold A Timlin and Charles J Martin. Electro-optical detector array, July 13 1993. US Patent 5,227,656.

105. Harold A Timlin and Charles J Martin. Method of making electro-optical detector array, April 19 1994. US Patent 5,304,500.

106. JA Nolde, EM Jackson, MF Bennett, CA Affouda, ER Cleveland, CL Canedy, I Vurgaftman, GG Jernigan, JR Meyer, and EH Aifer. Reticulated shallow etch mesa isolation for controlling surface leakage in gasb-based infrared detectors. *Applied Physics Letters*, 111(5):051102, 2017.

REPORT DOCUMENTATION PAGE

Form Approved
OMB No. 0704–0188

1. REPORT DATE *(DD–MM–YYYY)* 10–05–2022	**2. REPORT TYPE** Doctoral Dissertation	**3. DATES COVERED** *(From — To)* Dec 2017 — June 2022

4. TITLE AND SUBTITLE

METHODS FOR FOCAL PLANE ARRAY RESOLUTION
ESTIMATION USING RANDOM LASER SPECKLE IN
NONPARAXIAL GEOMETRIES

5a. CONTRACT NUMBER

5b. GRANT NUMBER

5c. PROGRAM ELEMENT NUMBER

6. AUTHOR(S)

Plummer, Philip, CIV, USAF

5d. PROJECT NUMBER

5e. TASK NUMBER

5f. WORK UNIT NUMBER

7. PERFORMING ORGANIZATION NAME(S) AND ADDRESS(ES)

Air Force Institute of Technology
Graduate School of Engineering and Management (AFIT/EN)
2950 Hobson Way
WPAFB OH 45433-7765

8. PERFORMING ORGANIZATION REPORT NUMBER

AFIT-ENP-DS-22-J-027

9. SPONSORING / MONITORING AGENCY NAME(S) AND ADDRESS(ES)

AFRL/RYMT
Phil Maciejewski, Chief
Building 620
WPAFB OH 45433-7765
Email: philip.maciejewski@us.af.mil

10. SPONSOR/MONITOR'S ACRONYM(S)

11. SPONSOR/MONITOR'S REPORT NUMBER(S)

12. DISTRIBUTION / AVAILABILITY STATEMENT

DISTRIBUTION STATEMENT A:
APPROVED FOR PUBLIC RELEASE; DISTRIBUTION UNLIMITED.

13. SUPPLEMENTARY NOTES

14. ABSTRACT

The infrared (IR) community has a need for detector evaluation due to the continued demand for small pixel pitch detectors, the emergence of strained-layer-superlattice devices, and the associated lateral carrier diffusion issues. Conventional laser speckle-based modulation transfer function (MTF) estimation is dependent on Fresnel propagation, limiting utilization on lambda-scale IR devices. This effort develops two methodologies for resolution evaluation of IR focal plane arrays (FPA). Both techniques are valid in nonparaxial geometries dictated by lambda-scale devices. The generalized FPA MTF estimation approach numerically evaluates Rayleigh-Sommerfeld speckle autocorrelation functions to indirectly compute the power spectral density (PSD) of a non-wide-sense-stationary (WSS) speckle random process. This method is demonstrated on a lambda-scale longwave infared FPA, showing at 27% spatial frequency range improvement over the established methodology. A resolution estimation approach, which utilizes employs a maximum likelihood estimation approach to solve for a system impulse response, is demonstrated with simulated imagery.

15. SUBJECT TERMS

laser speckle, modulation transfer function (MTF), power spectral density (PSD), autocorrelation function (ACF), infrared (IR), focal plane array (FPA), Wigner distribution function (WDF), Maximum likelihood estimator (MLE), conjugate gradient descent

16. SECURITY CLASSIFICATION OF:			**17. LIMITATION OF ABSTRACT**	**18. NUMBER OF PAGES**	**19a. NAME OF RESPONSIBLE PERSON**
a. REPORT	**b. ABSTRACT**	**c. THIS PAGE**			Dr. Michael Marciniak, AFIT/ENP
U	U	U	UU	189	**19b. TELEPHONE NUMBER** *(include area code)* (937) 255-3636 x4529

Standard Form 298 (Rev. 8–98)
Prescribed by ANSI Std. Z39.18